Interface Controlled Secondary Structure Changes of the Fibril Forming Peptides B18 and β Amyloid

Sandra Cristina Pinto da Rocha

A thesis submitted to the Universidade do Porto for the degree of Ph.D. in Engineering Sciences

Universidade do Porto
Faculdade de Engenharia
FEUP

Porto, 2004

Resumo

Nos últimos anos tem-se assistido a um crescente interesse no estudo de alterações conformacionais e agregação de proteínas. Este facto deve-se essencialmente ao aparecimento de um grande número de amiloidoses genéticas e esporádicas, e ao surto da encefalopatia espongiforme bovina, doença infecciosa associada a alterações conformacionais. Estas doenças são caracterizadas por uma alteração estrutural da forma nativa das proteínas (geralmente em α-hélice ou aleatória) para a forma de agregados (fibras de amilóide). O mecanismo pelo qual as proteínas na sua forma nativa se transformam em agregados patológicos não está ainda completamente esclarecido. No entanto, o aumento da concentração de proteínas a nível fisiológico poderá estar na base da sua agregação e, consequentemente, a causa destas doenças estará possivelmente relacionada com condições que favorecem esse aumento. É de salientar que, tendo em conta a elevada estabilidade dos agregados, o tratamento destas doenças deverá passar pela inibição de alterações conformacionais e agregação de proteínas.

Neste trabalho caracterizaram-se as interacções de dois peptídeos, B18 e β-amilóide, com superfícies poliméricas hidrofílicas e hidrofóbicas. Procedeu-se também ao estudo conformacional de ambos os peptídeos quando em presença de diferentes moléculas de tensioactivos e de nano-partículas. O peptídeo B18 é derivado da proteína responsável pela fecundação no ouriço do mar. Por sua vez, o peptídeo β-amilóide deriva da proteína precursora da amilóide por clivagem enzimática, e constitui o componente principal das placas senis que caracterizam a doença de Alzheimer. Ambos os peptídeos possuem uma elevada tendência para agregar em fibras de amilóide.

O grau de adsorpção dos peptídeos B18 e β-amilóide em diversas superfícies foi estudado por técnicas de reflexão de raios-X e neutrões e por microscopia de força atómica. A afinidade dos peptídeos para determinadas superfícies pode ser responsável pelo aumento da sua concentração local, que resultará posteriormente na sua agregação. Os resultados demonstraram que os peptídeos B18 e β-amilóide adsorvem a superfícies hidrofóbicas e a polímeros hidrofílicos de carga oposta à sua carga total. Ambos os peptídeos apresentaram maior afinidade para superfícies hidrofóbicas, as quais poderão constituir uma potencial localização para a sua acumulação e agregação em fibras de amilóide.

A interacção dos peptídeos B18 e β-amilóide com os diversos tensioactivos foi caracterizada por espectroscopia de dicroísmo circular. Ambos os peptídeos possuem inicial-

mente, em solução aquosa, uma estrutura aleatória. O peptídeo B18 adoptou uma estrutura em α-hélice na presença de monómeros e de micelas de tensioactivos catiónicos e aniónicos. Os monómeros de tensioactivos não iónicos não tiveram qualquer influência na estrutura do peptídeo, enquanto que as suas micelas induziram uma estrutura em α-hélice. O peptídeo β-amilóide adquiriu uma estrutura em α-hélice apenas em presença de micelas de tensioactivos catiónicos e aniónicos. Em soluções de micelas não iónicas, o peptídeo adoptou uma conformação em folha-β. Observou-se que as micelas do surfactante aniónico e perfluorado foram as mais eficazes a induzir a estrutura em α-hélice em ambos os peptídeos.

Sabe-se que álcoois fluorados, como o trifluoretanol, e micelas iónicas são capazes de induzir, a pH 7.4, uma estrutura em α-hélice em peptídeos amiloidogénicos. Com base neste facto, foram sintetizados polímeros com monómeros catiónicos e aniónicos alternados que foram posteriormente complexados com ácido dodecanóico ou ácido perfluorododecanóico, originando nano-partículas coloidais com um diâmetro de 4 nm. Estas nano-partículas possuem um núcleo hidrofóbico e uma superfície hidrofílica. As cadeias hidrocarbonadas ou fluoradas dos tensioactivos constituem o núcleo hidrofóbico, enquanto que a superfície hidrofílica é formada pelo polímero. Os estudos de espectroscopia de dicroísmo circular mostraram que as nano-partículas fluoradas induzem uma estrutura em α-hélice em ambos os peptídeos B18 e β-amilóide. Por sua vez, os análogos hidrocarbonados são menos eficientes, visto que, na maioria dos casos, conduziram à formação de estrutura em folha-β ou à agregação dos peptídeos. Uma vez que a estrutura em α-hélice é uma estrutura monomérica e estável, as nano-partículas fluoradas constituem potenciais agentes inibidores da agregação proteica.

Résumé

Les changements conformationnels et l'agrégation des protéines sont actuellement l'objet d'études intensives. Cet intérêt est principalement motivé par l'occurrence accrue d'amyloses génétiques et sporadiques et par la manifestation de l'encéphalopathie spongiforme bovine, une maladie infectieuse liée à des transitions de conformation de protéines. Ces maladies sont caractérisées par une transition progressive des protéines cellulaires d'une structure originelle (structure en hélice α ou aléatoire) vers un état agrégé, structure en feuillets β (fibrilles amyloïdes). Les raisons conduisant les protéines normales à se transformer en agrégats pathologiques sont peu claires. L'augmentation de la concentration physiologique en protéine pourrait être la cause du processus d'agrégation in vivo. Etant donnée la stabilité exceptionnelle de ces agrégats, les stratégies pour le traitement des maladies de changement conformationnel de protéine doivent impliquer la stabilisation des précurseurs de fibrille, ou l'inhibition de l'agrégation en feuillets β commune aux fibrilles amyloïdes.

Dans ce travail, l'interaction du B18 et du peptide β-amyloïde avec des surfaces hydrophobes ou hydrophiles a été caractérisée. En outre, la conformation des peptides en présence d'amphiphiles et de nanoparticules nouvellement synthétisées a été déterminée.

Le peptide B18 est une séquence de la protéine „bindin" de l'oursin de mer, qui est une protéine impliquée dans le processus de fécondation.

Le peptide β-amyloïde résulte du clivage protéolytique de la protéine transmembranaire précurseur d'amyloïde, et est le composant principal des plaques neuronales observées dans le cas de la maladie d'Alzheimer. Les deux peptides montrent une propension élevée à l'agrégation et à la formation de fibrilles amyloïdes.

L'adsorption du B18 et du peptide β-amyloïde a été étudié par des techniques de réflectométrie et de microscopie à force atomique. L'affinité des peptides pour des surfaces peut être une cause de l'augmentation de la concentration locale en peptide qui conduira à l'agrégation. Le B18 et le peptide β-amyloïde se sont adsorbés préférentiellement sur des surfaces hydrophobes et sur des films de charge opposée à la charge nette des peptides. Les peptides ont montré une affinité plus élevée pour les surfaces hydrophobes qui pourraient constituer un lieu approprié pour l'accumulation de peptide et la formation de fibrille.

Les interactions du B18 et du peptide β-amyloïde avec des tensioactifs non ioniques,

cationiques ou anioniques, comportant dans ce dernier cas des chaînes hydrogénées ou perfluorées, ont été caractérisées par dichroïsme circulaire. Une transition d'une conformation aléatoire vers une structure en hélice α a été observée pour le peptide B18 en présence d'amphiphiles chargés à l'état de monomères ou organisés en micelles. Les micelles non ioniques induisent une structure hélicoïdale dans le peptide mais aucune influence n'a été observée dans le cas des monomères. Le peptide β-amyloïde a adopté une structure en hélice α seulement en présence de micelles chargées. Dans une solution de micelles non ioniques, le peptide a montré une structure en feuillet β. Les micelles anioniques comportant des chaînes perfluorées se sont avérées les plus efficaces pour induire une structure en hélice α.

Partant du fait que les alcools fluorés tels que le trifluoroéthanol et que les micelles ioniques, peuvent, à pH physiologique 7.4, conduire à une structure en hélice α (pour ces peptides susceptibles de former des fibrilles), des polyélectrolytes comportant alternativement des motifs cationiques et anioniques ont été complexés avec de l'acide dodécanoïque ou perfluorododécanoïque. Ceci a conduit à la formation de nanoparticules ayant un diamètre hydrodynamique de 4 nm, constituées d'un cur hydrophobe (formé par les chaînes des tensioactifs) et d'une surface hydrophile chargée. Les nanoparticules fluorées induisent les structures riches en hélice α pour le B18 et le peptide β-amyloïde, tandis que leurs analogues hydrogénées se sont avérés moins efficaces, conduisant dans la plupart des cas à la formation de feuillets β ou d'agrégats, ce qui a été déterminé par dichroïsme circulaire. Les nanoparticules fluorées peuvent être des candidats potentiels pour l'inhibition des changements conformationnels menant à la formation de fibrilles amyloïdes. Elles pourraient être particulièrement efficaces dans le cas de protéines à conformation initiale aléatoire en induisant une structure en hélice α, un état non agrégé et stable.

Abstract

Protein misfolding and aggregation are currently being subject of intensive studies. This interest is mainly motivated by the sharp increase in the occurrence of genetic and sporadic amyloidosis and the outbreak of the bovine spongiform encephalopathy, an infectious protein-misfolding disease. These diseases are characterized by a progressive transition from correctly folded proteins (usually in α-helix or random coil structure) into an aggregated state rich in β-sheet structure (amyloid fibrils). The reasons for the conversion of normal proteins into pathological aggregates are still not completely understood. However, it is known that the increase of physiological protein concentration underlies the *in vivo* aggregation process. Moreover, strategies for the treatment of protein misfolding diseases must involve either stabilization of the fibril precursors, or inhibition of aggregation into the cross-β core structure, common to amyloid fibrils, in view of the exceptional stability of the aggregates.

In this work the interaction of B18 and amyloid β-peptide with modified surfaces was characterized. In addition, the conformation of the two peptides in the presence of amphiphiles and in the presence of newly synthesized nanoparticles was determined. B18 peptide is a sequence of the sea urchin protein bindin, which is a protein involved in the fertilization process. Amyloid β-peptide results from the proteolytic cleavage of the transmembranar amyloid precursor protein, and is the main constituent of the neuritic plaques found in Alzheimer's disease. Both peptides show high propensity for aggregation in amyloid fibrils.

The degree of adsorption of B18 and amyloid β-peptide was studied by reflectometry techniques and by atomic force microscopy. Strong peptide affinity for surfaces may be a reason for the local increase in peptide concentration, leading then to aggregation. B18 and amyloid β-peptide were found to adsorb on hydrophobic surfaces and on films with charge opposite to that of the net peptide. The peptides showed higher affinity for hydrophobic surfaces which constitute a potential location for peptide accumulation and fibril formation.

The interaction of B18 and amyloid β-peptide with (i) nonionic, (ii) cationic and (iii) anionic—hydrogenated and perfluorinated—amphiphiles was characterized by circular dichroism spectroscopy. A transition from random coil to α-helix structure was observed for B18 in the presence of charged amphiphiles, in monomeric or micellar state. In the

case of nonionic micelles a partial helical structure is induced in the peptide but no change is observed when monomers are used. Regarding the amyloid β-peptide, only charged micelles can induce an α-helix structure. In nonionic micellar solution, the peptide exhibits a β-sheet structure.

The anionic perfluorinated micelles were the most efficient α-helix inducing agents. Moreover, knowing that fluorinated alcohols, such as trifluoroethanol, and ionic micelles are able to induce α-helix structure in fibril-forming peptides, at physiological pH 7.4, polyampholytes with alternating cationic and anionic monomers were complexed with dodecanoic or perfluorododecanoic acid. This resulted in nanoparticles with hydrodynamic diameters of 4 nm, consisting of a hydrophobic core (formed by the surfactant chains) and a hydrophilic charged shell. The fluorinated nanoparticles induced α-helix rich structures in B18 and amyloid β-peptide, whereas their hydrogenated analogues were less efficient leading in most cases to β-sheet formation or aggregation, as determined by circular dichroism spectroscopy. Fluorinated nanoparticles are proposed to be potential candidates for inhibition of protein conformational alterations that lead to amyloid fibril formation. They could be particularly effective in the case of natively unfolded proteins by inducing α-helix structure, a non-aggregated and stable state.

Acknowledgments

The work presented in this thesis is the fruit of direct collaborations. The research was carried out at the Max Planck Institute of Colloids and Interfaces in Golm (Germany), which is thereby acknowledged for the hospitality. I thank Prof. Helmuth Möhwald for this opportunity and many helpful discussions and suggestions.

Dr. Gerald Brezesinski and Dr. Andreas Thünemann introduced me to the colloid chemistry. I learned a lot from our numerous discussions. Dr. Brezesinski welcomed me in his group at the Max Planck Institute. He was always open and tolerant in discussing the working out of the project. Dr. Thünemann (Federal Institute of Material Research and Testing) was responsible for the synthesis and characterization of the polysiloxane-surfactant complex (chapter 5) and the nanoparticles (chapter 6). I am grateful to them for proposing many new ideas for this work.

I thank Prof. Maria do Carmo Pereira and Prof. Manuel Coelho for accepting me as PhD student in the Faculty of Engineering of the University of Porto, and supervising the work, for their help, suggestions and encouragement.

Some experiments have been conducted with help and assistance of Dr. Rumen Krastev (neutron reflectivity), Paul Lazar (X-ray reflectivity), Anne Heilig (AFM), Heidi Zastrow (electrophoresis), Sérgio Funari (SAXS), Sebastian Schemmel and Robert Lucas (preparation of the hydrophobic films), whom I gratefully acknowledge. Olaf Zschörnig (University of Leipzig) is acknowledged for providing the B18 peptide.

Many thanks to all the members of my group. In particular, to Elena Maltseva, for helping with the preparation of the amyloid peptide samples and for several discussions. Ken-Ichi Iimura and Sandra Gromelski for assistance in the lab.

A special thank to Ana Cordeiro, Chrystelle Egger, Constança Cacela, Paul Lazar, Quézia Paiva, Rivelino Montenegro, Hans Ringström, Mihaela Rusu and Liying Wang for their help and continuous incentive and to Christophe Déjugnat for the french version of the abstract.

I thank Simone Calogero for standing by me with patience and for helping me with physics and Latex. My parents, my sister Annie Rocha, Marco Amador, Marlene Lúcio, Sandra Azevedo and Katiuska Barros for their constant support.

The Portuguese Science and Technology Foundation (FCT) is gratefully acknowledged for a PhD Fellowship (BD/948/2000). These investigations were supported by the Max Planck Society, the FCT research project POCTI/FCB/45365/2002 and German Science Foundation (DFG, Br1378/8).

Contents

1 Introduction

This thesis focuses on the structure of self-assembled peptides. The peptides that are considered, the B18 peptide and amyloid β-peptide, show a strong tendency to self-assemble into amyloid fibrils. Recently most attention has been focused on a group of diseases where proteins form insoluble fibrils which accumulate in a variety of organs including liver, spleen and brain [1, 2]. This group of diseases includes systemic amyloidosis and many neurodegenerative diseases such as Parkinson and Alzheimer's disease [1–3]. The amyloid β-peptide is the subunit of amyloid fibrils of the neuritic plaques that pathologically characterize the Alzheimer's disease [4].

Over 20 proteins and peptides, ranging from intact globular proteins to largely unstructured peptide molecules, are described to self-assemble into amyloid fibrils *in vivo* [1, 5]. Although the amyloid precursor proteins have very heterogeneous structures, the ultrastructural morphology of all amyloid deposits is remarkably similar. The fibrils consist of polypeptide chains organized in a unique cross-β-sheet structure in which continuous β-sheets are formed with β-strands running perpendicular to the long axis of the fibrils [6]. Since the amyloid fibril structure is very much different from the native structure of the proteins, the process of amyloid fibrillogenesis must involve a pronounced protein refolding and highly ordered self-assembly into protofilaments.

The ability to form amyloid fibrils seems to be a generic property of the polypeptide chain. Many other proteins that are not currently associated with diseases, such as muscle myoglobin, as well as many fusion peptides are able to self-assemble into amyloid fibrils. B18 peptide is the minimum membrane binding and fusogenic sequence of the fertilization protein bindin found in sea urchin [7]. The peptide shows a strong tendency to self-assemble into amyloid β-structure at the membrane surface [8]. The propensity to form amyloid fibrils under given circumstances can, however, vary markedly between different sequences. The relative aggregation rates for a wide range of peptides and proteins correlate with the physicochemical features of the molecules such as charge, secondary structure propensities and hydrophobicity [9]. In a globular protein the polypeptide main chain and the hydrophobic side chains are largely buried within the folded structure. Only when they are exposed, the conversion into amyloid fibrils will be possible.

In addition to the ability of self-assembly into amyloid fibrils, B18 and amyloid β-peptide are related by the fact that both have fusogenic properties, both have three his-

tidines and two hydrophobic clusters in their sequences and both are unstructured prior to aggregation into fibrils [5, 7, 8, 10]. Hence they were chosen as models to study the adsorption behavior and conformational changes of fibril-forming peptides in the presence of surfaces, micelles and nanoparticles.

The precise reasons for protein misfolding and deposition and their relation with the pathogenesis of the diseases are not known. The generic nature of amyloid formation suggests that the basis of fibrillogenesis may be the presence of denaturing conditions that destabilize the native protein but non-covalent interactions remain favorable [9]. Conditions such as low pH environments in endosomes associated with protein translocation have been implicated in these diseases [11]. Moreover the majority of the mutations associated with the familial amyloid-related diseases destabilize the normal conformation, and many give rise to intermediates prone to aggregation [12].

Aggregates in Alzheimer's disease are associated with peptide fragments that result from the processing or partial degradation of a precursor protein within the cellular environment [4]. Such peptides are exposed in the cellular environment and their aggregation might result from surface interaction. In addition fibrillization seems, under *in vivo* conditions, to be highly concentration dependent [11]. The interaction with surfaces may contribute to an increase in the local peptide concentration. This hypothesis is explored in the fourth chapter in view of peptide adsorption behavior since their affinity for certain surfaces may lead to an increase in the local peptide concentration which will then result in its aggregation.

Another approach for understanding the mechanisms underlying amyloid fibrillogenesis is to study the peptide conformation in the presence of amphiphiles. This is the subject of the fifth chapter of this thesis. In this chapter the interaction of B18 and amyloid β-peptide with amphiphiles—monomers and micelles—is considered. Several amyloidogenic proteins and peptides including amyloid β-peptide derive from transmembranar proteins [4]. Others such as B18 peptide derive from proteins that are functional at membrane surfaces [13]. Their amphipathic character makes them a target for membrane-associated toxic events. In particular studies with the amyloid β-peptide have shown that neuronal lipid membranes might be involved in its conversion into toxic oligomers [14]. This suggests that the interaction of amyloidogenic proteins with cellular membranes might be involved in the onset and development of the protein misfolding diseases.

Many evidences support that accumulation of amyloid β-peptide represents an early event of Alzheimer's disease [15]. Familial mutations that lead to an increase in the amyloid β-peptide concentration or to its aggregation increase neuropathogenicity. In addition, the fibrillar and oligomeric form of the peptide are found to be toxic to cultured cells. Hence therapeutic strategies that can decrease the accumulation of misfolded proteins might prove to be useful in treating or preventing more than one of the diseases associated with protein misfolding. Stabilization of the protein native state or inhibiting monomer-

monomer binding are particularly attractive strategies, considering the emerging evidence that small misfolded oligomers are neurotoxic [2]. With this perspective, colloidal nanostructures of charged polyampholytes and fluorinated amphiphiles were engineered. This constitutes the subject of the sixth chapter. The influence of fluorinated and corresponding hydrogenated nanoparticles on the peptide structure is considered. Based on the fact that fluorinated alcohols and negatively charged micelles made of sodium dodecyl sulphate induce α-helix conformation in fibril-forming peptides, complexes of polyelectrolytes and perfluorododecanoic acid were prepared. Combining polyelectrolytes with surfactant chains, highly charged particles are expected to be formed, which might enhance the helix inducing effect. Additionally it is possible that the critical aggregation concentration will be quite low, which is important when considering the possible toxicity of micelle structures. The characterization of the nanoparticles and their influence on the structure of B18 and amyloid β-peptide will be described.

The two chapters following this introduction yield an overview of protein folding and misfolding, and their relation to diseases and the main methods used in the present work. The last chapter summarizes the main conclusions of this thesis.

2 Folding and Self-Assembly of Peptides and Proteins

The formation of protein aggregates is observed in several diseases. A protein aggregates as a consequence of an aberrant folding or an alteration of its native structure. Misfolded or aggregated proteins may be related to diseases by either the absence of biological activity or by a gain of toxic activity. Therefore understanding the misfolding and aggregation mechanisms is essential for developing therapeutic strategies for diseases associated with protein deposition. Inhibiting the formation of protein aggregates may be of major importance for treating these diseases.

2.1 Protein Folding

The biological function of a protein depends on its three-dimensional structure (tertiary structure) which is determined by its amino acid sequence (primary structure) and the cellular environment surrounding the polypeptide chain [16]. Proteins have a unique sequence that results from a combination of the 20 natural amino acids (Table 2.1) [17].

Proteins are synthesized *in vivo* as linear polypeptide chains, but they rapidly fold into their final conformation. During folding adjacent amino acid residues in the linear sequence adopt regular structures (secondary structure). The tertiary structure is then formed by packing secondary structural elements into one or several domains. Some proteins contain several polypeptide chains arranged in a quaternary structure.

Even though the protein structure is encoded in the amino acid sequence, the mechanism of folding is not well understood. This is because there is a complex balance between forces that stabilize and destabilize the formation of the three-dimensional protein structure. In biological cells, where most of the volume is occupied, the probability of a protein to aggregate during folding is largely enhanced. Therefore, many newly synthesized proteins require molecular chaperones to direct or facilitate the folding process in the cell [18]. Only small proteins that fold rapidly do not require chaperones. Molecular chaperones are specific proteins that interact with hydrophobic groups of partially folded intermediates of target proteins. Their cellular functions include capturing misfolded states and allow them to fold, protecting proteins from aggregation as a con-

Code	Name	Side chain	Character	pK
A	Alanine	-CH_3	Neutral	
R	Arginine	-$CH_2CH_2CH_2NHCNH_2NH_2$	Basic	12.0
N	Asparagine	-CH_2CONH_2	Neutral	
D	Aspartic acid	-CH_2COOH	Acid	4.4
C	Cysteine	-CH_2SH	Neutral	8.5
Q	Glutamine	$CH_2CH_2CONH_2$	Neutral	
E	Glutamic acid	-CH_2CH_2COOH	Acid	4.4
G	Glycine	-H	Non-polar	
H	Histidine	-CH_2IMIDAZOLE	Neutral, basic	6.5
I	Isoleucine	-$CH(CH_3)CH_2CH_3$	Non-polar	
L	Leucine	-$CH_2CH(CH_3)_2$	Non-polar	
K	Lysine	-$CH_2CH_2CH_2CH_2NH_3$	Basic	10.0
M	Methionine	-$CH_2CH_2SCH_3$	Non-polar	
F	Phenylalanine	CH_2PHENYL	Non-polar	
P	Proline	-$CH_2CH_2CH_2$[N]	Non-polar	
S	Serine	-CH_2OH	Neutral	
T	Threonine	-$CH(CH_3)OH$	Neutral	
W	Tryptophan	-CH_2INDOLE	Non-polar	
Y	Tyrosine	-CH_2PHENOL	Neutral	10.0
V	Valine	-CH-CH_3CH_3	Non-polar	

Table 2.1. The natural amino acids: abbreviation codes, side chains, and character of the ionic forms, predominant at pH 6–7. The pK values given are of the ionizable side chains [17]. The general structure of amino acids is H_2N-C_αHR-COOH, where R is the side chain. An exception occurs with proline where the side chain is bridged to the nitrogen atom of the amino group.

sequence of cellular stress, and cooperating in protein degradation. If folding is unsuccessful, the protein is directed to the proteasome—a large protease—for degradation [19]. Ensuring accurate protein folding is essential for normal cellular function.

2.1.1 Thermodynamics and Kinetics of Protein Folding

A protein sequence must satisfy two requirements for folding, one thermodynamic and one kinetic [20]. The thermodynamic requirement is that the protein adopts a unique folded conformation (the native state) which is stable under physiological conditions. The kinetic requirement is that the denatured polypeptide chain can fold into the native conformation within a reasonable time.

The Gibbs free energy, G, is given by the equation

$$G = H - TS, \tag{2.1}$$

where H represents the enthalpy, T is the temperature and S is the entropy. The contributions to the free energy of folding arise from internal interactions and hydrophobic interactions, which are energetically favorable, and conformational entropy, which is energetically unfavorable.

The dominant forces that stabilize the protein structure are hydrogen bonds, electrostatic and van der Waals attractions, hydrophobic interactions and disulfide bonds [21]. In hydrogen bonds, the hydrogen atom is shared between two electronegative atoms, which in biological systems are oxygen and nitrogen. The bond energy ranges from 3 to 7 kcal/mol and the bond length is in the order of 3 Å. In electrostatic attractions a charged group of a molecule is attracted by an oppositely charged one. The bond energy is in the same range as that of the hydrogen bonds. The distance between two oppositely charged atoms is about 2.8 Å. Van der Waals bonds are nonspecific attractive forces that arise from interactions among induced dipoles. The atoms involved in these bonds are 3 to 4 Å distant from each other. The van der Waals bond energy is about 1 kcal/mol. Hydrophobic interactions are attractions between non-polar molecules or groups that tend to cluster in water. Disulfide bonds are formed between chains or between parts of a chain by the oxidation of cysteine residues.

The non-polar groups strongly favor the folded state due to the attractive van der Waals interactions and the hydrophobic effect, which favors the burial of non-polar groups [20]. The strong tendency of hydrophobic residues to be excluded from the water results in a large entropy gain. By contrast, the polar groups make a much smaller contribution to the stability of the native state owing to a balance of the interactions in the interior of the protein and those with the solvent [20].

The opposing force of folding arises principally from the loss of conformational entropy due to steric constraint in the folded state [21]. This is due to the fact that the conformation space available to the polypeptide main chain and side chains is much more restricted in the native state than in the denatured state. Proteins, as polymers, are subject to a type of configurational entropy that arises from the excluded volume, which is described as the impossibility of two chain segments to simultaneously occupy the same volume of space. There are relatively few ways the chain can configure if it is forced to occupy a small volume of space due to steric constraints. Native states of proteins are extremely compact. Because protein folding involves arrangement of chains from a large volume (unfolded state) to a small volume (native state), a considerable amount of entropy is lost in the process.

The free energy of the native state of a protein is only slightly lower than that of the denatured state under physiological conditions. The free energy change $\Delta G_{unfold} = G_{denatured} - G_{native}$ is typically 5 to 20 kcal/mol of protein [22]. This relatively low energy difference allows conformational flexibility which is required for protein function such as store and transport molecules, catalyze chemical reactions, transmit information between cells, control passage of molecules across membranes, bind to specific molecules. Nevertheless, in physiological conditions, the stability of the native state is greater than that of the denatured state. This is because the conformational entropy is outweighed by other effects, particularly hydrophobic interactions between non-polar groups. This

means that the protein folds so that its hydrophobic amino acids are clustered in the interior of the molecule and the polar, charged chains are on the surface. The 20 amino acids show varying degrees of hydrophobicity, and this has important consequences for protein folding [23].

An additional determinant of protein folding is the intrinsic structural preference for different secondary structure elements of the chain that already exists in the random coil state [20]. Under native conditions short-range interactions can give rise to structural features such as nascent helices which act as initiation sites to increase the probability of coalescing to structures involving longer range contacts.

Hydrophobic interactions are thought to be responsible for the unique native structure that is encoded by the amino acid sequence. There is a small number of configurations that allow a chain to configure in order to maximize the number of non-polar contacts [21].

In spite of the large number of possible conformations that a polypeptide chain can adopt, the folding process occurs in a short time scale from 10^{-1} to 10^{3} seconds. Therefore there must be folding pathways which allow the process to proceed rapidly. In fact proteins do not fold by sampling all possible conformations randomly but rather by progressive stabilization of intermediates [24]. During protein folding partially correct intermediates are retained, decreasing the time for folding. The process is complex since correct intermediates can be lost because of the small difference in the free energy of the folded and unfolded states. Small proteins fold without populating intermediates in a two-state transition process. In this case folding is thought to begin with a few native-like contacts that promote a rapid transition to the native state.

The energy landscape of folding is funneled towards the native state, which means that denatured molecules can fold by different pathways but all converge to the same native state. The unfolded protein forms intrachain contacts, lowering its free energy. The number of conformations that the protein can sample is progressively reduced until it reaches the unique native state at the energetic minimum. For large proteins, some pathways involve transient intermediates (local energy minima) whereas others involve significant kinetic traps (misfolded states). Intermediate species, which are partially folded states, are able to interact specifically with each other to form aggregates. Molecular chaperones are therefore essential for protein folding *in vivo* since they prevent the formation of kinetic traps or their aggregation.

2.1.2 Protein Secondary Structures

The secondary structures are regular elements of a protein structure and consist of α-helices, β-strands and β-turns (Figure 2.1) [25]. The unordered arrangements as well as structures that cannot be classified within the standard classes are known as random coil conformation.

The α-helix is a rod-like structure stabilized by hydrogen bonds between the CO group

of an amino acid and the NH group of the amino acid that is situated four residues ahead in the linear sequence. Each amino acid is related to the next one by a rise of 1.5 Å along the helix axis and a rotation of 100°, which gives 3.6 amino acid residues per turn of helix. This results in a distance per turn of 5.4 Å. Variations of the α-helix structure are 3_{10} and π-helices. In 3_{10}-helices the chain is more tightly packed with hydrogen bonds between residues n and n+3, whereas π-helices are more loosely packed stabilized by hydrogen bonds between residues n and n+5. The 3_{10}-helices are rare and the π-helices very unfavorable. A substantial amount of 3_{10}-helices occurs at the ends of α-helices.

The β-sheet is an almost fully extended structure stabilized by hydrogen bonds between CO and NH groups of amino acids of different polypeptide chains, called β-strands. The axial distance between amino acids is 3.5 Å. Adjacent β-strands may be orientated in the same direction, parallel β-sheet, or in opposite directions, antiparallel β-sheet. The classical β-sheets originally proposed are planar but most sheets observed in proteins are twisted.

In the β-turn structure the direction of the polypeptide chain is reversed. The structure is stabilized by hydrogen bonds between the CO group of the residue n and the NH group of the residue n+3 of a polypeptide chain.

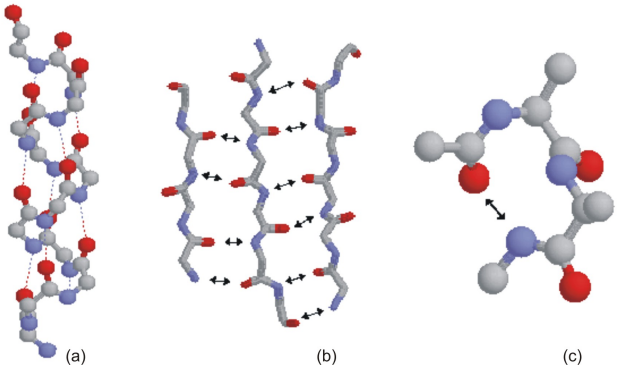

Figure 2.1. Ordered secondary structures in polypeptide chains: (a) α-helix; (b) antiparallel β-pleated sheet and (c) β-turn.

Proteins contain mainly α-helices and β-sheet structures (typically more than 60%). The shape of these structures determines the compact structure of the molecule.

The secondary structure of a polypeptide chain is specified by the degree of rotation of the backbone bonds in the peptide unit. Two (C_α-C and C_α-N) of the three backbone bonds are free to rotate (Figure 2.2). The degree of rotation can be predicted by diagrams called Ramachandran plots [25]. In theory a polypeptide chain can adopt an essentially infinite variety of conformations, corresponding to a unique set of values for the rotation angles of the backbone. However, many conformations can be excluded due to unfavorable steric overlaps. The peptide C-N bond is fixed and planar because of its partial

double-bond character.

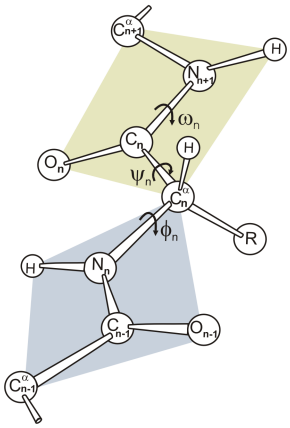

Figure 2.2. The geometry of a polypeptide chain segment comprising two peptide units. The notations for atoms and torsion angles are indicated; ψ refers to a rotation of the plane shown in yellow about the C_α-C bond and ϕ refers to a rotation of the plane shown in blue about the C_α-N bond.

Amino acid residues possess conformational preferences. The residues alanine, glutamate and leucine have tendency to be involved in α-helices. Valine and isoleucine have propensity for forming β-strand structure. Glycine, asparagine and proline promote the formation of turns. However, conformational preferences are only marginally, which makes the prediction of a protein structure difficult. Additionally, the structure of a polypeptide chain is not determined by a single residue. Interactions between residues that are distant from each other may significantly influence the final secondary structure.

2.2 Protein Misfolding and Aggregation

The process that ensures the correct folding of proteins and degradation of malfunctioning proteins *in vivo* is highly selective and precisely regulated. However, if this process fails, misfolded proteins, which are potentially toxic, can accumulate in tissues or organs and cause diseases.

Protein misfolding is an alteration of its secondary or tertiary structure that results in malfunction. Misfolded proteins are particularly prone to aggregation because hydrophobic residues that are normally buried are exposed on their surfaces. In many cases, misfolded proteins associated with disease are aggregated in the form of fibrils or amorphous deposits. Amyloid fibrils are one of the types of aggregate that can be formed by proteins. These aggregates are highly organized structures stabilized by hydrogen bonds.

2.2.1 Protein Misfolding Diseases

Several diseases have been associated to protein misfolding and aggregation [1, 3]. The hallmark feature of protein misfolding diseases is a change in the native structure of a protein without alteration of the primary structure. The misfolded protein aggregates and accumulates in tissues as insoluble amyloid deposits (Figure 2.3). In addition to the aggregated protein, amyloid deposits are characteristically rich in carbohydrates, particularly glycosaminoglycans.

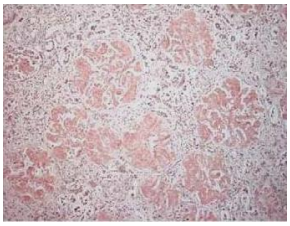

Figure 2.3. Renal amyloid deposits as demonstrated by Congo red staining. Adapted from [26].

There is a large secondary structural difference between the native protein and the aggregated material. In general the native protein exists in α-helical and unordered structures, whereas the misfolded protein is rich in β-sheet structure. While in α-helices the hydrogen bonds that stabilize the structure are between CO and NH groups of the same strand, in β-sheets the bonds are between CO and NH groups of different strands. Since the second strand can come from a different region of the same protein or from a different molecule, formation of β-sheets is usually stabilized by protein oligomerization or aggregation, which indeed occurs in protein misfolding related diseases. Although amyloid-forming proteins do not share clear sequence homology, the fibrillar structures have similar physicochemical and ultrastructural characteristics [6].

Another general feature of misfolding diseases is the prolonged period before clinical manifestations appear. There is a prolonged preclinical phase during which proteins misfold, aggregate and progressively compromise cellular and tissue functions [1].

The major representatives of these disorders are systemic amyloidoses that are accompanied by progressive extracellular deposition of proteins in multiple organs including liver, spleen, kidney and heart. Amyloidosis can be secondary to other pathological conditions that cause an increase in the concentration of an amyloid-prone polypeptide, as occurs for the serum amyloid A protein during the acute-phase response accompanying inflammatory disorders such as rheumatoid arthritis. Primary systemic amyloidosis involves progressive multi-tissue deposition of immunoglobulin light chains and their fragments.

In recent years, evidences have emerged indicating that prevalent neurodegenerative diseases also involve a protein-folding problem with deposition of protein aggregates in

the brain [3]. This group includes Alzheimer's disease, Parkinson's disease and transmissible spongiform encephalopathies (Table 2.2). Alzheimer's disease is the most common neurodegenerative disorder and is characterized by the accumulation of proteins both extracellularly (amyloid β-peptide) and intracellularly (tau protein). The clinical and neuropathological features of the disease are described below. The pathological features of Parkinson's disease, the second most common, are intracytoplasmatic inclusions called Lewy bodies that contain mainly fragments of α-synuclein protein. Transmissible spongiform encephalopathies are characterized by accumulation of abnormal prion proteins. The most common is the Creutzfeldt-Jakob disease. These diseases can be sporadic, inherited or infectious and are manifested usually later in life. They are pathologically characterized by neuronal loss in motor, sensory or cognitive systems, and affect movements, memory, emotions, cognition, and other abilities [27].

Disease	**Clinical features**	**Protein**	**Cellular location**
Alzheimer's disease	Progressive dementia	Amyloid β-peptide Tau	Extracellular plaques Tangles in neuronal cytoplasm
Parkinson's disease	Movement disorder	α-synuclein	Lewy bodies in neuronal cytoplasm
Creutzfeldt-Jakob disease	Dementia, ataxia Physiatric problems	Prion protein	Extracellular plaques Oligomers in neurons
Amyotrophic lateral sclerosis	Movement disorder	Superoxide dismutase	Deposits in neuronal cytoplasm
Huntington's disease	Dementia, motor and physiatric problems	Long glutamine stretches	Deposits in neuronal nuclei and cytoplasm

Table 2.2. Clinical and neuropathological features of neurodegenerative diseases.

The precise reasons for protein misfolding and deposition and their relation with the pathogenesis of the diseases are not known. In some cases of systemic amyloidoses the deposits are in such large amounts that they lead to organ malfunction simply by physical presence. However, amyloid fibrils or more likely low molecular weight amyloid aggregates may directly compromise cell function [2].

Alzheimer's disease

Clinical and neuropathological features

The initial clinical symptoms of Alzheimer's disease are almost imperceptible and typically involve lapses of memory for recent facts and poor judgment [28]. The performance of complex work tasks and ability to acquire new information may be reduced. After a couple of years cognitive functions are affected and patients show spatial disorientation,

apathy, general disinterest and difficulty in performing simple tasks such as preparing meals or managing bank accounts. Patients frequently lose emotional control which may be accompanied by physical or verbal aggression. Symptoms of depression may prevail in the early stage of illness. With progression of the disease, patients develop motor problems showing difficulty for walking and manual activities like writing. Recent memory is severely affected. Over several years, the disease leads to a gradual deterioration of the patients life who manifest a marked dementia with profound memory and cognition losses. Many patients become immobile and succumb to respiratory difficulties.

Alzheimer's disease is neuropathologically characterized by neuritic plaques and neurofibrillary tangles in the brain, particularly in regions related to memory and cognition [29]. The neuritic plaques are spherical extracellular lesions that consist of deposits of amyloid β-peptide fibrils surrounded by dystrophic axons and dendrites, activated microglia and reactive astrocytes. Amyloid plaques deposit in brain parenchyma and around cerebral vessel walls. In the same brain regions, diffuse plaques are observed in much larger number. They consist of amorphous extracellular deposits of amyloid peptide (material that lack of fibrils). Diffuse plaques appear to represent an earlier stage of neuritic plaques. Neurofibrillary tangles are helical paired filaments composed largely of abnormal microtubular tau protein. These fibers are found in the cytoplasm of neurons. There are no peripheral biochemical markers for the disease and confirmation still requires postmortem observation of the classical lesions.

At the moment, no therapies have been clinically proven to prevent the progression of Alzheimer's disease. Treatments used are largely symptomatic.

2.2.2 Amyloid Fibril Formation

Amyloid describes proteinaceous aggregates. The amyloid structure is characterized by straight, unbranched fibrils, about 100 Å in diameter and of indefinite length, composed of filamentous subunits (protofilaments) with a diameter varying from 25 to 35 Å [6]. An electron micrograph of amyloid fibrils formed *in vitro* is shown in Figure 2.4.

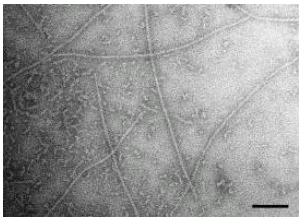

Figure 2.4. Electron micrograph of amyloid fibrils formed *in vitro* from amyloid β-peptide showing long straight fibrils as well as fibrillar aggregates. The scale bar is 1000 Å. Adapted from [30].

The fibrils consist of polypeptide chains organized in a β-sheet conformation. The

extended β-sheets run parallel to the axis of the fibril, and their components, β-strands (polypeptide chains), are arranged perpendicular to this axis (Figure 2.5). This structure is known as the cross-β-conformation. The protofilaments are usually composed of more than one β-sheet, stacking face to face, with an intersheet spacing of approximately 10 Å. The spacing between the adjacent β-strands is about 4.7 Å [6]. All amyloid fibrils bind to Congo red dye and generate a characteristic green birefringence when examined under cross-polarized light.

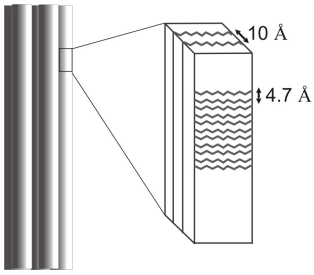

Figure 2.5. Molecular model of an amyloid fibril consisting of 5 protofilaments. The protofilaments are composed of β-sheets with spacing of 10 Å. The adjacent β-strands that compose the β-sheets are separated by 4.7 Å.

Over 20 unrelated proteins form amyloid fibrils *in vivo* [1, 5]. In addition proteins, for which no amyloid associated disease has been identified, can aggregate into fibrils under appropriate conditions [31–33]. Formation of amyloid fibrils may be a generic property of polypeptide chains, since the intermolecular bonds that stabilize the fibrils involve the peptide backbone, which is common to all proteins. Thus, the amyloid state may be accessible to any protein as a very stable alternative conformational state. Indeed the aggregated state can be under certain conditions even more stable than the native state [32]. Despite this fact, in biological systems the amyloid formation is restricted to a group of proteins and not all form this type of aggregates. The cellular environment is such that the denaturation of proteins does not normally occur under conditions where unfolded chains tend to aggregate [2]. The pH and temperature are carefully controlled, and molecular chaperones are present to prevent aggregation.

The basis for fibril formation may be the presence of denaturing conditions that destabilize the native protein fold, but non-covalent interactions remain favorable [9]. In fact genetic and environmental factors have been associated to fibril formation [3]. Mutations in the genes that encode the proteins of the fibrillar aggregates can lead to a destabilization of the normal protein conformation, favoring aggregation. Oxidative stress, changes in metal ions, pH and concentration of the protein are other possible causes for protein aggregation. Many of these alterations are associated with aging [34].

Studies have demonstrated that fibril formation follows a nucleation mechanism, with formation of instable intermediates that act as seeds [35–37]. At least two intermediates

have been identified during amyloid formation [38,39]. The first intermediates are soluble and of low molecular weight, composed of monomeric or dimeric peptide molecules. The second intermediates, the protofibrils, are short, flexible fibrils, generally 4–10 nm in diameter and up to 200 nm long. Protofibrils form amyloid fibrils and have similar characteristics to the mature fibrils; a β-sheet structure and capacity to bind Congo red dye.

Amyloid fibrils and in particular their precursor assemblies (oligomers and protofibrils) affect the normal metabolism of cultured cells [40]. As well early aggregates formed by non-disease-associated proteins were found to be highly cytotoxic [41].

2.3 Self-Assembled Peptides

In this section two distinct molecules, B18 peptide and amyloid β-peptide, that self-assemble into amyloid fibrils, are described.

2.3.1 B18 Peptide

B18 peptide is the amino acid sequence 103 to 120 of the protein bindin, which is found in the membrane of sperm cells of *strongylocentrotus purpuratus* (purple sea urchin) [13]. Bindin plays a key role in the fertilization process and the sequence B18 is recognized as the minimal membrane binding and fusogenic motif [7, 13]. These 18 amino acids are perfectly conserved among all known sea urchin species. The amino acid sequence and amphipathicity of B18 is shown in Figure 2.6.

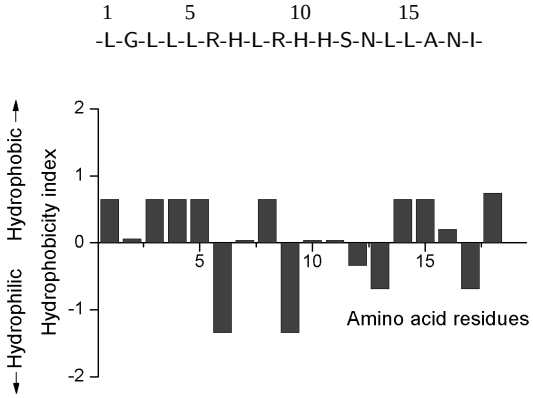

Figure 2.6. Amino acid sequence and schematic representation of the amphipathicity of B18 peptide using Miller et al. scale [23].

In biological cells fusion of membranes is induced by proteins [42]. Fusion is essential in physiological processes such as fertilization, intracellular vesicle traffic and muscle

development. However, it can also be part of a pathogenic process such as in viral infections. Viral fusion proteins promote infection by mediating fusion between viral and cellular membranes.

Fusion proteins contain a short hydrophobic sequence of 12 to 30 amino acid residues, known as fusion peptide, that interacts directly with the membrane [43]. The amino acid composition of fusion peptides shows a predominance of glycine, alanine and threonine and aliphatic hydrophobic residues (valine, leucine, methionine).

Fusion peptides exhibit a polymorphic structural behavior, which seems to be crucial for the fusion process. Evidences suggest that the fusion-promoting state is the α-helix structure [44]. It is proposed that the peptides are initially in a random coil conformation and adopt an α-helix structure when inserted in the membrane. Certain viral fusion peptides have a strong tendency to self assemble into amyloid β-structures at the membrane surface. Although self-association may contribute to the recruitment of more peptides to the fusion site, its functional relevance is not known.

B18 peptide is able to induce aggregation and fusion of neutral lipid vesicles, which is strongly enhanced by zinc ions [7]. Zinc induces an α-helix conformation in the peptide molecule by binding to histidine residues 7 and 11, resulting in the formation of oligomeric metallo-peptide complexes [45]. The high affinity of B18 peptide for membranes was attributed to hydrophobic interactions since the peptide has hydrophobic side chains at both ends of the molecule.

B18 peptide exhibits a high conformational flexibility and can adopt α-helix, random coil or β-sheet conformation depending on solution conditions [46]. At neutral pH, the peptide shows a strong tendency to self assemble and to form fibrils, consisting of twisted ribbons that are assembled from three to five protofilaments with widths of about 5 nm each [8]. The fibrils have a cross β-sheet conformation and stain positively to Congo red dye, similar to amyloid fibrils. Studies of B18 peptide upon binding to lipid membranes revealed an oligomeric β-sheet structure [47].

There is a structural homology between fusion peptides and sequences of amyloidogenic peptides [43]. Moreover fusogenic properties have been described for prion peptides and amyloid β-peptide [10, 48]. These properties are thought to contribute to the neurotoxicity of amyloidogenic peptides by destabilizing cellular membranes.

Peptides related to amyloid diseases, consisting of short sequences of 12 to 20 residues, have been shown to self assemble into amyloid fibrils with similar ultrastructure of the amyloid from larger polypeptides and proteins [49, 50]. Hence, short peptides such as B18 constitute ideal model systems to study conformational changes and fibrillization *in vitro*.

2.3.2 Amyloid beta-Peptide

Amyloid β-peptide is the subunit of amyloid fibrils that form the neuritic plaques found in Alzheimer's disease [51]. The peptide accumulates in the small blood vessels of the meninges and cerebral cortex [52]. The non fibrillar form of the peptide is found in amorphous extracellular deposits (diffuse plaques) [53]. The peptide, with N- and C-terminal heterogeneity, occurs in two principal lengths: 40 or 42 amino acids long. The neuritic plaques appear to contain a mixture of the 40 and the 42 residues form. The diffuse plaques are almost exclusively composed of the amyloid β-peptide (1–42), and the cerebrovascular deposits contain mainly the 40 residues form.

The amyloid β-peptide, a 4.3 kDa molecule, is a product of proteolytic cleavage of a transmembranar protein, the amyloid precursor protein, which is encoded by a gene on chromosome 21 [54]. The peptide includes 28 residues outside the membrane and 12–14 residues derive from the transmembranar region of the precursor protein (Figure 2.7).

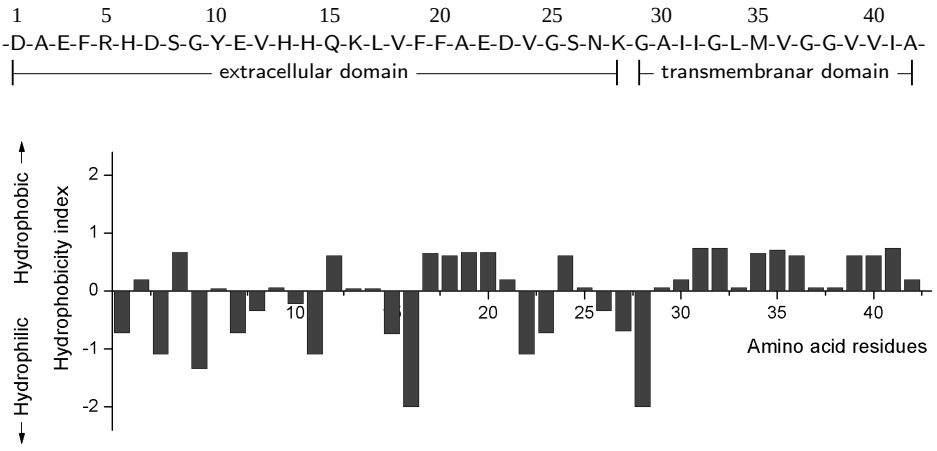

Figure 2.7. Amino acid sequence and schematic representation of the amphipathicity of amyloid β-peptide using Miller et al. scale [23].

The amyloid precursor protein comprises a heterogeneous group of polypeptides of 110 to 140 kDa widely expressed in neurons and non neuronal cells. The metabolism of the precursor protein can be processed by two alternative proteolytic events (Figure 2.8) [55]. The proteolytic cleavage by α-secretase is the most frequent and results in the release of a large soluble ectodomain fragment into the extracellular space and the retention of a fragment of 83 residues in the membrane. This fragment can be cleaved by γ-secretase, generating the peptide p3. Other precursor molecules can be cleaved by β-secretase, yielding a smaller ectodomain derivative and a fragment of 99 residues, which is retained in the membrane. The subsequent cleavage of this fragment by γ-secretase produces the amyloid β-peptide.

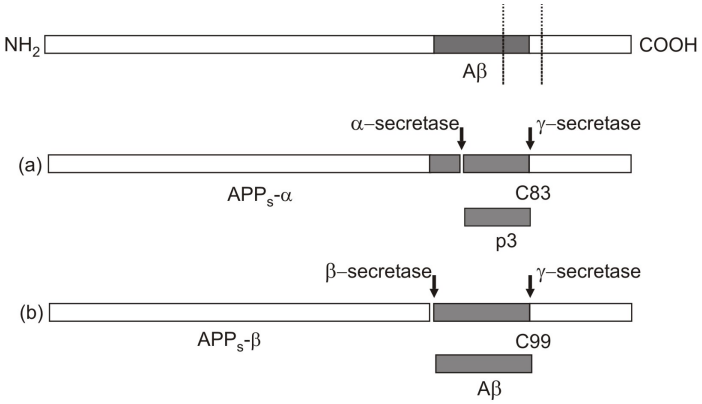

Figure 2.8. Schematic diagram of the amyloid precursor protein processing. Two alternative proteolytic events are shown: (a) The cleavage by α-secretase originates a large ectodomain (APP_s-α) and an 83 residues fragment. The subsequent γ-secretase cleavage produces the p3 peptide; (b) The β-secretase cleavage generates a smaller ectodomain (APP_s-β) and a 99 residues fragment, which after cleavage by γ-secretase releases the amyloid β-peptide (Aβ).

Since amyloid β-peptide has a hydrophobic character and is part of a membranar protein, the finding of soluble peptide in biological fluids was not expected. However, the peptide is continuously secreted by normal cells in culture and is detected as a circulating peptide in the plasma and cerebrospinal fluid of healthy individuals [56, 57]. The 40 residues form is normally the more abundantly produced by cells.

Considering that amyloid β-peptide is a normal metabolic product, a change in the balance between its production and clearance could increase its levels and lead to amyloid deposition. The basis of the peptide accumulation is not completely known. Likewise, whether the peptide deposition is a cause or an effect of Alzheimer's disease is not clear. However, strong evidences indicate that amyloid β-peptide accumulation represents an early event in the pathogenesis of the disease and may be responsible for the brain abnormalities that characterized the disease [15, 58]. A schematic representation of the amyloid cascade hypothesis is shown in Figure 2.9. This hypothesis is largely supported by genetic studies [4]. Mutations found to be causative of Alzheimer's disease such as mutations in amyloid precursor gene increase the cellular production of amyloid β-peptide and its accumulation. In Trisomy 21 (Down's syndrome) there is an overexpression of normal amyloid precursor protein owing to elevated gene dosage that leads to premature occurrence of classical Alzheimer's disease neuropathology at an early age. Studies with transgenic animal models have shown that overexpression of wild type or mutant human amyloid precursor protein results in development of pathological and clinical hallmarks of Alzheimer's disease including amyloid plaques and cognitive behavior alterations [59]. Additionally it was observed that the fibrillar and the oligomeric forms of the peptide, but

not the monomeric form, cause changes in cultured neurons or microglia [60, 61]. This observation agrees with the fact that amyloid β-peptide is produced by healthy cells and that neuronal injury appears to be associated with aggregated forms.

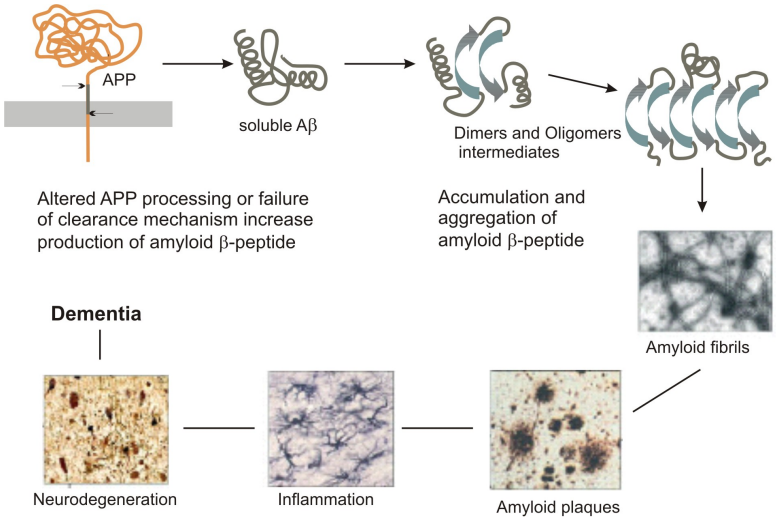

Figure 2.9. Amyloid peptide cascade hypothesis of Alzheimer's disease. The first pathological alteration of the disease seems to be the misfolding and aggregation of amyloid β-peptide (Aβ), after its release from the amyloid precursor protein (APP). Adapted from [58].

For the development of therapies for Alzheimer's disease, it is important to understand the relation between amyloid fibril formation and the mechanisms involved in assembly of amyloid β-peptide. Amyloid deposits isolated from Alzheimer's disease brain tissue are in a β-pleated sheet conformation where the β-strands run perpendicular to the fiber axis [62]. However, the peptide is described to exist in distinct states of aggregation in different lesions of the disease [63]. *In vitro* studies have shown that the peptide can exist in monomeric, dimeric or oligomeric forms depending on solution conditions [64, 65]. The monomeric form exists in α-helix or random coil conformation, whereas the dimeric and oligomeric forms are in a β-sheet structure. It was found that during fibrillogenesis the peptide undergoes a conformational transition from a random coil structure to a β-sheet structure, during which a transitory α-helix component is detected.

Synthetic amyloid peptides spontaneously form fibrils composed of continuous β-sheet structure [66] similar to the *in vivo* amyloid fibrils [62]. *In vitro* studies have established conditions that promote amyloid β-peptide aggregation such as long incubation times, high concentration of the peptide and pH range of 4 to 7 [64, 65]. Additionally assembly studies of short fragments and amino acid substitutions in the peptide sequence have provided information about the relation between the peptide sequence and its aggregation properties [49, 67–70]. The studies clearly showed that a significant proportion of

the amyloid β-peptide aggregation is driven by the hydrophobic sequences, the internal domain comprising residues 17 to 21 [67, 70] and the C-terminal region corresponding to the residues 29 to 42 [49, 68]. Electrostatic interactions have also been implicated in the formation and stabilization of amyloid fibrils [69].

Amyloid β-peptide fibrillogenesis is described as a nucleation-dependent polymerization process [35, 36]. The kinetics of this process is controlled by two parameters, the nucleation rate and the elongation rate. Nucleus formation requires a series of association steps that are thermodynamically unfavorable. Once the nucleus is formed the addition of monomers becomes thermodynamically favorable, resulting in rapid growth. A simple mechanism is shown in Figure 2.10.

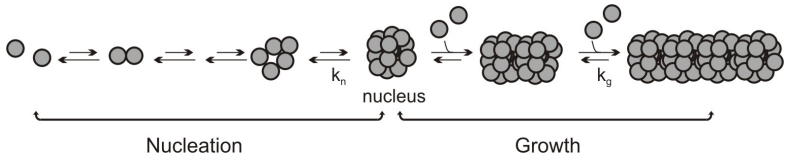

Figure 2.10. Scheme of a simple mechanism for nucleation-dependent polymerization: monomers self-associate to form the nucleus at a rate K_n; addition of monomers to the nucleus at a rate k_g results in rapid polymerization.

It is proposed that nucleation of amyloid β-peptide fibrillogenesis is induced by other peptide molecules (homogeneous nucleation) or by impurities (heterogeneous nucleation) [36]. In the first case, the nucleation begins when the peptide exceeds a certain critical concentration leading to a spontaneous self-assembly of peptide monomers into aggregates, which act as a fibril nuclei (seeds). The detailed structure of the peptide nucleus was determined to be elongated with a radius of 2.4 nm and a length of 11 nm and consisting of 30 to 50 monomers [71]. Alternative pathways, including seeding on impurities, may exist for the formation of fibril nuclei, when the peptide concentration is below the critical concentration [36]. Nucleation is followed by fiber elongation, with a rate proportional to the peptide monomer concentration. Structural and kinetics analysis have shown that during fibrillogenesis amyloid β-peptide forms three different species, dimer, protofibril and fiber [38]. The dimer and protofibril forms are considered intermediates of fibril formation [40]. Based on the nucleation-dependent polymerization process, the formation of protofibrils could be explained as a result of the linear growth of the fibril nuclei, which would be formed by a combination of monomeric and dimeric forms. The protofibrils would then give rise to the mature fibrils [38].

The advances in understanding the molecular basis of Alzheimer's disease with the delineation of the amyloid β-peptide hypothesis predict therapeutics based on preventing the peptide accumulation. Approaches of particular interest are the use of β or γ-secretase inhibitors and anti-aggregation compounds that bind to peptide monomers and prevent their assembly and conformational transitions [4, 72]. However, it is likely that β or

γ-secretases cleave many other proteins, which might be essential for cell functioning. Thus inhibiting these enzymes may have toxicological effects. Aggregation inhibitors are attractive therapeutic approaches since they could be synthesized specifically for amyloid β-peptide or for stages of fibril formation that are shared between different amyloid types. Since precursor intermediates of amyloid fibrils were found to be toxic, inhibition of amyloid formation should be directed to the early steps.

3 Peptides and Methods

3.1 Peptides

B18 peptide (M_w = 2090 g/mol) was provided by Olaf Zschörnig from the University of Leipzig. The peptide was synthesized according to standard Fmoc protocols and purified by reverse phase high pressure liquid chromatography. The purity and the mass were checked by electrospray mass spectrometry and the amount of lyophilized peptide was determined gravimetrically. B18 peptide is blocked at the C-terminus with an amide group. Stock solutions were prepared by dissolving B18 in double distilled water, where the peptide is fully soluble and does not self-aggregate. The solution was then diluted with different buffers in order to obtain the desired pH.

Amyloid β-peptide (1–40) (M_w = 4330 g/mol) was purchased from Bachem. The starting aggregation states and the structure of the peptide are highly dependent on the sample batch [73]. Therefore to achieve disaggregation and a unique conformational state, the peptide was first dissolved in hexafluoro-2-propanol (to disrupt intermolecular H-bonds) at an approximate 1:1 ratio (mg:ml), followed by sonication until the peptide dissolved completely. Complete solubilization is indicated by the absence of precipitate after centrifugation. The organic solvent was removed with nitrogen gas and under vacuum. The dry peptide, in a monomeric, unstructured state, was dissolved in aqueous buffer solutions. A solution prepared in hexafluoro-2-propanol is stable for several months with no precipitation observed.

Desired pH was obtained with 10 mM potassium phosphate buffer or 10 mM hepes buffer (pH 7.4) and 10 mM ammonium acetate buffer (pH 4). Sodium azide (0.05 mM) was added to prevent microbial growth. The pH values were measured with a pH meter (WTW-inoLab Level 1) equipped with an electrode (model SenTix Mic, WTW) that was calibrated with pH 4.00, 7.00 and 12.00 buffers.

3.2 Absorption Spectroscopy

The concentration of peptides was estimated from UV absorbance (A) at around 280 nm and 230 nm according to the Lambert-Beer law,

$$A(\lambda) = \log_{10}\left(\frac{I_0}{I}\right) = \varepsilon(\lambda)Cl, \tag{3.1}$$

where I_0 is the intensity of the incident light, I is the intensity of the light after traveling a distance l (cm) through a medium containing a sample with a concentration C (M) and ε is the molar extinction coefficient (M^{-1} cm^{-1}) of the sample.

At around 280 nm the optical absorption is due to the aromatic amino acid residues tryptophan or tyrosine. No other residues make an appreciable contribution at this wavelength. In the case of amyloid β-peptide (1–40) a maximum absorption in the aromatic region is observed at 276 nm which results from the optical contribution of the tyrosine residue (ε = 1390 M^{-1} cm^{-1}).

Higher sensitivity in absorption measurement is obtained at 230 nm. In this range the molar extinction of each residue is about 300 M^{-1} cm^{-1}. However, many solvents also absorb at this wavelength complicating the measurements. Since B18 has no aromatic groups, the concentration of the peptide was estimated from UV absorbance at 230 nm.

Absorption spectra were recorded with a Cary 400 UV/Vis spectrophotometer in quartz cuvettes with an optical path length of 0.1 cm or 0.2 cm from 190 to 400 nm.

3.3 Circular Dichroism Spectroscopy

The secondary structure of peptides and proteins can be determined by circular dichroism spectroscopy in the far-UV spectral region. The technique is nondestructive, requires small amount of material and can be used for molecules in solution.

Circular dichroism is a chiroptical phenomenon by which optically active molecules such as proteins interact differently with left and right circularly polarized light. To exhibit such differences a molecule must be chiral, i.e., asymmetric in the sense that it cannot be superimposed on its mirror image.

Circularly polarized light has an electric field vector of constant magnitude that changes its direction as a function of time on the plane orthogonal to the propagation. It is called right circularly polarized light if the tip of the electric field vector defines a right-handed helix (Figure 3.1). The left circularly polarized light has the electric vector rotating in the opposite direction.

In contrast, the electric vector of linearly polarized light has varying magnitude and constant direction orthogonal to the line of propagation. Linearly polarized light can be decomposed in right and left circularly polarized light of equal magnitudes (Figure 3.2 a).

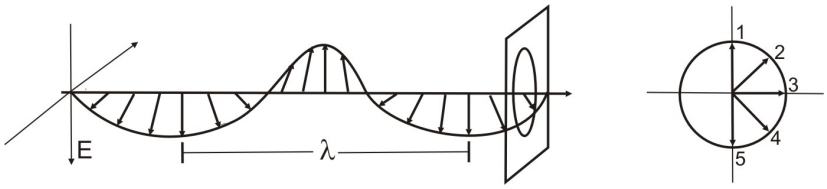

Figure 3.1. Schematic diagram showing the electric vector of right circularly polarized light. The tip of the electric vector follows a circular path in a clockwise sense when viewed along the direction of propagation, looking toward the light source.

Circular dichroism is defined as the difference between the absorption of right and left circularly polarized light. Applying the Lambert-Beer law, equation (3.1), circular dichroism is described as:

$$\Delta A = A_L - A_R = \varepsilon_L Cl - \varepsilon_R Cl = \Delta\varepsilon Cl, \tag{3.2}$$

where $\Delta\varepsilon$ represents the difference of the decadic molar extinction coefficient of the molecules for right and left polarized light. When linearly polarized light passes through an optically active molecule, its two circular components are differently absorbed by the molecule and the light is converted into elliptically polarized light, in which the tip of the electric vector traces out an ellipse rather than oscillating in a plane or forming a circle (Figure 3.2).

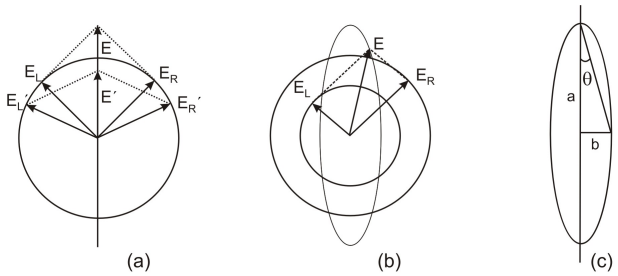

Figure 3.2. (a) Linearly polarized light resolved into two circular components with the same intensity. (b) Elliptically polarized light generated by right (E_R) and left polarized light (E_L) of different intensities. (c) The ellipticity is the angle θ whose tangent is the ratio of the semi minor *a* and semi major *b* axes of the ellipse.

Circular dichroism data is plotted as ellipticity, which is an angle θ, whose tangent is the ratio of the semi minor and semi major axes of the ellipse (Figure 3.2 (c)). Since θ is always small, the tangent of θ will be equal to θ in radians

$$\theta(rad) \approx tan\theta = \frac{|E_L| - |E_R|}{|E_L| + |E_R|}. \tag{3.3}$$

Since the light intensity is proportional to the square of its electric field vector, applying the definition of absorbance, equation (3.3) becomes

$$\theta(rad) = \frac{10^{-A_L/2} - 10^{-A_R/2}}{10^{-A_L/2} + 10^{-A_R/2}}. \tag{3.4}$$

Considering $10^x = \exp(x \ln 10)$, expanding the exponentials ($\exp(x) \approx 1 + x/(1!)$, for small x), neglecting terms of the order of ΔA in comparison with unity, and converting to degrees gives

$$\theta(deg) = 180 \ln 10 \frac{\Delta A}{4\pi} = 32.98 \Delta A. \tag{3.5}$$

The ellipticity of the light that emerges from an optically active sample is very small and would be difficult to measure accurately. Therefore modern instruments measure circular dichroism by exposing a sample alternately to left and right circularly polarized light and detect the differential absorption ΔA.

To compare results it is necessary to remove the linear dependence on path length and solute concentration defining the molar ellipticity $[\theta]$ (deg cm^2 dmol^{-1})

$$[\theta] = 100 \frac{\theta}{Cl}. \tag{3.6}$$

For peptides and proteins, circular dichroism data in the far UV is reported in terms of mean residue concentration. In this case C is obtained by dividing the molecular mass of the macromolecule by the number of residues. Combining equations (3.2), (3.5) and (3.6) yields the relation between $[\theta]$ and $\Delta\varepsilon$

$$[\theta] = 3298 \Delta\varepsilon. \tag{3.7}$$

Circular dichroism spectra were recorded with a Jasco 720 spectrophotometer from 190 to 260 nm using quartz cuvettes with an optical path length of 0.05 cm or 0.1 cm.

3.3.1 Electronic Circular Dichroism of Proteins

The major chromophore in peptides and proteins is the amide group that results from bonding between component amino acids [74]. The amide group has three π centers and therefore three π orbitals with two main $\pi\pi^*$ transitions; one near 190 nm and the other at higher energy. The $\pi\pi^*$ is electrically allowed and the transition moment is directed approximately along the NO direction (Figure 3.3). In addition to the π orbitals, there are two lone pairs on the carbonyl oxygen (n orbital) which provides an nπ^* transition. This transition is electrically forbidden in amides but has a magnetic dipole transition moment directed along the carbonyl bond at a wavelength between 215 to 220 nm, depending on the solvent (Figure 3.3).

Proteins and peptides have a characteristic circular dichroism spectrum according to their secondary structure. An example is shown in Figure 3.4 for poly-L-lysine which

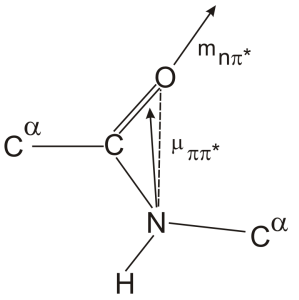

Figure 3.3. The electric dipole transition moment of the amide $\pi\pi^*$ transition ($\mu_{\pi\pi^*}$) and the magnetic dipole transition moment of the amide nπ^* transition ($m_{n\pi^*}$).

can adopt α-helix, β-sheet or random coil conformation in aqueous solution. At pH 4.5, poly-L-lysine exists as disordered polypeptide due to the interaction among charged side groups. On deprotonation at pH 12, internal hydrogen bonds are favored to increase the stability and the homopeptide folds as a helix. Upon heating at pH 12, the energy necessary to break the hydrogen bonds stabilizing the helical structure is supplied. Lysyl residues of the random chain are removed from the aqueous environment and are associated, forming the β-sheet structure.

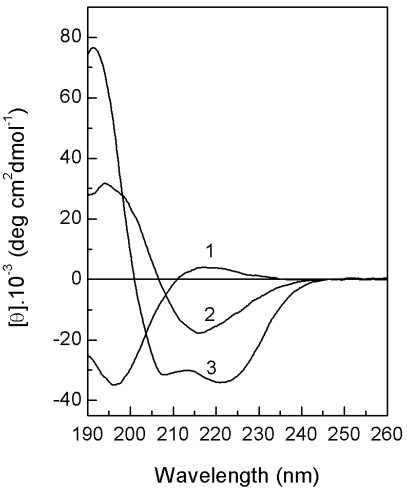

Figure 3.4. Circular dichroism spectra of poly-L-lysine in random coil (1), β-sheet (2) and α-helix (3) conformation.

The spectrum of α-helix shows a negative band at about 222 nm that has been attributed to the nπ^* transition, and negative and positive bands near 208 and 190 nm, respectively, assigned to the $\pi\pi^*$ transition. These two bands result from exciton splitting of the $\pi\pi^*$

absorption band into a 208 nm component polarized along the helix axis and a 190 nm component polarized perpendicular to the helix axis due to the helix symmetry [74].

The spectrum of β-sheet has a negative band near 215 nm, assigned to the nπ^* transition, and a positive band near 197 nm ($\pm$ 5 nm), attributed to $\pi\pi^*$ transition. The degree of twisting of the β-sheet is related to the magnitude of the bands. Weakly twisted sheets have bands of equal magnitude whereas for highly twisted sheets the $\pi\pi^*$ band near 197 nm is much stronger than the nπ^* band [74].

Unordered polypeptide chains generally show a strong negative band just below 200 nm ($\pi\pi^*$ transition) and a very weak band at 217 nm (nπ^* transition), which can be either a positive band or a negative shoulder.

There are two major types of β-turns. Type I β-turns exhibit a circular dichroism spectrum similar to the α-helix in the long wavelength region, but the positive band at short wavelength is weaker. Type II β-turns spectrum is similar to the β-sheet, but shifted to the red by 5 to 10 nm [74].

3.3.2 Protein Secondary Structure Estimation

Estimation of the secondary structure of a protein from its circular dichroism spectrum is complicated by the fact that aromatic amino acid side chains and disulfide bonds can contribute to the spectrum. Additionally the characteristic of the spectrum depends on the length of structural elements in peptides and proteins (Figure 3.5). This is particularly important for the α-helix structure for lengths below 1000 units because of the short average helix length in globular proteins.

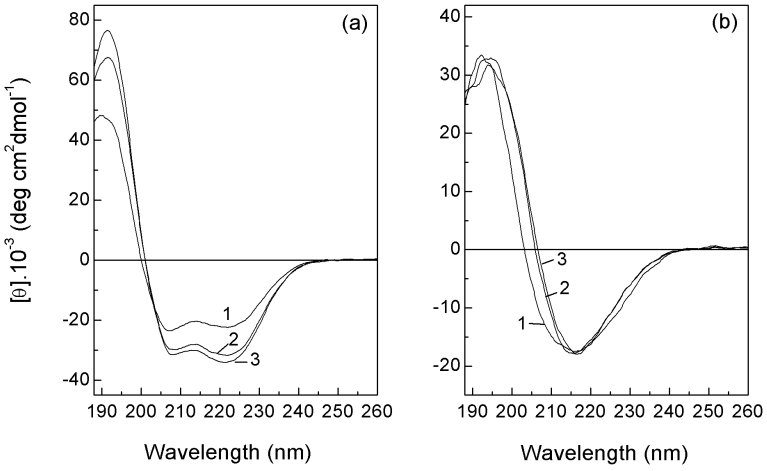

Figure 3.5. Circular dichroism spectra of poly-L-lysine with different degree of polymerization in α-helix (a) and β-sheet (b) conformation: 126 (curve 1), 1027 (curve 2) and 2714 (curve 3).

The helix content can be estimated using the helix-coil model which accounts for the number of amino acid residues [75]. According to this model, the ellipticity at 222 nm, θ_{obs}, is assumed to be linearly related to the mean helical content, f_H,

$$\theta_{obs} = f_H[\theta_H(1-x/N_r) - \theta_C] + \theta_C, \tag{3.8}$$

where θ_H is the ellipticity of a complete helix of infinite length at 0 °C (-42.500 deg cm^2 dmol^{-1}), θ_C is the ellipticity of the random coil at 0 °C (640 deg cm^2 dmol^{-1}). The term $(1-x/N_r)$ is a correction to θ_H for end effects, where x is the number of peptide CO groups that are not hydrogen bonded in a complete helix (for unblocked peptides, $x = 4$, and for carboxyamidated peptides, $x = 3$) and N_r is the number of peptide residues. Measurements at a single wavelength are useful to follow the kinetics and thermodynamics of the folding process. The disadvantages are that the model is limited and information on β-sheets and β-turns is not included.

There are many methods to obtain structural information from circular dichroism data in the literature [76]. Basically, all methods assume that the spectrum of a protein can be represented by a linear combination of the secondary structure elements, plus a noise term, which includes the contribution of aromatic chromophores,

$$\theta_\lambda = \sum_{i=1}^{N} F_i B_{\lambda i} + noise, \tag{3.9}$$

where θ_λ is the circular dichroism data of the protein as a function of wavelength λ, F_i is the fraction of each structure i, and $B_{\lambda i}$ is the ellipticity of the secondary elements at each wavelength λ. The basis spectra $B_{\lambda i}$ are calculated from circular dichroism data of a set of reference proteins of known three-dimensional structure (usually from X-ray analysis). The constraints for F_i are

$$\sum_{i=1}^{N} F_i = 1 \qquad \text{and} \qquad F_i \geq 0.$$

The deconvolution of spectra of amyloid peptides is difficult due to their tendency to aggregate. At the early stages of the β-sheet transition small peptide fibers can scatter light and distort circular dichroism spectra. Finally at the end of the transition the signal simply disappears. Thus deconvolution of the curves using standards can give poor fits.

The methods that fit the data to be analyzed via the spectra of standards by least squares (multiple linear regression) give reliable results. Two programs, Lincomb and G&F, that perform constrained least square analysis (sum of F_i equal to 1) can be used. These programs are useful for deconvolution of peptide spectra since polypeptide standards such as poly-L-lysine curves (G&F program) [77] or standard curves from Brahms and Brahms (Lincomb) [78] can be included in the reference set.

Another method that gives reliable results is based on the ridge regression analysis (CONTIN) [79]. The method involves the direct analysis of a circular dichroism spectrum as a linear combination of the spectra of a large database of proteins with known

conformations. In this method the contribution of each reference is kept small, unless it contributes to a good agreement between the theoretical best-fit curve and the raw data. Sreerama and Woody modified the method by incorporating the variable selection method in the locally linearized model in CONTIN (CONTIN/LL) [80]. This method gave the most reliable results. The analysis of the circular dichroism spectra was carried out using the CDPro software [80]. Due to the disordered structure of the peptides studied in aqueous solutions, an extended reference set of 48 peptides was used, which included various spectra of denatured/disordered systems (basis set 7 in CDPro) [81].

3.4 Neutron and X-Ray Reflectometry

Neutron and X-ray reflectometry techniques are used for investigating the structures of surfaces and interfaces.

3.4.1 Theory of Specular Reflection

Neutrons and X-rays are reflected and transmitted at the interface between two media with different optical properties [82]. The properties of a medium are described by a refractive index n which for neutrons and X-rays is defined as

$$n = 1 - (\delta - i\beta). \tag{3.10}$$

The dispersion term δ is defined as

$$\delta = \frac{\lambda^2}{2\pi}\rho_n \qquad \text{for neutrons,}$$

$$\delta = \frac{\lambda^2}{2\pi}r_e\rho_e \qquad \text{for X-rays,}$$

where

$$\rho_n = \sum N_j b_j,$$

is the neutron scattering length density, N_j is the number density of atomic species j, b_j is the scattering length of the material, r_e is the classical electron radius (2.814 x 10^{-5} Å), ρ_e is the electron density of the material and λ is the wavelength of the incident radiation.

The absorption term β is defined as

$$\beta = \frac{\lambda}{4\pi}\mu,$$

where μ is the neutron or X-ray linear absorption coefficient.

Typical values for δ are 10^{-5} to 10^{-6} and the absorption β is one or two orders of magnitude smaller for X-rays and approximately 10^{-12} for neutrons which is essentially

negligible. The absorption term β can also be neglected for X-rays in the case of soft matter.

In a reflectivity experiment, radiation with wave vector K_i is incident on the interface between two media with different refractive indices at an angle θ. In general some of the radiation will be reflected with wave vector K_r and some transmitted. In the case of specular reflection the angle of incidence is equal to the angle of reflection, the wave vectors K_i and K_r are confined to the xz plane and are equal in magnitude, and the scattering vector q is defined as

$$q = |K_i - K_r| = \frac{4\pi}{\lambda} \sin\theta. \tag{3.11}$$

The transmission and reflection coefficients depend upon the height (scattering length density or electron density) and thickness of the barrier and the momentum of the incident radiation (photons or neutrons). The scattering geometry is illustrated schematically in Figure 3.6.

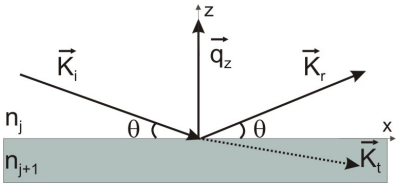

Figure 3.6. Scattering geometry of the specular reflection experiment.

Since the refractive index is slightly less than 1, this implies that a beam impinging on a flat surface can be totally reflected. The condition to observe total reflection is that the angle of incidence θ must be smaller than a critical angle θ_c. Applying the Snell-Descartes' law

$$\cos\theta = n\cos\theta_{tr}, \tag{3.12}$$

where θ_{tr} is the angle between the transmitted ray and the surface, and with $\cos\theta_{tr} = 1$ at total reflection, yields in absence of absorption

$$\cos\theta_c = n = 1 - \delta. \tag{3.13}$$

Since δ is of the order of 10^{-5} to 10^{-6}, the critical angle for total external reflection is extremely small. At small angles $\cos\theta_c$ can be approximated as $1 - \theta_c^2/2$ and (3.13) becomes

$$\theta_c^2 = 2\delta \tag{3.14}$$

The total external reflection of a X-ray or neutron beam is therefore only observed at grazing angles of incidence $\theta < 0.5^\circ$. At larger angles the reflectivity decreases very rapidly.

The essence of a specular reflectivity experiment is to measure the reflectivity R of a surface as a function of the incident angle θ or alternatively as a function of the modulus of the wave-vector transfer q [82]. The reflectivity is defined as

$$R = \frac{I}{I_0}, \tag{3.15}$$

where I is the intensity of the reflected radiation for an angle of incidence θ or wave vector transfer q and I_0 is the intensity of the incident radiation. Normalizing the intensity of the incident beam to unity, the reflectivity is given by

$$R = \left|r^2\right|, \tag{3.16}$$

which corresponds to the reflectivity of an ideally smooth, sharp interface known as the Fresnel reflectivity. The reflected intensity is the quantity measured in an experiment and is defined as the square of the modulus of the reflection coefficient, r, given by the Fresnel equation

$$r = \frac{\sin\theta - n\sin\theta_{tr}}{\sin\theta + n\sin\theta_{tr}}. \tag{3.17}$$

Applying the Snell-Descartes' law, equation (3.12), and considering equation (3.13) the reflection coefficient for small incidence angles is

$$r = \frac{\theta - \sqrt{\theta^2 - \theta_c^2}}{\theta + \sqrt{\theta^2 - \theta_c^2}}. \tag{3.18}$$

Below the critical angle the reflectivity is unity (incident radiation is completely reflected by the interface). When $\theta \geq 3\theta_c$ the reflectivity decreases proportional to q^{-4}.

The Fresnel reflectivity is applied to single uniform substrates with a constant electron density. In the case of stratified media or multilayers scattering from all interfaces has to be considered. Considering that the material is made of an infinite number of thin layers, the reflectivity is given by

$$R(q_z) = R_F(q_z)\left|\frac{1}{\rho_s}\int_{-\infty}^{+\infty}\frac{d\rho(z)}{dz}\exp(iq_z z)dz\right|^2, \tag{3.19}$$

where z is the vertical distance from the substrate surface, ρ_s is the electron density or scattering length density of the substrate, $d\rho/dz$ is the gradient of the density along the surface.

When a layer of another material is deposited onto the interface, the reflectivity profile becomes an oscillating function with a period of oscillations known as Kiessig fringes (Figure 3.7). The fringe spacing is related to the layer thickness, while the depth of the oscillations is dependent on the magnitude of the differences in scattering length density or electron density between the interfaces.

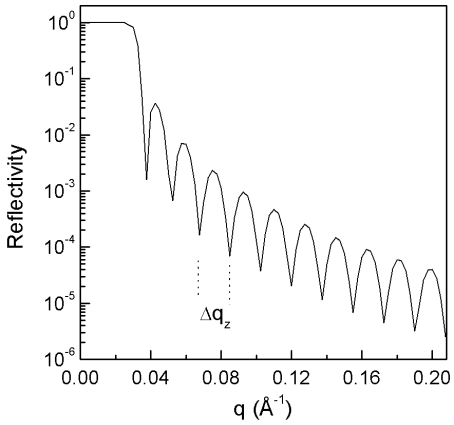

Figure 3.7. Calculated X-ray reflectivity of a polymer film with a thickness of 350 Å on silicon substrate.

Roughness of surfaces and interfaces can significantly alter the reflected intensity [82]. The reflectivity of sharp interfaces is calculated assuming a constant index of refraction n_j that jumps to another constant value n_{j+1} at the interface between layer j and $j+1$. For a rough surface or interface this sharp step has to be replaced by a continuous variation of the refractive index and hence by a continuous electron density or scattering length density (Figure 3.8).

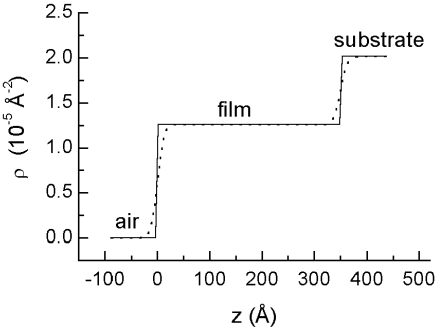

Figure 3.8. Calculated density profile (ρ) of a polymer film on a substrate. The solid line represents the density profile of ideally smooth air/polymer and polymer/substrate interfaces. The dashed line corresponds to the density profile of polymer and substrate surfaces with identical roughness (10 Å).

The reflectivity curve of a rough interface falls more rapidly than in the case of sharp interfaces and the amplitude of the fringes can be reduced at high wave-vector transfers.

An example of reflectivity curves of a film deposited on silicon substrate assuming a certain roughness for the substrate and film surface is shown in Figure 3.9. The amplitude remains unaffected only if the roughnesses of the substrate and film surfaces are identical, but the intensity drops more quickly than in the case of sharp interfaces.

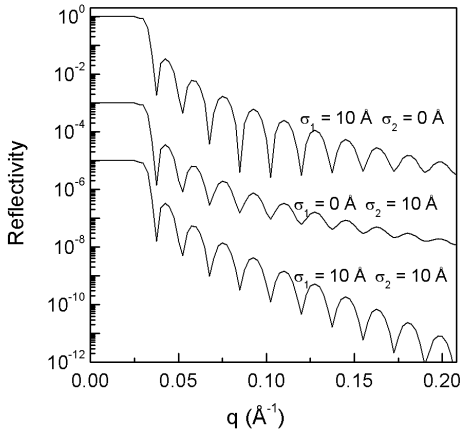

Figure 3.9. Calculated X-ray reflectivities of a polymer film with a thickness of 350 Å on silicon and different root mean square roughness σ_1 (air/polymer interface) and σ_2 (polymer/silicon interface). The curves are shifted on the intensity scale for clarity.

A rough interface can be seen as made of locally flat areas with different heights. The reflection coefficient of a rough surface is obtained by multiplying the Fresnel reflection coefficient by a factor known as the Croce-Névot factor

$$r_{j,j+1}^{rough} = r_{j,j+1}^{flat} \exp(-q_{z,j} q_{z,j+1} \sigma_{j+1}^2/2), \tag{3.20}$$

where the parameter σ (root mean square height) is the standard deviation of the interface position in the z direction for all x, y positions and gives an indication of the degree of roughness. Therefore it is possible to determine the interface roughness of a layer system by reflectivity.

3.4.2 Data Analysis

The observation of Kiessig fringes in a reflectivity profile can allow direct determination of the layer thickness d from the Δq spacing of the minima of two neighboring interference fringes

$$d = \frac{2\pi}{\Delta q}. \tag{3.21}$$

Further information can be obtained by more complex data analysis methods. The reflectivity spectra were analyzed by applying the standard fitting routine Parratt 32 [83].

The calculation is based on Parratt's recursion scheme for stratified media. The film was modeled as consisting of layers of specific thickness and scattering length density or electron density. The model reflectivity profile calculated using the dynamic iterative model was compared to the measured one. Then the model was adjusted to the best chi-square, a residual term indicating the deviation between the measured and calculated data. The thickness, density profile and the roughness of each layer were obtained from the fits.

3.4.3 Reflectometers

X-ray reflectometry measurements were performed with a θ (reflection angle)/2θ (detector angle) instrument with U = 30 kV, I = 15 mA, $\lambda = 1.54$ Å (Cu K_α radiation). The divergence of the incoming beam was 0.1° and the 2θ resolution was 0.05°.

Neutron reflectometry measurements were performed at the Hahn-Meitner Institute, Berlin, on the V6 reflectometer with a $\theta/2\theta$ geometry. The neutron wavelength selected was 4.66 Å. The resolution was set to $\Delta q = 0.001$ Å^{-1} for $q \leq 0.04$ Å^{-1}, and $\Delta q = 0.002$ Å^{-1} for larger q values. The experiments were performed in a solid/liquid experimental cell, which consisted of a single silicon crystal with size of 15 x 80 x 50 mm^3 and a teflon trough that was fixed to the bottom of the silicon crystal (Figure 3.10). Because of the large penetration depth of the neutrons as a consequence of their weak interaction with almost any material, *in situ* measurements at solid/liquid interfaces can be performed.

Figure 3.10. Typical cell used for neutron reflectivity measurements at the solid/liquid interface.

3.5 Atomic Force Microscopy

Atomic force microscopy (AFM) is a scanning probe microscopy technique for studying the topology of surfaces with nanometer precision. A very sharp tip at the end of a cantilever is used to probe and map the morphology of a surface. AFM detects the interaction force between tip and sample on the basis of the cantilever deflection. The bending of the cantilever is usually detected by an optical technique by directing a laser beam onto the cantilever. The beam is reflected from the surface on the back side of the cantilever onto a photodetector. The scanning system that moves the sample or scans the probe over the sample is typically a piezoelectric tube scanner.

AFM imaging can be processed essentially by two modes.

In contact mode the tip is brought in contact with the sample. The cantilever deflection is kept constant, while the tip scans laterally over the sample surface. If the cantilever deflection changes, a feedback system moves the piezoscanner in the vertical direction to maintain the deflection constant (*setpoint*). The piezo movements ΔZ are then recorded as a function of x and y position. The resulting image is called height image and ideally corresponds to the sample surface topography.

In tapping mode, also referred to as intermittent contact mode, the cantilever oscillates close to its resonance frequency, typically between 100–400 kHz and with a free amplitude between 10–150 nm. When the sample surface approaches the tip, the cantilever oscillations are, at some point, attenuated due to interactions between the tip and the sample. The amplitude drop is used as feedback parameter. In this mode the tip is only for a short time in contact with the sample and hence the lateral forces are drastically reduced. It is therefore preferred when dealing with soft substrates.

AFM imaging was performed in air in tapping mode with a Nanoscope III Multi-mode. At least three regions of the surface were examined to verify if similar morphology existed throughout the sample. The images were analyzed using the Nanoscope III software. Height sizes were estimated by section analysis and the root mean square roughness was calculated as

$$\sigma = \sqrt{\frac{\sum (Z_i - \overline{Z})^2}{N}}, \tag{3.22}$$

where Z_i is the height value for the i-th pixel on the AFM image, $\overline{Z}$ is the average on Z_i and N is the number of points in the selected area.

4 Adsorption of Self-Assembled Peptides on Modified Surfaces

Several proteins are located at a phase boundary. Moreover many biological processes occur at or near interfaces, including cell-cell adhesion, protein synthesis and secretion, transport and translocation of proteins across membranes. During these processes, strong surface interactions may induce the unfolding of polypeptide chains and damage the native structure of a protein.

Fusion peptides promote the fusion of membranes and therefore are functional at interfaces. Surface interactions may be responsible for peptide conformational changes, which will determine their function. These interactions may as well induce aggregation of fusion peptides into amyloid fibrils. In fact several fusion peptides such as B18 peptide are found to form fibrils at lipid membranes [8, 44].

Likewise the fibrillogenesis of amyloidogenic peptides such as prion protein fragments and amyloid β-peptide might result from surface interactions. The cellular prion protein is a glycoprotein bound to the cell surface by a glycolipid anchor [84] and its aberrant isoform is thought to result from the cellular form either at the cell surface [85] or along the endocytic pathway [86].

The amyloid β-peptide is a sequence of a transmembranar protein with an extracellular and a transmembranar domain and results from the proteolytic cleavage of the parent protein [54], as described in section 2.3.2. The precise manner in which soluble peptide undergoes conformational changes and deposition *in vivo* is not known. It became clear that oligomerization and fibrillogenesis start when the peptide concentration exceeds a critical level. The increase of the local peptide concentration may well result from peptide-surface association. A significant amount of soluble peptide was found to bind to various macromolecules such as lipoproteins and albumin in human plasma and cerebrospinal fluid [87, 88]. Apolipoprotein E (cholesterol transport protein) and derived proteolytic fragments are present in the amyloid deposits of Alzheimer's disease [89]. In fact the apolipoprotein E gene is associated with altered risks of the disease [4]. In addition the peptide is described to specifically bind to membranes containing gangliosides (glycolipids that constitute 5–10% of the total lipid mass of neuronal membranes), forming an antiparallel β-sheet structure [90], and was found tightly bound to GM1 ganglioside in brains exhibiting early pathological changes of Alzheimer's disease [91]. Kowalewski and

Holtzman have found that the size and the shape of the peptide aggregates, as well as the kinetics of their formation, exhibited a pronounced dependence on the physicochemical nature of the surface [92]. On hydrophilic mica, amyloid β-peptide formed pseudo micellar aggregates, whereas on hydrophobic graphite the peptide formed uniform, elongated sheets. Furthermore, the formation of β-sheets by amyloid peptide has been described at the air-water interface, in contrast to the initial bulk solution rich in α-helix and unordered conformations [93, 94]. Such evidences suggest that surfaces may be crucial for fibril formation of amyloid peptides. The degree of adsorption on surfaces might be directly related to the peptide aggregation, since it will influence the local peptide concentration. The structural changes of amyloid β-peptide induced by teflon particles were previously reported to depend on the amount of adsorbed molecules [95]. Therefore, the investigation of the influence of different surfaces on peptide adsorption may provide insights for the mechanism of fibril formation.

The degree of adsorption of B18 and amyloid β-peptide on modified surfaces was determined by X-ray and neutron reflectometry. These techniques are extremely sensitive to the thickness and electron or scattering length densities of self-assembled peptide layers. However, they cannot provide information about lateral features, since they effectively average over the structure in the surface plane. Therefore atomic force microscopy was combined with the reflectivity techniques in order to characterize the morphology of adsorbed peptide.

4.1 Surface Preparation

Hydrophilic and hydrophobic surfaces were prepared on silicon substrates previously cleaned by the RCA standard procedure, which consists in immersing the substrates in a solution of H_2O + H_2O_2 (30%) + NH_3 (30%), ratio 5:1:1 by volume, and heated to 75 °C for 10 minutes, followed by excessive rinsing with ultrapure water, in order to remove organic residues.

4.1.1 Hydrophilic Surfaces

Hydrophilic surfaces consisted of oxide layer, polyelectrolyte multilayers and a polyvinyl formal polymer (formvar).

Silicon oxide surface

The polished surfaces of silicon substrates bear a native oxide layer. The oxide layer surface consists of siloxane bonds (Si-O-Si), which rapidly acquire silanol groups (Si-OH) at the surface from contact with water or atmospheric moisture. These -OH groups make the surface hydrophilic. After the RCA procedure the silicon oxide surface is well

saturated with silanol groups, conferring very high hydrophilicity. Above pH 2, the oxide surface is negatively charged and the charge density is almost constant over pH 3–8 [96].

Polyelectrolyte multilayers

Polyelectrolyte multilayer films were prepared by the layer-by-layer self-assembly technique, which involves the sequential adsorption of oppositely charged polyelectrolytes onto a solid support [97]. The resulting multilayers are primarily formed by electrostatic interaction and complex formation between the oppositely charged polyelectrolytes.

The polymers were adsorbed from aqueous solutions of 10^{-2} monomer mol/L. The silicon substrate was initially immersed in a solution of poly(ethyleneimine) (PEI, M_w = 750000 g/mol) for 20 minutes, and then washed in ultrapure water at least three times to remove the excess polymer. After this procedure the substrate was positively charged and was used for the deposition of the polyanion poly(sodium 4-styrenesulfonate) (PSS, M_w = 70000 g/mol) followed by the polycation poly(allylamine hydrochloride) (PAH, M_w = 50000–65000 g/mol), both solutions contained 1 M NaCl. The adsorption steps were carried out by immersing the substrates in the polymer solution for 20 minutes and rinsed with water until obtaining the desired number of layers. After deposition of the last layer the sample was dried in a nitrogen stream.

The chemical structures of the polyelectrolytes used in the preparation of charged hydrophilic films are shown in Figure 4.1.

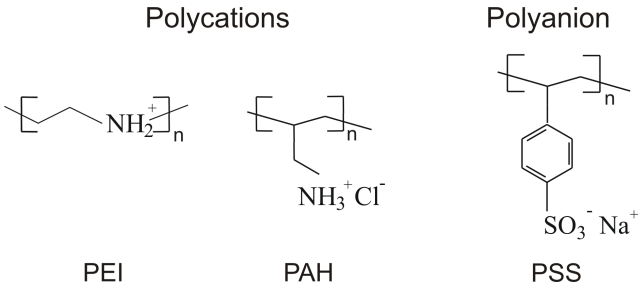

Figure 4.1. Chemical structures of the assembled polyelectrolytes.

The pK values for PAH were estimated to be in the range between 9 and 10 and between 3.5 and 4.5 for PSS [98]. Zeta potential values for the polyelectrolytes on flat fused silica were determined to be -20 mV for the anionic outer layer and $+20$ mV for the cationic one, after the deposition of three to four layers [99].

The advantages of using polyelectrolytes as hydrophilic surfaces are their high charge density and the fact that it is possible to control the film thickness.

Formvar

A non-charged film was prepared with formvar 15/95E (Mr = 24000–40000 g/mol), a commercial polyvinyl formal polymer, containing 5 to 6% hydroxyl groups in the form of polyvinyl alcohol (Figure 4.2).

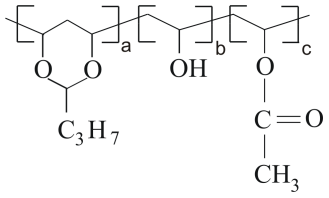

Figure 4.2. Chemical structure of the polymer formvar.

Formvar was dissolved in chloroform at a concentration of 1 g per 100 mL. The pre-cleaned silicon substrate was immersed in the solution and removed with a constant speed of 0.5 mm/s.

4.1.2 Hydrophobic Surfaces

Hydrophobic surfaces were obtained by coating silicon substrates with octadecyltrichlorosilane, a polysiloxane-surfactant complex and polystyrene.

Octadecyltrichlorosilane

Silanization of silicon substrates was attained with n-octadecyltrichlorosilane (OTS) dissolved in toluene at a concentration of 2.5 x 10^{-3} mol/L. The pre-cleaned substrates were first dried with nitrogen gas, as well as the surrounding atmosphere to eliminate the water. The substrates were then immersed in the solution overnight at a temperature of 4 °C. The excess of OTS was removed by washing the substrates with toluene and isopropanol alternately several times. OTS has the chemical formula $CH_3(CH_2)_{17}SiCl_3$ and a molecular weight of 387.94 g/mol.

Polysiloxane-surfactant complex

The polysiloxane contained an amount of 0.6 mol% aminoethyl aminopropyl functions. The complex was obtained as follows. One equivalent of silicone oil was dissolved in 100 ml hexane and 0.5 equivalent of dodecanoic acid was dissolved in 50 ml butan-2-ol and 0.5 ml methanol. While stirring, the surfactant solution was added in drops to the silicon oil resulting in a transparent complex solution. The chemical structure of the polysiloxane-surfactant complex is shown in Figure 4.3. Silicon substrates were coated

with 1 mg/mL complex solution by spin coating using a SCS model 6708D spin-coater, at a speed of 3500 rpm, for 60 seconds.

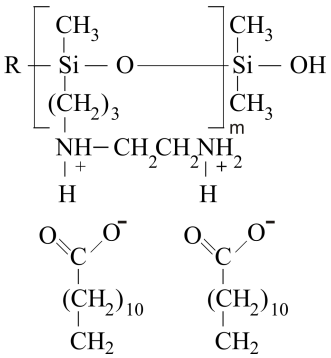

Figure 4.3. Chemical structure of the polysiloxane-surfactant complex.

Polystyrene

A solution of polystyrene was prepared at a concentration of 0.1% (w/w) in toluene. The coating of the silicon substrates was performed by spin coating using a SCS model 6708D spin-coater, at a speed of 3550 rpm, for 60 seconds. Polystyrene has the chemical formula $[CH_2CH(C_6H_5)]_n$ and the molecular weight was 62500 g/mol.

4.2 Characterization of B18 Peptide Adsorption

B18 peptide was allowed to adsorb on hydrophilic charged films and trichlorosilane layer at different incubation times. The solution concentration was 4.8 μM and the pH 7.4. The peptide was in random coil conformation, as determined by circular dichroism spectroscopy.

4.2.1 Degree of Adsorption at Hydrophilic Interfaces

The adsorption of B18 peptide on charged PEI(PSS/PAH)$_6$ and PEI(PSS/PAH)$_6$PSS films was characterized by neutron reflectometry. The reflectivity profile of the pure films in D_2O was first measured. The subphase was then exchanged by the peptide solution. After 12 hours adsorption time the peptide solution was exchanged by pure D_2O and neutron reflectivity measurements were repeated.

Figure 4.4 shows the neutron profile of the positively charged PEI(PSS/PAH)$_6$ film before (curve 1) and after exposure to B18 peptide solution (curve 2). No differences in the position and amplitude of the Kiessig fringes were observed in the reflectivity curves, in-

dicating that the thickness and composition of the film were unchanged. Hence adsorption and penetration of B18 on the positively charged film can be excluded.

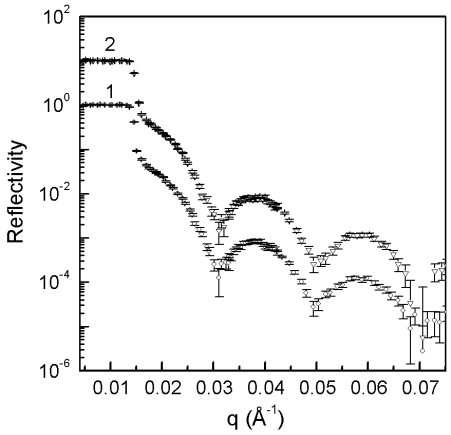

Figure 4.4. Neutron reflectivity profile of positively charged PEI(PSS/PAH)$_6$ film in D_2O: 1) bare polymer surface, 2) polymer surface exposed to B18 peptide for 12 h. The curves are offset vertically for clarity.

The effect of B18 peptide on the negatively charged PEI(PSS/PAH)$_6$PSS film can be seen by comparing the reflectivity profile of the bare surface (Figure 4.5, curve 1) with that from the film after exposure to the peptide solution (Figure 4.5, curve 2). B18 exposure resulted in a shift of the position of the minima to smaller q values, indicating an increase in the film thickness.

The structural parameters of the pure PEI(PSS/PAH)$_6$PSS film were obtained by fitting a two-layer model to the reflectivity profile, the first layer representing the silicon oxide and the second layer the film. The thickness and the scattering length density of the polymeric film were estimated to be 358 Å and 3.79 x 10^{-6} Å^{-2}, respectively. Adsorbed B18 could not be accounted for by a single uniform layer. Thus the reflectivity profile of the polymeric film after B18 adsorption was fitted with a two-layer model but in this case the second layer corresponds to the film plus adsorbed B18 peptide. A thickness of 369 Å was obtained. Therefore B18 adsorption resulted in a thickness increase of 11 Å. The fitting parameters are resumed in Table 4.1.

On a hydrophilic surface, the electrostatic attraction is often the driving force for adsorption of a protein on the solid substrate [100]. The extent of adsorption is determined by the balance between electrostatic attraction and repulsion in the adsorbed layer. At pH 7.4, B18 peptide carries a net positive charge. Most likely, the absence of B18 adsorption on the positively charged film is due to electrostatic repulsion between the peptide and the surface, whereas adsorption on the negatively charged film is driven by electrostatic

layer	d(Å)	ρ (10^{-6}Å^{-2})	σ(Å)
silicon oxide	8 ± 2	3.41 ± 0.10	5 ± 1
before adsorption			
film	358 ± 1	3.79 ± 0.10	9 ± 3
D_2O	–	6.11 ± 0.20	23 ± 4
after adsorption			
film and peptide	369 ± 1	3.79 ± 0.10	2 ± 1
D_2O		6.11 ± 0.20	25 ± 1

Table 4.1. Structural parameters used to fit the reflectivity profiles measured for the system PEI(PSS/PAH)$_6$PSS and B18 peptide. d, ρ and σ are the thickness, scattering length density and roughness, respectively.

attraction between the film and the positively charged B18. The adsorbed amount on the negatively charged polymer corresponds to an irreversibly adsorbed state since the surface was rinsed with D_2O after B18 exposure.

4.2.2 Morphology of Adsorbed B18 on Charged Layers

Negatively charged surfaces were incubated in B18 peptide solution and removed at defined times for atomic force microscopy measurements. After removal the surfaces were washed with ultrapure water and dried with nitrogen.

Atomic force microscopy imaging of PEI(PSS/PAH)$_6$PSS after B18 peptide adsorp-

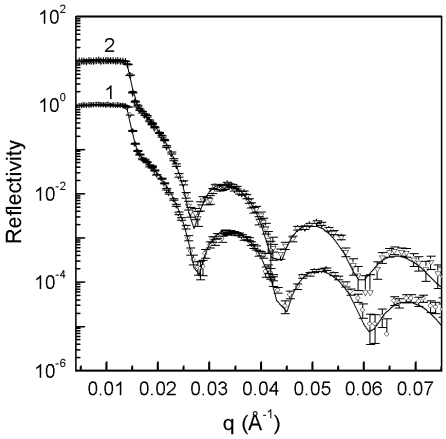

Figure 4.5. Neutron reflectivity profile of negatively charged PEI(PSS/PAH)$_6$PSS film in D_2O: 1) bare polymer surface, 2) polymer surface exposed to B18 peptide for 12 h. The continuous lines are profiles calculated using parameters of Table 4.1. The curves are offset vertically for clarity.

tion revealed small differences when compared to the bare surface (Figure 4.6). As can be observed on Figure 4.6 (a) the bare surface after incubation in buffer solution shows brighter structures closely packed, which are considered to be polymer aggregates. The roughness was estimated to be 21 ± 3 Å, which agrees with the value obtained by neutron reflectivity. After incubation in B18 peptide solution the surface became more covered and the clusters appeared to be larger (Figure 4.6 (b)). This change was attributed to the adsorption of B18 peptide on the polymeric film. However, it is not possible to distinguish peptide molecules from polymer aggregates. The roughness was essentially the same as that of the pure polymer (22 ± 2 Å). Nevertheless, as described in section 4.2.1, neutron reflectivity measurements showed that B18 peptide adsorbs on the polymeric film after 12 hours incubation time. Though adsorbed B18 could not be fitted as a single uniform layer and the roughness was large and similar to that obtained for the pure film, as observed by atomic force microscopy. This suggests that the peptide adsorbs in the form of patches, which are placed between the polymer aggregates.

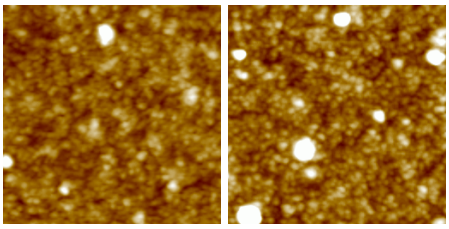

(a) 0 hours (b) 72 hours

Figure 4.6. AFM images of PEI(PSS/PAH)$_6$PSS film: (a) bare polymer, (b) polymeric film after incubation in B18 solution for 72 hours. Images were recorded at 1 x 1 μm scan. The Z range is 20 nm.

In order to better resolve the peptide structure on negatively charged surfaces, the adsorption of B18 on silicon oxide layer was characterized by atomic force microscopy. Neutron reflectivity measurements of these samples were not performed since the silicon oxide is a thin layer (less than 30 Å). For thin adsorbed layers, reflectivity at high values of q will give most of the structural information. However, as q increases the noise level increases and at high values of q (> 0.2 Å^{-1}), the reflectivity will rapidly fall off to the background level (due to incoherent scattering from the solvent). For $q < 0.15$ Å^{-1} the reflectivity of thin silicon oxide layer will give a fast signal decay without modulations (Kiessig fringes). As the peptide layer is expected to be thin, in the range of 10–20 Å, the changes in the overall thickness will not be easily detected.

Figure 4.7 (a) shows the atomic force microscopy images of initial bare silicon surface after incubation in buffer solution. As expected, the substrate surface is flat and featureless. Thus small changes in the morphology of the surface upon peptide adsorption are presumably easy to detect. At early times after exposing the silicon substrate to the peptide solution, no significant differences were found on the surface when compared to the

bare substrate (Figure 4.7 (b)). Increasing the incubation time to 12 hours, spherical structures closely packed are observed (Figure 4.7 (c)). Areas devoid of adsorbed molecules are also seen. After 24 hours incubation time the color of the structures became lighter, indicating that their heights increased (Figure 4.7 (d)). The surface coverage seems to be identical to that after 12 hours adsorption time. Finally longer incubation time (72 hours) led to the formation of a film which covered uniformly the surface (Figure 4.7 (e)).

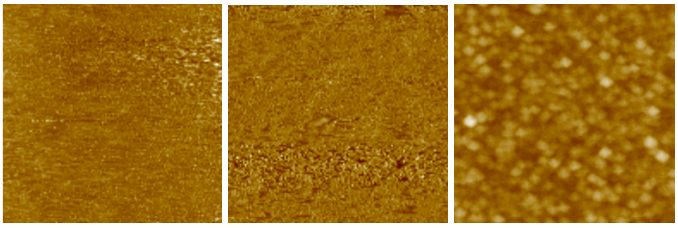

(a) 0 hours (b) 1 hour (c) 12 hours

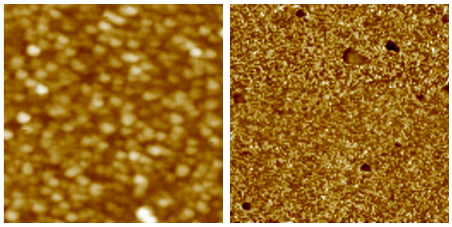

(d) 24 hours (e) 72 hours

Figure 4.7. AFM images of silicon oxide layer after incubation in B18 solution at different times. Images were recorded at 1 x 1 μm scan. The Z range is 10 nm.

The heights of the spherical structures were quantified by section analysis and the results are shown in Table 4.2. Aggregates of 13 ± 2 Å height were found after 12 hours adsorption time, which agrees with the thickness obtained for B18 adsorption layer on PEI(PSS/PAH)$_6$PSS film as determined by neutron reflectivity. After 24 hours adsorption time, heights of 16 ± 1 Å and 23 ± 2 Å were measured, indicating that molecules are adsorbing on already adsorbed peptide. The height of the film formed at 72 hours incubation time was estimated to be 23 ± 3 Å. The roughness was found to increase by about 8 Å (Table 4.2).

Time (h)	**Height (Å)**	**Roughness (Å)**
0	–	3.2 ± 0.1
12	13 ± 2	4.0 ± 0.2
24	16 ± 1; 23 ± 2	5.7 ± 0.4
72	23 ± 3	10.7 ± 0.3

Table 4.2. Height and roughness of adsorbed B18 on silicon substrates as determined by AFM. The mean values and confidence interval were obtained from at least five distinct areas.

Adsorption of B18 peptide onto negatively charged surfaces is a slow process. Long

incubation times are required to observe irreversible adsorption. One possible reason for the slow adsorption kinetics is that the peptide aggregates first in solution and it adsorbs in aggregated form. Indeed B18 is known to aggregate in solution at pH $\geq$ 7 [8, 45]. However, aggregation is concentration dependent and was observed at much higher concentrations than that used here. The most likely mechanism is that the peptide adsorbs as single molecules but it requires time to conformationally adjust to the surface. Considering that B18 has hydrophobic sequences at both ends of the molecule, it is possible that the peptide undergoes conformational changes when interacting with hydrophilic surfaces before irreversible adsorption. Additional molecules will preferentially adsorb on the top of those already adsorbed on the surface. The model of a second layer of peptide growing on the clusters is supported by the finding of different aggregate heights by atomic force microscopy. A long period of adsorption leads to an almost complete coverage of the surface.

Because B18 is positively charged and the bare silicon and PEI(PSS/PAH)$_6$PSS surfaces are negatively charged, there is an electrostatic attraction for the peptide to the surfaces. A possible driving force for adsorption of bulk peptide on already adsorbed molecules may result from the exposed hydrophobic residues, due to peptide conformational changes. Apparently, this process occurs on a faster time scale than that allowing molecules to adsorb on the surface. When bulk peptides come into contact with adsorbed molecules, the hydrophobic residues on each are available for agglomeration, which might be thermodynamically more favorable than adsorption on the bare charged surface.

4.2.3 Degree of Adsorption on Hydrophobic Surfaces

X-ray reflectometry of OTS layers after incubation in B18 solution revealed information about the adsorption degree of B18 on hydrophobic surfaces. After a defined adsorption period, the samples were rinsed with ultrapure water and dried in a nitrogen flow.

Figure 4.8 shows the reflectivity curve of the pure OTS layer (curve 1), which was fitted with a two-layer model, the first layer corresponding to the silicon oxide and the second layer to OTS. The electron density and the thickness of the bare OTS layer were 0.24 $e^-/Å^3$ and 24 Å, respectively. The reflectivity profile of the hydrophobic surface changed after incubation in B18 peptide solution. After 1 hour adsorption time, the reflectivity curve showed a pronounced shift of the position of the first minimum to smaller q values and a second minimum was observed (Figure 4.8, curve 2). This is interpreted as an increase of the film thickness. The best fit of the reflectivity data was obtained with a three-layer model (silicon oxide, OTS and peptide layer). The structural parameters of the hydrophobic OTS were identical to the ones obtained for the bare layer. An additional layer with an electron density of 0.11 $e^-/Å^3$ and a thickness of 23 Å was observed. After 72 hours incubation time the reflectivity curve showed an increase in the amplitude of the fringe when compared with the profile after 1 hour adsorption time (Figure 4.8, curve

3). In addition, the distance between the two minima changed. These are indications that the thickness and composition of the surface changed. The fitting parameters showed an OTS layer with an electron density of 0.26 $e^-/Å^3$ and a thickness of 23 Å. The electron density and thickness of the peptide layer changed to 0.16 $e^-/Å^3$ and 20 Å, respectively. The fitting parameters of the reflectivity curves are summarized in Table 4.3.

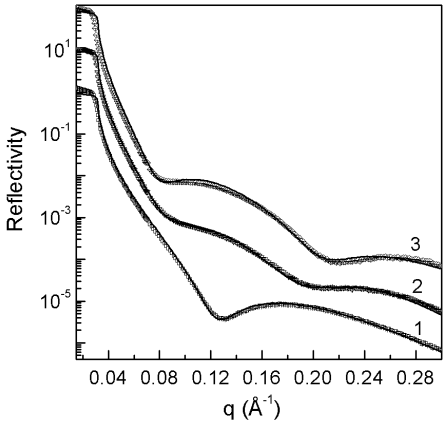

Figure 4.8. X-ray reflectivity profile of OTS layer after incubation in buffer solution (curve 1) and in B18 peptide solution for 1 hour (curve 2) and 72 hours (curve 3). The curves were fitted using parameters of Table 4.3 (continuous line). The curves are offset vertically for clarity.

layer	**d (Å)**	ρ_e **($e^-/Å^3$)**	σ**(Å)**
bare layer			
OTS	23.8 ± 0.3	0.24 ± 0.01	2.7 ± 0.2
silicon oxide	11.0 ± 3.0	0.72 ± 0.11	7.6 ± 0.2
1h adsorption time			
peptide	22.8 ± 0.8	0.11 ± 0.01	3.9 ± 0.7
OTS	24.0 ± 0.7	0.24 ± 0.01	2.6 ± 0.6
silicon oxide	11.0 ± 2.0	0.72 ± 0.01	7.8 ± 0.3
72h adsorption time			
peptide	19.8 ± 0.7	0.16 ± 0.01	3.9 ± 0.6
OTS	23.1 ± 1.1	0.26 ± 0.01	1.0 ± 0.9
silicon oxide	11.0 ± 6.0	0.72 ± 0.02	7.8 ± 0.6

Table 4.3. Structural parameters used to fit the reflectivity profiles measured for the system OTS layer and B18 peptide. d, ρ_e and σ are the thickness, electron density and roughness, respectively.

When OTS is exposed to B18 peptide solution, X-ray reflectivity data indicate that even after rigorous rinsing with water, there is a layer of peptide adsorbed on the hydrophobic

surface. This indicates that B18 peptide shows high affinity for hydrophobic surfaces, which is likely caused by its seven leucine residues, that contribute to a decrease in free energy on going from the aqueous environment (initial state) to the hydrophobic interface (final state). Lower electron density obtained from the X-ray reflectivity data for 1 hour adsorption time comparing with 72 hours suggests that at early times the coverage of the surface was less uniform. In addition the thickness of the peptide layer was found to decrease with time which might indicate diffusion of peptide molecules to the free sites on the substrate.

In order to better understand the mechanism of B18 adsorption on the OTS layer, atomic force microscopy measurements were performed.

4.2.4 Imaging B18 Adsorption on Hydrophobic Layer

Figure 4.9 shows representative topographic images of OTS at different incubation times in B18 solution. The bare OTS layer was uniform and no special features were observed (Figure 4.9 (a)). After 10 minutes incubation time no significant differences were observed in the layer when compared to the bare substrate (Figure 4.9 (b)). In contrast, after 20 minutes the surface was different from the bare substrate. In this case the surface was covered with structures in a well defined arrangement that resembled a network (Figure 4.9 (c)). The surface coverage increased with time and the pattern became more dense (Figure 4.9 (d) and (e)). After 72 hours adsorption time the surface was covered more uniformly but many small regions devoid of adsorbed molecules were observed (Figure 4.9 (f)).

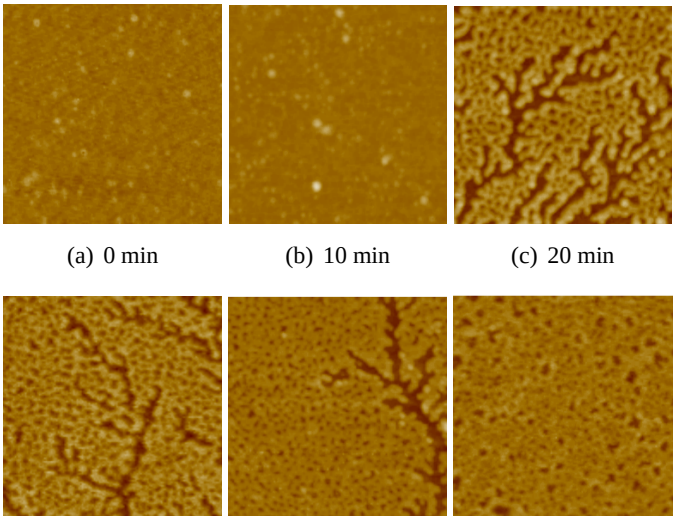

(a) 0 min (b) 10 min (c) 20 min

(d) 1 hour (e) 2 hours (f) 72 hours

Figure 4.9. AFM images of OTS layer after incubation in B18 solution at different times. Images were recorded at 1 x 1 μm scan. The Z range is 20 nm.

At incubation times up to 2 hours aggregates with a fractal like morphology were observed. Elongated structures appeared to grow from amorphous aggregates (Figure 4.10).

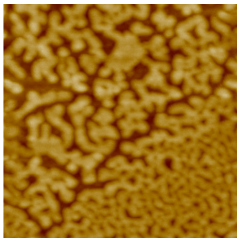

Figure 4.10. AFM image of B18 aggregates on OTS layer after 2 hours adsorption time. The image was recorded at 500 x 500 nm scan. The Z range is 20 nm.

Section analysis of the images showed that at early adsorption times the heights of the structures were not uniform (Figure 4.11 (a)). Heights of 25 $\pm$ 1 Å and 37 $\pm$ 2 Å were measured after 20 minutes adsorption time. Similarly, structures of two distinct heights were found after 1 hour (23 $\pm$ 1 Å and 32 $\pm$ 2 Å) and after 2 hours incubation time (20 $\pm$ 1 Å; 34 $\pm$ 2 Å). Higher structures were preferentially located at the boundary between covered and bare areas and decreased in number with time. After 72 hours, the higher area disappeared and the height amounted to 20 $\pm$ 1 Å. The surface roughness after peptide adsorption decreased as a function of time (Figure 4.11(b)). Similar trends were found with X-ray reflectivity measurements.

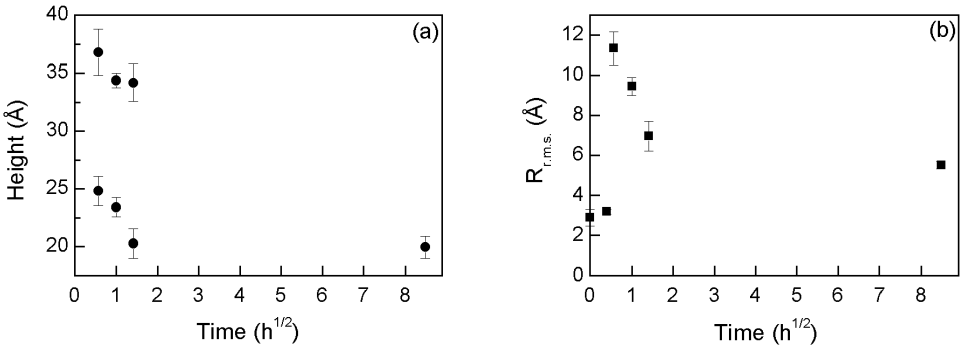

Figure 4.11. Height (a) and roughness (b) of B18 peptide adsorbed on OTS layer as a function of time as determined by AFM. The square root of time is used to distinguish the experimental points. The mean values and confidence intervals were obtained from at least five independent areas.

Adsorption of B18 onto hydrophobic OTS is faster than onto hydrophilic surfaces. This indicates that B18 has a lower activation free energy of adsorption on hydrophobic surfaces than on hydrophilic surfaces. Yet, irreversible adsorption on hydrophobic surfaces takes more than 10 minutes suggesting that also in this case the peptide requires time to conformationally adjust to the surface. It is not possible to determine unambiguously

whether the peptide adsorbs as single molecule or in aggregated form. However, it is likely that aggregation occurs on the surface since in solution higher concentrations and longer times are required for peptide assembly [8]. The following mechanism for B18 adsorption on OTS layer is proposed. Single molecules adsorb irreversibly on the surface after conformational arrangement. Additional molecules will preferentially adsorb from the bulk solution on those already adsorbed. Afterwards, molecules will undergo conformational changes and will diffuse to the free sites on the substrate. This would explain why the heights of aggregates decrease with time. It is possible that two-dimensional lateral diffusion on the surface affects the adsorption process of B18 on OTS layers. It is known that polymers can undergo rapid lateral diffusion on surfaces. The high local concentration of peptide in the amorphous deposit could well act as a reservoir of elongated structures, which would be a more stable state. The growing of amyloid fibrils from amorphous aggregates has been reported for a recombinant amyloidogenic immunoglobulin light chain [101]. It is possible that fibril formation by B18 peptide follows a similar mechanism. The presence of amorphous aggregates may serve as nucleation sites for fibril growth. This process might constitute an important mechanism of fibril formation.

4.2.5 Functional Implications

Although B18 peptide is known to induce fusion of lipid vesicle systems [7], the fusion mechanism is poorly understood. The adsorption behavior of B18 on hydrophilic and hydrophobic surfaces may provide some information about this process. The results of this study point that most likely single peptide molecules interact with the hydrophilic membrane surface, resulting in conformational change. Hydrophobic interactions will then lead to aggregation of peptide molecules which will allow the formation of a membrane defect. Since the peptide has high affinity for hydrophobic surfaces, it will then penetrate and diffuse in the target membrane.

The type of B18 aggregates is though to determine the peptide functional state [8]. The fusion activity of B18 is promoted by zinc ions, which induce the formation of globular clusters of the peptide. Similar aggregates were observed on negatively charged surfaces, as described in section 4.2.2. In the absence of zinc, the peptide is rapidly inactivated at pH $\geq$ 7 by aggregation into amyloid fibrils [8]. Whether the fibrils are functional relevant for the fusion process is not clear. However, fibril formation is believed to lead to a disruption of the membrane rather than fusion [8]. A similar mechanism may as well be observed for amyloidogenic peptides when interacting with cellular membranes. It has been suggested that the lipid membrane might play a catalytic role in the nucleation or self-assembly process of amyloid fibrils, which would lead to a perturbation of the membrane [102].

4.3 Characterization of Amyloid beta-Peptide Adsorption

The interaction of amyloid β-peptide (1–40) with hydrophilic and hydrophobic surfaces has been characterized by neutron reflectivity. The structural parameters of the pure films were first determined by measuring their reflectivity profiles in D_2O. The subphase was then exchanged by a solution of amyloid β-peptide (1–40) in D_2O at a concentration of 4.6 μM. Neutron reflectivity measurements were repeated after 12 hours of exposure. The pD values of the peptide solutions were obtained by adding 0.4 units to the pH-meter readings [103]. The mean value and confidence interval of pD of all solutions used in the neutron reflectivity measurements were 7.1 ± 0.2. The peptide was in random coil conformation as determined by circular dichroism spectroscopy.

4.3.1 Adsorption at Hydrophilic Solid/Liquid Interfaces

The amyloid β-peptide (1–40) was allowed to adsorb on formvar and on the multilayer films PEI(PSS/PAH)$_6$PSS and PEI(PSS/PAH)$_6$. The neutron reflectivity profile of pure formvar film in D_2O is shown in Figure 4.12 (curve 1). The thickness of the film was evaluated from the position of the minima of two consecutive fringes using equation (3.21) and was determined to be 270 Å. The reflectivity profile of the non-charged film after exposure to amyloid solution showed no significant differences from the curve of the pure layer (Figure 4.12, curve 2).

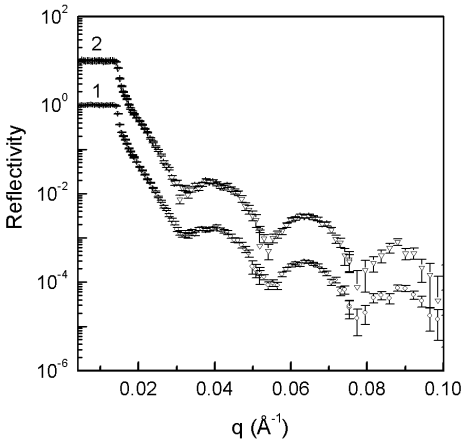

Figure 4.12. Neutron reflectivity profiles of non-charged formvar film in D_2O: 1) bare polymer surface; 2) polymer surface exposed to amyloid β-peptide solution for 12 h. The curves are offset vertically for clarity.

The reflectivity curve of the PEI(PSS/PAH)$_6$PSS film in D_2O yielded a thickness of 405 Å for the polyelectrolyte multilayers by using equation (3.21) (Figure 4.13, curve 1).

No significant changes were observed in the reflectivity profile of negatively charged films after exposure to amyloid β-peptide solution when compared to the bare polymer (Figure 4.13, curve 2).

In both cases no differences in the position of the minima and amplitude of the fringes were observed after long exposure time to amyloid β-peptide solution. This is an indication that adsorption or penetration of the peptide on non-charged and negatively charged hydrophilic films did not occur.

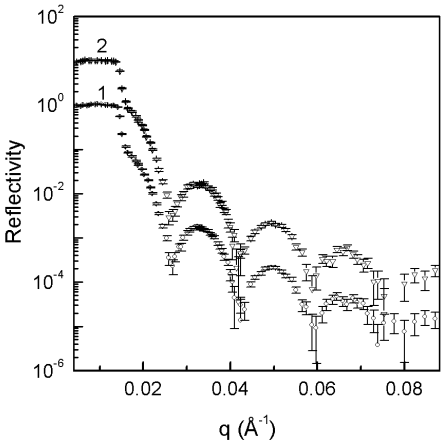

Figure 4.13. Neutron reflectivity profiles of negatively charged PEI(PSS/PAH)$_6$PSS film in D_2O: 1) bare polymer surface; 2) polymer surface exposed to amyloid β-peptide solution for 12 h. The curves are offset vertically for clarity.

The adsorption of amyloid β-peptide on positively charged film showed a different behavior. In contrast to the non-charged and negatively charged films, the PEI(PSS/PAH)$_6$ profile changed after exposure to amyloid β-peptide (1–40) solution (Figure 4.14). A pronounced shift of the position of the minima to lower q values was observed in the reflectivity curve after 12 hours adsorption time. This is an evidence that the thickness increased, indicating the formation of an additional adsorption layer on PEI(PSS/PAH)$_6$ film.

The reflectivity curve of the bare film was fitted with a two-layer model. The first layer represents the silicon oxide layer and the second one the bare film. A scattering length density of 4.1 x 10^{-6} Å^{-2} and a thickness of 308 Å were obtained for the pure film. The reflectivity curve after amyloid β-peptide adsorption was fitted adding an additional layer to the previous model. However, it was found that the surface coverage was not uniform. The best fit was obtained with a surface coverage of 0.6, suggesting that the peptide adsorbs as patches dispersed over the surface. According to the fitting parameters these aggregates have a scattering length density of 3.4 x 10^{-6} Å^{-2} and a thickness of

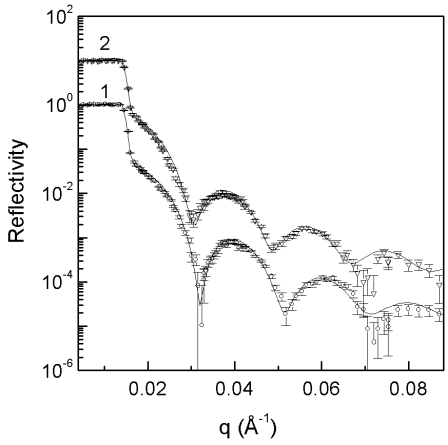

Figure 4.14. Neutron reflectivity profiles of positively charged PEI(PSS/PAH)$_6$ film in D_2O: 1) bare polymer surface; 2) polymer surface exposed to amyloid β-peptide solution for 12 h. The curves were fitted using parameters of Table 4.4 (continuous line). The curves are offset vertically for clarity.

20 Å. The structural parameters obtained from the models used to fit the reflectivity curves are resumed in Table 4.4.

layer	**d (Å)**	ρ **(10^{-6}Å^{-2})**	σ**(Å)**
silicon oxide	6 ± 4	3.48 ± 0.41	2 ± 1
film	308 ± 2	4.10 ± 0.04	3 ± 2
peptide	20 ± 1	3.40 ± 0.07	2 ± 1
D_2O	–	6.37 ± 0.18	17 ± 1

Table 4.4. Structural parameters used to fit the reflectivity profile of the system PEI(PSS/PAH)$_6$ and amyloid β-peptide. The surface coverage of peptide adsorption layer was estimated to be 0.6. d, ρ and σ are the thickness, scattering length density and roughness, respectively.

The electrostatic attraction between a charged surface and oppositely charged protein is often the driving force for protein adsorption on the hydrophilic solid substrate [100]. In addition to electrostatic attraction, a further driving force for protein adsorption is attributed to entropic changes associated with dehydration of the protein and surface and/or structural rearrangement within the protein [100].

At pD 7, partial deprotonation of the histidines residues of amyloid β-peptide is expected to occur and hence the net charge of the peptide at this pD value is negative [104]. Adsorption of amyloid β-peptide on hydrophilic non-charged surface was not observed likely due to the absence of electrostatic attraction. Similar behavior was observed at zwitterionic phosphatidylethanolamine monolayers, which can be compared with non-charged surfaces [94]. No adsorption of the peptide at the lipid monolayer was observed at sur-

face pressure above 30 mN m^{-1}. On hydrophilic negatively charged surfaces, the absence of adsorption is attributed to electrostatic repulsion between the peptide and the surface. Circular dichroism measurements showed that amyloid β-peptide exhibits mainly random coil secondary structure when dissolved in D_2O. Zhang et al. found that amyloid β-peptide (10–35) adopts a collapsed coil structure in D_2O, which was considered an intermediate meta-stable state [105]. The peptide molecule has a compact well-defined conformation within its hydrophobic core stabilized by van der Waals and electrostatic interactions, whereas the flanking regions are partially disordered. Amyloid β-peptide (1–40) exhibits two hydrophobic clusters: residues 17 to 21 and residues 29 to 40. In the collapsed coil conformation, these clusters are expected to be in the interior of the structure. However, a hydrophobic patch was observed on the surface of the molecule [105]. This hydrophobic patch could be an additional reason for a thermodynamically unfavorable situation for adsorption on hydrophilic non-charged and negatively charged surfaces used in this study.

The fact that amyloid β-peptide adsorbs on the positively charged film suggests that electrostatic attraction between the peptide and the PAH surface occurs. In addition, adsorption may be driven by an entropy gain caused by dehydration of surface and peptide and/or conformational entropy gain resulting from structural changes in the peptide. When compared with PSS polymer, PAH is less hydrophilic. Neutron reflectivity measurements have shown that six water molecules are bound per PSS monomer while one water molecule is bound per PAH monomer [98]. Since amyloid β-peptide has a hydrophobic patch on the surface, the molecule will have higher affinity for PAH than for PSS, resulting in an entropic gain. This would explain why the peptide adsorbed on the positively charged film but not on the negatively charged one, even when both positive and negative charges are present in the molecule.

4.3.2 Adsorption at Hydrophobic Solid/Liquid Interfaces

The amyloid β-peptide (1–40) was allowed to adsorb on polysiloxane-surfactant film. The reflectivity profile of the hydrophobic surface changed after injection of amyloid β-peptide solution. The profile of the polysiloxane-surfactant complex after 12 hours in contact with the peptide solution showed a shift in the position of the minimum of the interference fringe to lower q values, when compared with the reflectivity profile curve of the pure film (Figure 4.15).

The neutron reflectivity curve of the pure film was fitted with a two-layer model. The layer closer to the silicon substrate corresponds to the silicon oxide layer and has a scattering length density of 3.47 x 10^{-6} $Å^{-2}$ and a thickness of 9 Å. The silicon oxide layer is followed by a second one with low scattering length density of 0.68 x 10^{-6} $Å^{-2}$, which is typical for organic materials. This layer must be composed of the polysiloxane-surfactant complex. The reflectivity profile after injection of the peptide solution was fitted with a

three-layer model. In addition to the two layers observed, an additional layer with a scattering length density of 3.13 x 10^{-6} Å^{-2} and a thickness of 12 Å was found after amyloid β-peptide adsorption. This layer consists of the peptide adsorbed onto the hydrophobic polysiloxane-surfactant complex. The fitting parameters are summarized in Table 4.5. The measurements were repeated 59 hours after peptide injection, but there were no differences between this reflectivity curve and the one observed after 12 hours adsorption time.

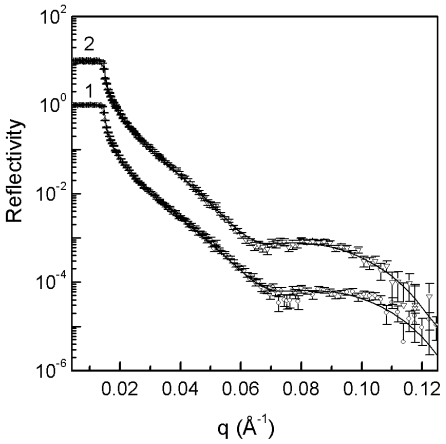

Figure 4.15. Neutron reflectivity profiles of polysiloxane-surfactant complex in D_2O: 1) bare polymer surface; 2) polymer surface after amyloid β-peptide adsorption. The continuous lines are profiles calculated using parameters of Table 4.5. The curves are offset vertically for clarity.

layer	**d (Å)**	ρ **(10^{-6}Å^{-2})**	σ**(Å)**
silicon oxide	9 ± 1	3.47 ± 0.14	5 ± 1
complex	101 ± 1	0.68 ± 0.16	8 ± 2
peptide	12 ± 1	3.13 ± 0.09	2 ± 1
D_2O	–	6.36 ± 0.14	12 ± 2

Table 4.5. Structural parameters used to fit the reflectivity profile of the system polysiloxane-surfactant complex and amyloid β-peptide. d, ρ and σ are the thickness, scattering length density and roughness, respectively.

Additionally, the adsorption of amyloid β-peptide (1–40) on a polystyrene surface was studied. The reflectivity from the bare silicon block covered with a polystyrene layer is shown in Figure 4.16 (curve 1). The evaluation of the data revealed the formation of a layer with a scattering length density of 1.96 x 10^{-6} Å^{-2}. The reflectivity from the same sample after 12 hours of amyloid β-peptide adsorption showed a pronounced shift of the position of the minimum to lower q values (Figure 4.16, curve 2). This indicates an

increase in the film thickness that corresponds to the formation of an additional adsorption layer on top of the polystyrene film.

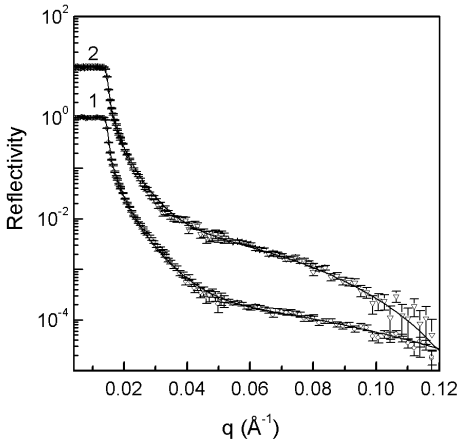

Figure 4.16. Neutron reflectivity profiles for polystyrene in D_2O: 1) bare polymer surface; 2) polymer surface after amyloid β-peptide adsorption. The continuous lines are profiles calculated using parameters of Table 4.6. The curves are offset vertically for clarity.

The best fit to the reflectivity data after peptide adsorption was obtained with a three-layer model (Table 4.6). Again, the formation of a layer with a scattering length density of 3.13 x 10^{-6} Å^{-2} was observed. The thickness of this layer (20 Å) is larger when compared with the adsorption layer on the polysiloxane-surfactant complex.

layer	**d (Å)**	ρ **(10^{-6}Å^{-2})**	σ**(Å)**
silicon oxide	21 ± 2	3.47 ± 0.13	11 ± 5
polystyrene	31 ± 2	1.96 ± 0.05	5 ± 4
peptide	20 ± 2	3.13 ± 0.29	3 ± 2
D_2O	–	6.36 ± 0.05	2 ± 1

Table 4.6. Structural parameters used to fit the reflectivity profile of the system polystyrene and amyloid β-peptide. d, ρ and σ are the thickness, scattering length density and roughness, respectively.

On a hydrophobic surface, attraction occurs between the hydrophobic surface and hydrophobic fragments within the protein [100]. The folding of a polypeptide chain in aqueous solution involves a considerable loss of conformational entropy but this is compensated by a gain in energy due to the removal of the hydrophobic residues from contact with water [21]. The hydrophobic surface, however, provides a region on which the peptide backbone can unfold without exposure of the hydrophobic residues to water [100]. Since amyloid β-peptide has two hydrophobic domains, residues 17 to 21 and residues 29 to 40, it can interact with hydrophobic surfaces, resulting in adsorption.

4.3.3 Conformational Implications

In an experiment where species p are adsorbed on a surface from aqueous solution, as an uniform layer, the scattering length density of the adsorbed layer, ρ_{exp}, is made up of a contribution from the species and from water, w, present in the layer

$$\rho_{exp} = \rho_p \phi_p + (1 - \phi_p)\rho_w, \tag{4.1}$$

where ϕ_p is the volume fraction of species p in the layer. The scattering length density of the peptide can be obtained from

$$\rho_p = \frac{\sum m_i b_i}{V_m}, \tag{4.2}$$

where V_m is the molecular volume of the peptide, m_i and b_i represent the stoichiometry and the scattering length of the elements in the peptide molecule (carbon, hydrogen, oxygen, nitrogen and sulphur). The element scattering lengths b_i are taken from the literature [106]. Because the peptide contains labile hydrogens on the backbone and amino acid side groups, which readily exchange with D_2O, the effect of H/D exchange on the total scattering length of the peptide has to be considered. The H/D exchange of amyloid β-peptide was determined by nuclear magnetic resonance to be 66 [107]. The molecular volume of the peptide was estimated by adding the partial volumes of all amino acid residues, leading to a value of 5120 $Å^3$ [25]. The scattering length density of the peptide was subsequently calculated to be 3.34 x 10^{-6} $Å^{-2}$. The value is very close to the scattering length density of the peptide layer adsorbed on hydrophobic surfaces obtained from the model used to fit the reflectivity profiles described in section 4.3.2. This suggests that the peptide formed a very tightly packed layer, which does not contain D_2O. The accuracy of this value is affected by the estimated molecular volume. However, a similar value for the thickness of adsorbed peptide was found after drying the samples in a nitrogen flow, suggesting that the amount of water in the layer was very low. In addition the peptide was found to form a packed uniform layer on different hydrophobic surfaces such as OTS layer, as observed by atomic force microscopy (Figure 4.17).

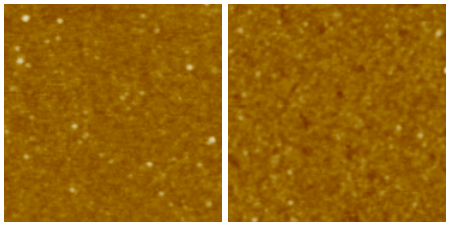

(a) 0 hours (b) 36 hours

Figure 4.17. AFM images of OTS layer after incubation in amyloid β-peptide solution. Images were recorded at 1 x 1 μm scan. The Z range is 10 nm.

It is likely that the peptide adopts a β-sheet structure upon adsorption on hydrophobic surfaces. A tightly packed layer agrees with the formation of β-structures. Amyloid

β-peptide was previously found to be in a β-sheet structure at the air-water interface [93,94]. Additionally the formation of uniform, elongated sheets on hydrophobic graphite by the peptide has been described [92]. X-ray diffraction studies indicate that amyloid fibrils are composed of more than one β-sheet, stacking face to face, with an inter-sheet spacing of approximately 10 Å [62]. The 12 Å obtained for adsorbed peptide layer on polysiloxane-surfactant complex agrees with the presence of one pleated sheet, whereas the 20 Å of amyloid adsorbed layer indicates that at most two pleated sheets exist. This means that the conformational rearrangement of amyloid β-peptide in β-sheet structure and further aggregation occur more rapidly on polystyrene film than on polysiloxane-surfactant complex polymer.

For the system positively charged PEI(PSS/PAH)$_6$ film and amyloid β-peptide, described in section 4.3.1, the adsorbed layer was not uniform. However, it is possible to compare the value of the scattering length density obtained for the peptide patches with the calculated value. Also in this case the values are very close, which indicates that the patches are tightly packed. In addition circular dichroism measurements showed that PAH polymer induces a β-sheet structure in amyloid β-peptide (Figure 4.18). Thus the peptide within the patches adsorbed on the positively charged film might be in a β-sheet structure.

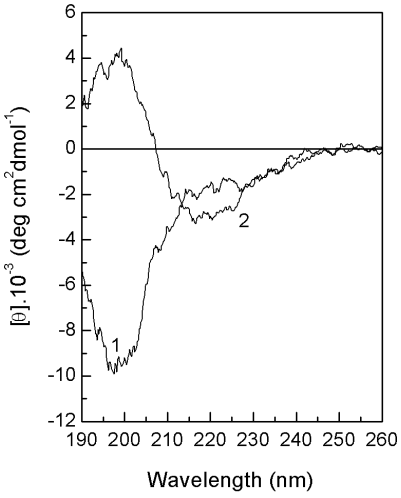

Figure 4.18. Circular dichroism spectra of amyloid β-peptide in the presence of PAH polymer: 0 mg mL^{-1} (curve 1) and 1 mg mL^{-1} (curve 2).

Opposed to this, no conformational changes are observed in amyloid β-peptide when incubated in hermetically closed quartz cuvettes previously treated by the RCA procedure. After this procedure the quartz surface is highly hydrophilic and negatively charged. Circular dichroism measurements showed that the peptide is mainly in random coil conformation when in contact with negatively charged quartz surfaces for more than 2 weeks

(Figure 4.19 (a)). This was not the behavior observed for the peptide solution when incubated in test tubes. In this case a transition from random coil to β-sheet structure occurred (Figure 4.19 (b)).This might be explained by the fact that in the test tubes amyloid β-peptide was in contact with air, whereas in the quartz cuvettes this interaction was prevented. The air-water interface acts as a hydrophobic-hydrophilic surface to which the peptide has high affinity resulting in a β-sheet conformation. The peptide was previously found to adsorb at air-water interface and merely β-sheet structure was detected [94].

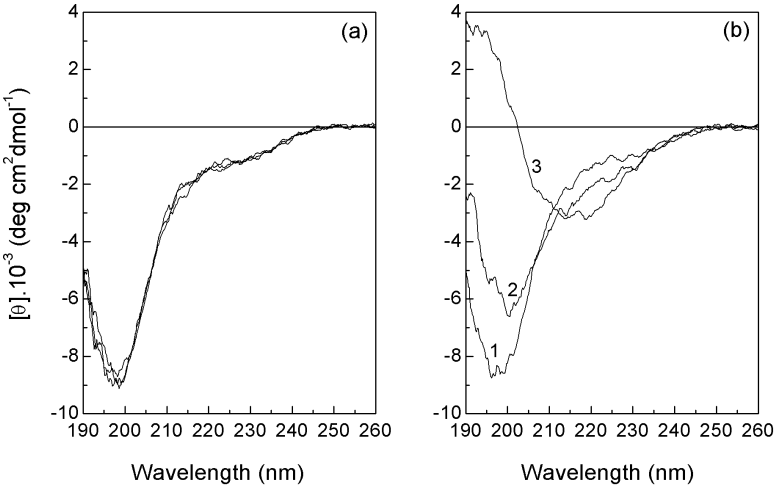

Figure 4.19. Circular dichroism spectra of amyloid β-peptide stored in negatively charged quartz cuvettes (a) and in test tubes (b) at different times: 10 minutes (curve 1), 4 days (curve 2) and 20 days (curve 3). The curves of (a) overlap.

Whereas no adsorption is observed on hydrophilic non-charged and negatively charged films, amyloid β-peptide adsorbs on hydrophobic surfaces and hydrophilic positively charged film. Structure prediction studies have indicated that the C-terminal 10 residues and residues 17–21 of the peptide show the greatest hydrophobicity [30]. Thus the peptide is thought to interact with hydrophobic surfaces through its hydrophobic domains, residues 17 to 21 and residues 29 to 40. Adsorbed peptide on hydrophobic surfaces likely adopts a β-sheet conformation. A schematic representation of the amyloid β-peptide layer adsorbed on hydrophobic surfaces is shown in Figure 4.20. The adsorbed peptide is represented as a monolayer that is assumed to correspond to a β-pleated sheet. If this is the case the distance between the peptide molecules (β-strands) within the pleated sheet is 4.7 Å and the thickness of the β-pleated sheet is approximately 10 Å as described for amyloid fibrils [6, 62]. This value is close to the one obtained for the thickness of peptide layer adsorbed on the polysiloxane-surfactant complex.

In the case of the positively charged surface an entropy gain must be the driving force

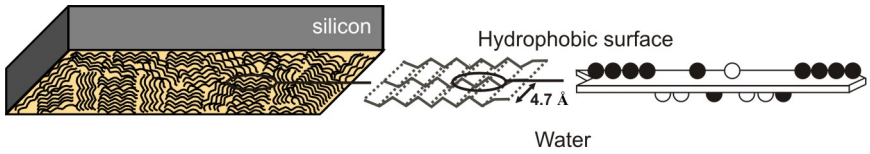

Figure 4.20. Schematic representation of amyloid β-peptide layer adsorbed on hydrophobic surfaces. The hydrophobic residues and charged polar residues are shown in black and white, respectively.

for adsorption. The polymer that formed the surface was found to induce a β-sheet structure on the peptide. Therefore it is assumed that the peptide adsorption results in a conformational transition from random coil to β-sheet structure. Since adsorption or conformational transitions were not observed in the case of negatively charged surfaces, β-sheet formation seems to result from peptide adsorption.

5 Interaction of Amphiphiles with Self-Assembled Peptides

Detergent micelles are widely used as models to study the structure of peptides in membrane mimicking systems. In the case of peptides with fusogenic properties and ability to form fibrils such as B18 and amyloid β-peptide, these studies might provide insights into the role of membranes in amyloid fibril formation and into the mechanism of perturbation of membranes.

B18 peptide as well as several viral fusion peptides tend to self-associate into amyloid fibrils in membrane-bound state and it has been suggested that the fibril formation leads to a perturbation of membranes [8, 44]. Previous studies have shown that the C-terminal domain of amyloid β-peptide has fusogenic properties [10] and that the peptide disrupts membranes containing acidic lipids [102]. The fact that amyloid β-peptide derives from a transmembranar protein and that its oligomeric forms are toxic to neurons [60, 61] associated with a perturbation of lipid composition observed in Alzheimer's disease [108, 109] indicates that interactions of the peptide with cellular membranes might be related to the development of the disease.

Moreover the investigation of interaction effects between amyloid peptides and micelles might be relevant for the development of therapeutic agents that stabilize the monomeric form of the peptides or inhibit the fibril formation. Amyloid β-peptide seems to be released as a monomeric soluble peptide and to require a minimal level of aggregation to exert neurotoxicity [40, 57, 60, 61].

The conformation of amyloid β-peptide in water-micelle environments has been extensively described in the literature [110–115]. However, several of these studies were carried out with shorter fragments of the amyloid β-peptide (1–40) and (1–42) [110, 112, 113]. In addition, the reports of solution structure of the 40 and 42 amino acid sequences in detergent micelles concerned essentially the influence of sodium dodecyl sulphate micelles [111, 114, 115]. In this work the study is extended to cationic, anionic perfluorinated and nonionic micelles. The concentration dependent effect of the different amphiphiles on the structure of B18 and amyloid β-peptide (1–40) was characterized by circular dichroism spectroscopy.

The aim of this study is to better understand the interaction of amyloid peptides with charged and nonionic amphiphiles.

5.1 Amphiphiles

The amphiphiles used were sodium dodecyl sulphate (SDS), pentadecafluorooctanoic acid (PFOA), cetyltrimethylammonium chloride (CTAC), and 1-*O*-*n*-octyl-β-D-glucopyranoside (OG) (Figure 5.1).

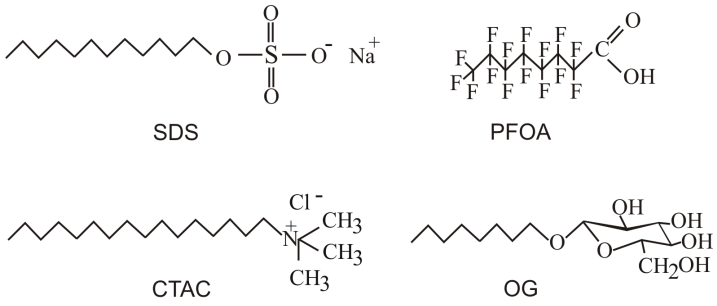

Figure 5.1. Chemical structure of the amphiphiles used in the study of interaction effects with amyloid peptides.

The properties of the amphiphiles are summarized in Table 5.1. The ionic amphiphiles were selected in order to have micelles with approximately the same shape. Octyl glucoside was chosen because of its purity when compared with other nonionic surfactants and due to its very little effect on the properties of membrane proteins and membrane associated-protein complexes, that permits to reconstitute proteins without denaturation [116–118].

Amphiphile	cmc (mM)	Shape of micelle	Size of micelle (nm)	Aggregation number
SDS[a]	8.0	spherical	4.8	78
PFOA[b]	9.1	disk-like		
CTAC[c]	1.4	spherical	4.8	90
OG[d]	25	cylinder	R = 1.3; L = 9.6	90

[a,c] [116, 119], [b] [120], [d] [121]

Table 5.1. Properties of the amphiphiles used in the study of interaction effects with amyloid peptides. cmc is the critical micellar concentration. For OG, *R* is the radius of the cylinder, and *L* is its length.

Stock solutions were prepared by dissolving the surfactants in double distilled water and adjusting the pH to 7 with KOH or HCl (ionic strength $< 10^{-3}$ M). Peptide-amphiphile solutions were prepared with amphiphile concentrations below and above the corresponding critical micellar concentration (cmc), in order to study the effect of the monomers and micelles on the peptide structure.

5.2 Secondary Structure of B18 Peptide in Amphiphile Solutions

The effect of amphiphiles on the secondary structure of B18 peptide was investigated at pH 7, with a final peptide concentration of 96 μM. B18 peptide exhibits, in the absence of amphiphiles, a circular dichroism spectrum characteristic of random coil conformation (minimum at 198 nm). The content of structure motifs was estimated to be 3% α-helix, 19% β-sheet, 10% β-turn and 68% random coil, using the method CONTIN/LL.

Figure 5.2 shows the circular dichroism spectra of B18 peptide in SDS solutions at concentrations ranging from 1.7 to 50.3 mM. At low concentration of SDS (1.7 mM), B18 peptide exhibits a spectrum with two negative bands, at 222 nm and 208 nm, and a positive band at 190 nm, which is an indication of the presence of α-helix structure (Figure 5.2, curve 2). At higher SDS concentrations (5.0, 16.8 and 50.3 mM), the spectra showed as well characteristic bands of α-helix but the bands were less pronounced when compared with the spectrum at 1.7 mM SDS (Figure 5.2, curves 3 to 5). This suggests that the α-helix content decreased at higher concentrations of SDS.

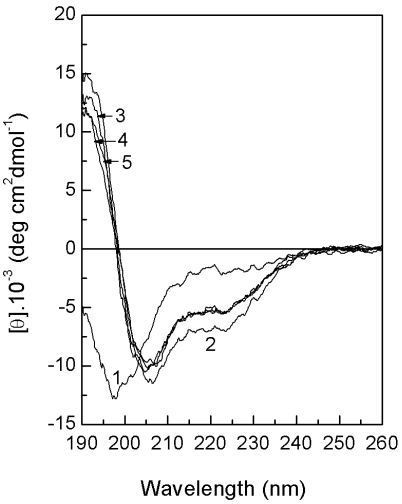

Figure 5.2. Circular dichroism spectra of B18 peptide in aqueous solution containing SDS at concentrations of 0.0 mM (curve 1), 1.7 mM (curve 2), 5.0 mM (curve 3), 16.8 mM (curve 4) and 50.3 mM (curve 5).

Quantitative analysis of the fraction of secondary structures showed the maximum α-helix content at 1.7 mM SDS (36%, Table 5.2). It can be seen in Table 5.2 that the increase in α-helix upon addition of SDS amphiphile (from 3% to 36%) is more due to a reduction of the random coil content (from 68% to 25%) than to the reduction of β-sheet or β-turn structures. Higher SDS concentrations decreased the helix inducing effect of

the amphiphile, leading to an α-helix content of about 20%.

Conc. (mM)	Helix (%)	Strand (%)	Turn (%)	Unordered (%)
0.0	3	19	10	68
1.7	36	22	17	25
5.0	23	21	19	37
16.8	21	22	17	40
50.3	20	23	18	39

Table 5.2. Secondary structure estimation of B18 peptide in SDS solutions by the CONTIN/LL program ($\pm$ 3%).

The effect of anionic perfluorinated amphiphile PFOA on B18 peptide is shown in Figure 5.3. Similar to those obtained in the SDS system, the circular dichroism spectra of B18 peptide in 1.8 and 5.4 mM PFOA, which are below the cmc of the amphiphile, showed characteristics of α-helix structure and remained unchanged at micellar PFOA concentrations.

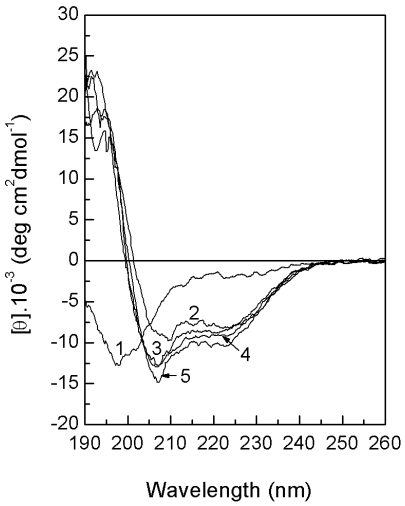

Figure 5.3. Circular dichroism spectra of B18 peptide in aqueous solution containing PFOA at concentrations of 0.0 mM (curve 1), 1.8 mM (curve 2), 5.4 mM (curve 3), 18.0 mM (curve 4) and 54.0 mM (curve 5).

The content of helicity of B18 was estimated to be in the range of 34–40% in the presence of PFOA (Table 5.3). The random coil fraction decreased from 68%, in absence of amphiphile, to 29–33% upon addition of the anionic perfluorinated amphiphile. The β-sheet and β-turn structure content changed only slightly. Thus, similar to the effect of SDS, the increase of α-helix was more due to a reduction of the random coil content than to a reduction of β-sheet and β-turn structures. This is supported by the finding of an

isosbestic point at 203 nm in the spectra of B18 measured in the absence and presence of PFOA at concentrations ranging from 5.4 to 54.0 mM (Figure 5.3, curves 1 and 3 to 5).

Conc. (mM)	Helix (%)	Strand (%)	Turn (%)	Unordered (%)
0.0	3	19	10	68
1.8	34	16	17	33
5.4	40	16	16	29
18.0	36	15	20	29
54.0	40	10	18	32

Table 5.3. Secondary structure estimation of B18 peptide in PFOA solutions by the CONTIN/LL program ($\pm$ 3%).

Interaction of B18 with the positively charged CTAC amphiphile showed predominantly a random coil conformation of the peptide at a concentration of 0.3 mM and an α-helix structure at higher concentrations (Figure 5.4).

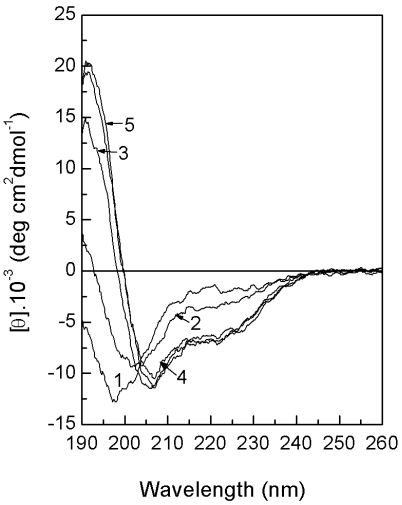

Figure 5.4. Circular dichroism spectra of B18 peptide in aqueous solution containing CTAC at concentrations of 0.0 mM (curve 1), 0.3 mM (curve 2), 1.0 mM (curve 3), 3.3 mM (curve 4) and 9.8 mM (curve 5).

Quantitative analysis showed an increase to 33–38% of α-helix content upon addition of CTAC at concentrations ranging from 1.0 to 9.8 mM (Table 5.4). The content of random coil decreased from 68% to 28%, whereas the β-sheet and β-turn did not vary significantly.

To discern the role of amphiphile charges on the peptide structure, samples of B18 in nonionic octyl β-glucopyranoside solutions were prepared. Circular dichroism measurements showed no influence of the nonionic amphiphile on B18 structure at concentrations

Conc. (mM)	Helix (%)	Strand (%)	Turn (%)	Unordered (%)
0.0	3	19	10	68
0.3	8	24	15	53
1.0	33	22	18	27
3.3	35	21	17	27
9.8	38	16	18	28

Table 5.4. Secondary structure estimation of B18 peptide in CTAC solutions by the CONTIN/LL program ($\pm$ 3%).

below the cmc (Figure 5.5, curves 2 and 3). However, at micellar concentrations, the circular dichroism spectra of B18 changed compared with the spectrum of the peptide in absence of the amphiphile (Figure 5.5, curves 4 and 5). A small positive band at 190 nm and small negative bands at 208 and 222 nm were observed for B18 in the presence of nonionic micelles. The changes were more pronounced at concentrations much above the cmc. An isosbestic point is observed at 203 nm indicating that the transition occurs mainly between two states, random coil and α-helix.

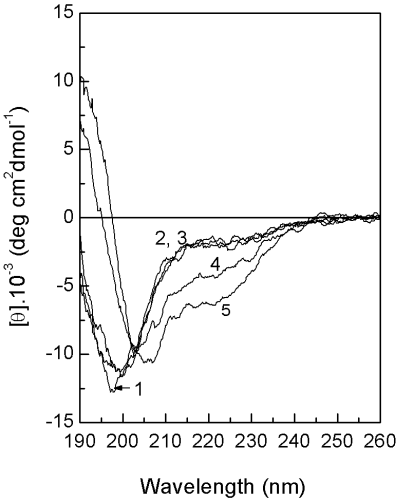

Figure 5.5. Circular dichroism spectra of B18 peptide in aqueous solution containing octyl β-glucopyranoside at concentrations of 0.0 mM (curve 1), 4.0 mM (curve 2), 12.0 mM (curve 3), 40.0 mM (curve 4) and 120.0 mM (curve 5). Curve 2 and 3 overlap.

Secondary structures estimation indicated that the content of α-helix increased from 3% to 21% upon addition of octyl β-glucopyranoside micelles, whereas the random coil content decreased from 68% to 41% (Table 5.5). The β-sheet and β-turn contents remained aproximately constant.

B18 peptide is positively charged at pH 7. Since the C-terminus of B18 is blocked

Conc. (mM)	Helix (%)	Strand (%)	Turn (%)	Unordered (%)
0.0	3	19	10	68
4.0	3	20	9	68
12.0	3	21	10	66
40.0	11	25	17	47
120.0	21	20	18	41

Table 5.5. Secondary structure estimation of B18 peptide in octyl β-glucopyranoside solutions by the CONTIN/LL program ($\pm$ 3%).

with an amide group, due to the synthesis, there are no negatively charged groups on the molecule. Both anionic and cationic amphiphiles were found to induce α-helix structure on B18 peptide at monomeric concentrations. These results suggest that the helical state of the peptide is not determined by electrostatic interactions but rather by hydrophobic interactions between amphiphiles' chains and hydrophobic residues of B18. Since non-ionic amphiphile monomers have no influence on the B18 structure it is assumed that the length of the hydrophobic chain plays a certain role in the interaction of amphiphiles with B18 peptide. Octyl β-glucopyranoside and anionic perfluorinated PFOA have the shortest chain length of the amphiphiles used in this study (C_8). However, in the case of PFOA, CF_3 groups are present, resulting in high degree of hydrophobicity. Hence hydrophobic interactions between the peptide and perfluorinated amphiphile are enhanced. The cationic amphiphile on the other hand has the longest hydrophobic chain (C_{16}), which likely allows that hydrophobic interactions to overcome the electrostatic repulsion between the positively charged amphiphile and positively charged peptide, resulting in an α-helix structure. The difference observed between anionic and cationic monomers at concentration 4.7 times below the cmc might be explained by the difference in the ratio amphiphile/peptide. Since the cmc of CTAC is about 6 times lower than the cmc of anionic amphiphiles, the CTAC/peptide ratio was much lower (3) when compared with the anionic amphiphile/peptide ratio (18).

Glaser et al. [46] reported that B18 exhibits, in the presence of trifluoroethanol, two helical regions at both ends of the molecule, connected by a flexible loop distinctly bent (Figure 5.6).

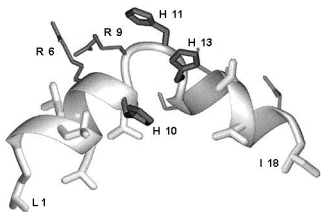

Figure 5.6. Structure of B18 peptide in 30% trifluoroethanol showing two helical regions connected by a flexible hinge in the histidine rich center. Adapted from [46].

Trifluoroethanol seems to favor the formation of α-helix mainly in the hydrophobic regions on both sides of the peptide. It is assumed that hydrophobic amphiphile chains have the same effect.

At micellar concentrations, all amphiphiles induced an α-helix structure on B18 peptide. Since there is no significant increase on the helical content in the presence of ionic micelles, the helix effect is attributed to the monomers. However, in the case of nonionic amphiphiles, the conformational transition of B18 from random coil to α-helix structure is a result of the interaction between the peptide and the micelle. Previous studies have shown that B18 peptide adopts, in the presence of zwitterionic lipid vesicles, a helix structure connected by a flexible loop, similar to that described in trifluoroethanol [45, 122]. In addition, zinc ions were found to induce an α-helical loop in the center of B18, which may act as a nucleation site for further folding [46]. It is possible that B18, in the presence of micelles, would be forced to bend due to their high degree of curvature, resulting in an α-helix structure. However, the size of the nonionic micelles might not allow the peptide to bend. This would explain the low helix content of the peptide induced by nonionic micelles. B18 was found to insert in the zwitterionic membranes in a slightly oblique orientation. The N-terminal helix of B18 was immersed into the bilayer, whereas the C-terminal was peripherally aligned and bound at the bilayer surface [122]. Likewise, in the case of nonionic micelles, B18 peptide may penetrate into the micelle core.

B18 might interact in a similar manner with anionic micelles. In this case due to the presence of negative charges, a strong electrostatic interaction will occur between the positively charged residues of B18 and the negatively charged surface of the micelle. Thus the peptide would interact in a smaller extent with the hydrophobic chains of the micelle when compared with the monomeric amphiphile. This might explain the decrease in the helix content by increasing the SDS concentrations above the cmc. In the case of perfluorinated micelles, the high hydrophobicity of the fluorinated chains likely allows that hydrophobic interaction to compensate the contribution of electrostatic attraction.

5.3 Secondary Structure of Amyloid beta-Peptide in Amphiphile Solutions

The interaction of amyloid β-peptide (1–40) with amphiphiles was studied at pH 7, with a final peptide concentration of 46 μM. In aqueous buffer, the peptide is mainly in random coil and β-sheet conformations, as determined by circular dichroism spectroscopy. The secondary structure estimation using the method CONTIN/LL resulted in a content of 3% α-helix, 34% β-sheet, 14% β-turn and 49% random coil.

It can be seen from Figure 5.7, curve 2, that at 1.7 mM of SDS, the spectrum of amyloid β-peptide is characterized by a negative band at 217 nm and a positive band at 195 nm, indicating the presence of β-sheet structure. At higher concentrations of SDS (5.0, 16.8

and 50.3 mM), the spectra exhibit characteristics of predominantly α-helix, with 2 negative bands, at 222 nm and 208 nm, and a positive band at 190 nm (Figure 5.7, curves 3 to 5). An isosbestic point between the spectrum of amyloid β-peptide in aqueous buffer and the spectra at higher SDS concentrations is observed at 202 nm, which is a strong indication of an equilibrium between two states.

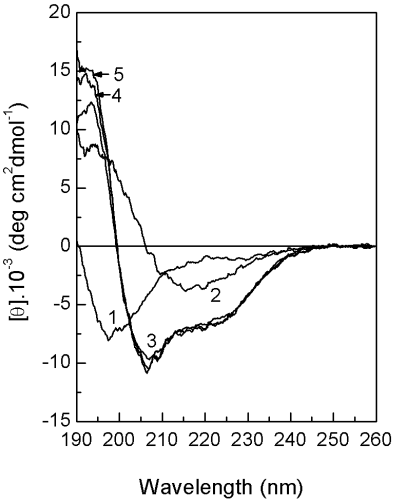

Figure 5.7. Circular dichroism spectra of amyloid β-peptide in aqueous solution containing SDS at concentrations of 0 mM (curve 1), 1.7 mM (curve 2), 5.0 mM (curve 3), 16.8 mM (curve 4) and 50.3 mM (curve 5).

Quantitative analysis of the fraction of secondary structures showed substantial 45% of β-sheet structure induced by 1.7 mM SDS, in contrast to 4% of α-helix. At higher concentrations of SDS the content of β-sheet decreased to 24% and the fraction of α-helix structure increased to 33% (Table 5.6).

Conc. (mM)	Helix (%)	Strand (%)	Turn (%)	Unordered (%)
0	3	34	14	49
1.7	4	45	21	30
5.0	30	29	15	26
16.8	32	24	20	24
50.3	33	24	19	24

Table 5.6. Secondary structure estimation of amyloid β-peptide in SDS solutions by the CONTIN/LL program ($\pm$ 3%).

Amyloid β-peptide displayed in the presence of 1.8 mM of the perfluorinated amphiphile PFOA a spectrum analogous to the spectrum in aqueous buffer (Figure 5.8, curve 2), indicating that PFOA at this concentration has no significant effect on the peptide

structure. At a concentration of 5.4 mM of PFOA, the peptide exhibited a spectrum with a small positive band at 195 nm and a small negative band at 216 nm indicating an increase in the β-sheet or β-turn contents (Figure 5.8, curve 3). The content of β-sheet and β-turn was estimated to be 38% and 21%, respectively (Table 5.7). This result is in the line with the finding that amyloid β-peptide (1–42) adopts a β-sheet structure in 10–32.5% of trifluoroethanol [111]. In contrast, at concentrations above the cmc, the perfluorinated amphiphile induced an α-helix conformation (Figure 5.8, curves 4 and 5).

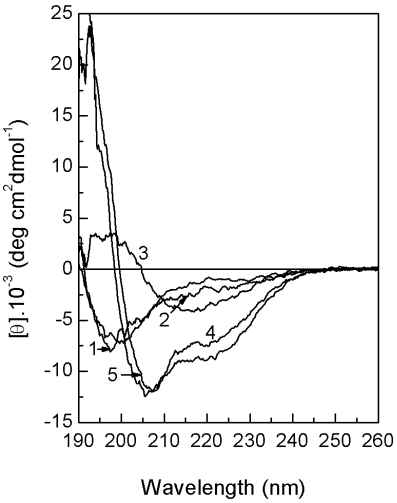

Figure 5.8. Circular dichroism spectra of amyloid β-peptide in aqueous solution containing PFOA at concentrations of 0.0 mM (curve 1), 1.8 mM (curve 2), 5.4 mM (curve 3), 18.0 mM (curve 4) and 54.0 mM (curve 5).

The content of α-helix at concentration above the cmc was above 40%. The β-sheet structure decreased to 11% and the random coil fraction decreased to 27% (Table 5.7). In this case the increase of α-helix content is due to a decrease of both random coil and β-sheet contents.

Conc. (mM)	Helix (%)	Strand (%)	Turn (%)	Unordered (%)
0.0	3	34	14	49
1.8	3	27	15	55
5.4	6	38	21	35
18.0	43	3	31	23
54.0	42	11	20	27

Table 5.7. Secondary structure estimation of amyloid β-peptide in PFOA solutions by the CONTIN/LL program ($\pm$ 3%).

The cationic amphiphile CTAC, at low concentrations (0.3 mM), induced a β-sheet

structure on amyloid β-peptide (Figure 5.9, curve 2). Increasing the concentration of the amphiphile monomers, resulted in a circular dichroism spectrum reminiscent of a mixture of structures (Figure 5.9, curve 3). In the presence of cationic micelles the peptide displayed circular dichroism spectra characteristics of α-helix structure (Figure 5.9, curves 4 and 5).

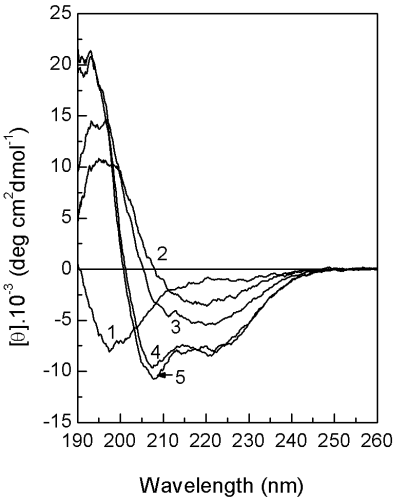

Figure 5.9. Circular dichroism spectra of amyloid β-peptide in aqueous solution containing CTAC at concentrations of 0.0 mM (curve 1), 0.3 mM (curve 2), 1.0 mM (curve 3), 3.3 mM (curve 4) and 9.8 mM (curve 5).

The secondary structure estimation showed a content of 6% α-helix, 42% β-sheet, 22% β-turn and 30% of random coil at 0.3 mM of CTAC (Table 5.8). Above the cmc, the α-helix content increased to 32%, whereas the fraction of β-sheet decreased to 18% (Table 5.8). The content of random coil remained aproximately constant at all CTAC concentrations.

Conc. (mM)	Helix (%)	Strand (%)	Turn (%)	Unordered (%)
0.0	3	34	14	49
0.3	6	42	22	30
1.0	20	34	20	26
3.3	30	20	18	32
9.8	32	18	18	32

Table 5.8. Secondary structure estimation of amyloid β-peptide in CTAC solutions by the CONTIN/LL program ($\pm$ 3%).

Figure 5.10 shows the circular dichroism spectra of amyloid β-peptide in aqueous solution of octyl β-glucopyranoside. At concentrations below the cmc, the spectra showed

the same feature as in the absence of amphiphiles, indicating that monomers of nonionic amphiphile have no significant influence on amyloid β-peptide structure. However, at concentrations above the cmc, the spectra showed a negative band at 216 nm and a sharp positive band at around 195 nm, characteristic of β-sheet conformation. The β-sheet structure might be twisted since the spectrum has the $\pi\pi^*$ band near 195 nm much stronger than the $n\pi^*$ band [74]. Further increase of nonionic micelle concentration resulted in a small increase of the band intensities with a red shift. This might be due to either an increase of β-turn content (type II has a spectrum similar to the β-sheet shifted to the red) or an increase of the number of strands. The position of the $\pi\pi^*$ absorption band depends on the width of the sheet, strongly shifted to the blue in single or double strand sheet, but shifting to longer wavelengths with increasing number of strands [74]. Since the shift is observed mainly for the positive band near 195 nm, it is most likely that increasing the micelle concentration leads to an increase of the number of strands.

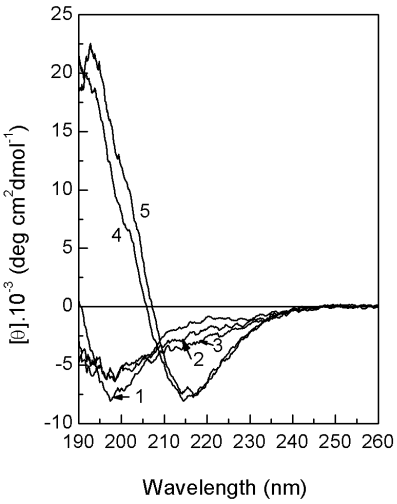

Figure 5.10. Circular dichroism spectra of amyloid β-peptide in aqueous solution containing octyl β-glucopyranoside at concentrations of 0.0 mM (curve 1), 4.0 mM (curve 2), 12.0 mM (curve 3), 40.0 mM (curve 4) and 120 mM (curve 5).

The β-sheet and β-turn contents at concentrations above the cmc were estimated to be around 50% and 20%, respectively (Table 5.9). The random coil content decreased to 23%.

Structure prediction studies of amyloid β-peptide indicate that the C-terminus, from residue 28, has a high probability for β-sheet structure (Figure 5.11) [30]. This domain shows as well a tendency to form α-helix structure. The same is observed for the residues 9–21. Two β-turns are predicted between residues 5 and 8, and residues 23 and 27. As a consequence the two domains, residues 17–21 and 28–40, may adopt both α-helix and

Conc. (mM)	Helix (%)	Strand (%)	Turn (%)	Unordered (%)
0.0	3	34	14	49
4.0	2	27	16	55
12.0	3	27	16	54
40.0	5	51	20	24
120.0	5	52	20	23

Table 5.9. Secondary structure estimation of amyloid β-peptide in octyl β-glucopyranoside solutions by the CONTIN/LL program ($\pm$ 3%).

β-sheet conformation depending on environmental effects.

In aqueous solutions, the peptide aggregation is affected by the pH and hydrophobic packing. At pH 4–7, the glutamic acid (E) and aspartic acid (D) residues ($pK_a = 4.5$) are negatively charged (residues 1, 3, 7, 11, 22, 23), the lysine, arginine ($pK_a = 10$) and histidine (H, $pK_a = 6.5$) residues are positively charged (residues 5, 6, 13, 14, 16, 28), stabilizing the aggregated β-sheet by intermolecular ion-pairing interactions [69,70,104]. In addition hydrophobic contacts developed by rearrangement of the peptide stabilize the peptide aggregates [67, 68]. At pH 7, partial deprotonation of histidine residues may occur. Regardless of this fact the peptide still forms aggregated β-structure. Only at pH below 4, at which there are six positively charged residues, and above 10, at which there are seven negatively charged residues, the ion-pairing formation is prevented, resulting in random coil conformation.

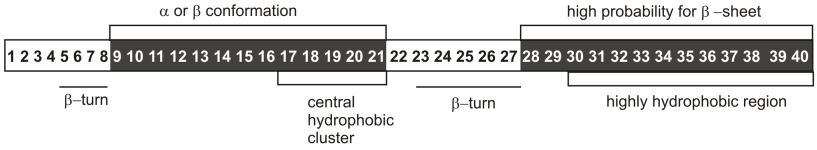

Figure 5.11. Schematic representation of amyloid β-peptide showing clusters of hydrophobic residues and structure prediction which suggests regions with a high propensity for β-sheet structure. Adapted from [30].

In solutions of ionic amphiphile monomers the structure of amyloid β-peptide (1–40) depends on the concentration of the amphiphile. SDS monomers induce β-sheet structure at concentrations 4.7 times below the cmc, whereas at higher concentrations (1.6 times below the cmc), an α-helix structure is observed. A similar effect is observed for cationic amphiphile monomers but at higher concentrations (1.4 times below the cmc) the α-helix content is much lower. Perfluorinated monomers have a small effect on the peptide structure at low concentrations whereas a β-sheet structure is induced at higher concentrations (1.7 times below the cmc). Nonionic amphiphile monomers have no significant influence on the peptide structure. The ionic amphiphiles used show longer hydrophobic chains than the nonionic amphiphile (shorter chain length), and most likely the stabilization of

β-sheet structure by ionic monomers results from hydrophobic interactions. The fact that ionic monomers can induce α-helix structures at concentrations close to the cmc might be due to the presence of pre-micellar aggregates or to a shift of the cmc of the amphiphile caused by the peptide.

Above the cmc both cationic and anionic amphiphiles induce an α-helix structure on amyloid β-peptide, whereas the nonionic amphiphile induces a β-sheet structure. The α-helix inducing effect of charged micelles, in contrast to the stabilization of β-sheet structure by nonionic micelles, is largely attributed to electrostatic interactions. The highly charged environment around the micelle prevents the intermolecular ion pairing and favors the electrostatic interaction between the peptide and the micelle. Nuclear magnetic resonance studies have shown that the pK_a values of the residues E, D, H of amyloid β-peptide (1–28) in SDS micelle solution were significantly higher by 1.1–1.6 units relative to the free amino acids in SDS or to the peptide in D_2O [104]. A similar trend was observed for residues E22 and D23 of amyloid β-peptide (1–40) in SDS solution [114]. This large increase was partially attributed to electrostatic contributions. In contrast, the pK_a values of amyloid β-peptide (1–28) residues in zwitterionic dodecylphosphocholine micelle solution were nearly identical to the values obtained in D_2O [104]. Hence, the pK_a values of the peptide are assumed not to vary significantly in the presence of octyl β-glucopyranoside micelles. In the case of nonionic micelles the intermolecular ion-pairing are not prevented. The β-sheet structure is likely induced through hydrogen bonds between the peptide and the micelle. A molecular interaction model between amyloid β-peptide and micelles is proposed in Figure 5.12.

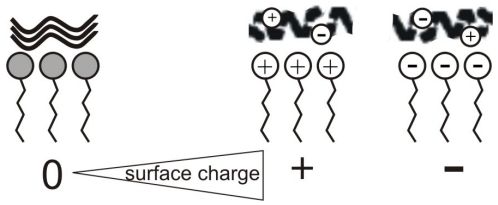

Figure 5.12. Schematic model for amyloid β-peptide (1–40) interactions with micelles. The peptide interacts with nonionic micelles through hydrogen bonds, resulting in β-sheet structure. When the micelle exhibits a charged surface, electrostatic interactions between the peptide and the micelle occur, resulting in α-helix structure.

According to the calculated α-helix content of amyloid β-peptide (1–40) in aqueous charged micelle solutions, it is possible to estimate that in SDS and CTAC solutions 13 residues of the peptide constitute the α-helix structure, whereas in PFOA solutions 17 residues are involved. This estimation is consistent with the predicted α-helix structure in solutions of charged micelles, considering that at pH 7 the helical domain of residues 15–24 can be less structured [110, 113–115]. The structure of amyloid β-peptide (1–40)

in SDS micelle solution was described to consist of two helical regions, residues 15–24 and residues 28–36, separated by a looped region (residues 25–27) [114, 115]. The helicity of the region 15–24 was found to be selectively sensitive to pH. Above pH 6, part of this helix was less structured. Likewise, the structure of the short fragment amyloid β-peptide (1–28) in charged micelle solutions or trifluoroethanol solution was described to be strongly dependent on the pH [113]. Two helical regions were observed at low pH and at high pH for negatively and positively charged micelles, respectively, whereas at pH 4–8, only one helical region was detected. Below pH 3, in 60% trifluoroethanol, the peptide adopted a complete α-helix structure, while above pH 7, the first nine N-terminal residues unfolded, leaving an α-helix at residues 10–27 [110].

Penetration of amyloid β-peptide (1–40) into the charged micelles is possible to occur. The C-terminal part of the peptide is reported to possess fusion properties. Studies with the short segment amyloid β-peptide (25–35) have shown that the C-terminal 32–35 was inserted in SDS micelles [112]. Moreover, amyloid β-peptide is reported to insert in lipid membranes by its C-terminus [123, 124]. Higher α-helix content was observed when the peptide was incorporated into acidic lipids [124]. The hydrophobic domain appeared to be completely buried between the lipid acyl chains, which was attributed to the surface charge density of the membrane. In the case of neutral membranes only a partial burial of the hydrophobic part of the peptide and a high β-sheet content were observed [124]. Likewise, insertion of amyloid β-peptide (1–40) into nonionic octyl glucoside micelles is expected to occur in very low extent or not occur at all.

5.4 Structure Stabilization by Amphiphiles

The effect of amphiphiles on the secondary structure of self-assembled peptides may have two distinct implications. On one hand it is possible to extrapolate the *in vitro* studies of the interaction of amphiphiles with peptides to the *in vivo* environment. SDS micelles readily mimic biological membrane interfaces and the lipid part of lipoproteins [125, 126]. Octyl glucoside molecules form micelles with a polar surface made up of glucose head groups, which can mimic the glycoprotein or glycolipid covered regions of the membrane surface.

The results reported in section 5.2 indicate that B18 exhibits a preferential α-helix structure in ionic and nonionic micelle solutions, suggesting that the peptide at a concentration of 96 μM and pH 7 may adopt a similar structure in the presence of ionic and zwitterionic membranes. Hydrophobic interaction and electrostatic attraction between charged residues (often positively) and negatively charged lipids are involved in most peptide or protein/lipid binding processes [127, 128]. This study strongly suggests that primary hydrophobic interactions are essential for driving B18 to interact with membranes and that electrostatic interaction may affect peptide insertion.

As described in section 5.3, amyloid β-peptide (1–40) adopts a preferential α-helix structure in the presence of ionic micelles, whereas a β-sheet structure is formed in nonionic micelle solution. This suggests that amyloid β-peptide would adopt an α-helix structure upon interaction with a charged biological membrane and a β-sheet structure when interacting with zwitterionic membranes. In this case the results suggest that electrostatic attraction provided by ionic amphiphiles is essential for driving the amyloid β-peptide to the membrane surface, and subsequent hydrophobic interactions with the chains may stabilize the peptide-membrane interaction and influence the insertion of the peptide. In the case of nonionic micelles the absence of charges associated with the glucose head group are thought to be a barrier to a possible insertion of the peptide in the hydrophobic core of the micelle, leading to an accumulation and aggregation of the peptide on the micelle surface. The formation of β-sheet and subsequent aggregation of amyloid β-peptide into fibrils may well occur at surfaces of membranes containing glycolipids.

Most importantly, the results presented in the previous sections demonstrate that macromolecules with positively and negatively charged surfaces stabilize the α-helix structure. This structure is monomeric and stable, constituting an appropriate target for the design of inhibitors of amyloid fibril formation. The most efficient α-helix inducing charged micelles were composed of perfluorinated chains and negatively charged head groups.

6 Influence of Nano-Engineered Particles on the Secondary Structure of Self-Assembled Peptides

Fluorinated alcohols, such as trifluoroethanol, are able to convert β-sheet into α-helix conformation in amyloid β-peptide at physiological pH of 7.4 [129]. This effect, however, is not observed for their hydrogenated analogues. Fluorinated alcohols are, however, not biocompatible and therefore have no therapeutic relevance *in vivo*.

Charged micelles were observed to induce α-helix structure in B18 and amyloid β-peptide and the higher helical content was attained with charged perfluorinated micelles, as described in chapter 5. Based on these findings, polyelectrolyte-fluorosurfactant complexes were prepared, since it is expected that combining highly charged polymers and fluorinated compounds will enhance the α-helix inducing effect [130]. It has been previously demonstrated that polyelectrolyte-fluorosurfactant complexes are able to dissolve amyloid plaques in sections of animal tissue [131] and to convert β-sheet into α-helix structures [129]. These complexes were in a first approach tested on solid supports. In order to increase the contact area between peptide molecules and complexes, nanoparticles of these complexes were synthesized [130].

Polyelectrolyte-fluorosurfactant complexes can be, in principle, engineered with biocompatible properties [131]. Generally, perfluorinated hydrocarbons are considered to be metabolically inert and non-toxic [132]. However, perfluorinated fatty acids, such as perfluorooctanoic and perfluorodecanoic acids, were shown to be peroxisome proliferators which are known to be carcinogenic [133]. A causal link between an increase in the oxidative stress by peroxisomes and tumor promotion has been proposed to explain the hepatocarcinogenicity of these compounds. Additionally they were found to be involved in down-regulation of gap junctional intercellular communication (exchange process of small molecules and ions between cells through proteinaceous channels), which has also been linked to the tumor promoting properties of many carcinogens [134]. Perfluorinated fatty acids were not cytotoxic up to a dose of 400 μM, but still they could alter the gap junctional intercellular communication. These effects, however, seem to be dependent on the chain length of the fluorinated tail and only perfluorinated fatty acids with 7–10 carbons inhibited this biological process [134].

The polyelectrolyte-fluorosurfactant complexes were prepared with fluorinated chains of 12 carbons. By preparing this type of nanoparticles it is expected that the concentration of perfluorinated amphiphiles will be low enough to be in the range of non-toxic doses.

The influence of the nanoparticles on B18 and amyloid β-peptide was characterized by circular dichroism spectroscopy. Both hydrogenated and fluorinated complexes were used in order to discern their influence on the peptide structure.

6.1 Nanoparticle Characterization

Polyampholytes with alternating cationic N,N'-diallyl-N,N'-dimethylammonium chloride monomer and anionic maleamic acid (P_1) or N-phenylmaleamic acid (P_2) monomers, were synthesized with a degree of polymerization in the range of 60 to 80. The polyampholytes were complexed with dodecanoic and perfluorododecanoic acid, in order to obtain hydrogenated (PH) and fluorinated (PF) complexes, respectively. This results, in both cases, in nanoparticles, so-called polyampholyte dressed micelles [130]. The chemical structure of the nanoparticles is shown in Figure 6.1.

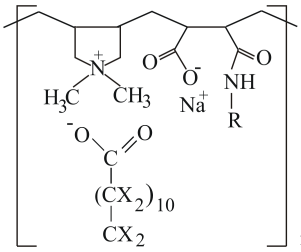

	X = H	X = F
R = H	P_1H	P_1F
R = C_6H_5	P_2H	P_2F

Figure 6.1. Chemical structure of the complexes of polyampholytes with dodecanoic acid (P_1H and P_2H) and perfluorododecanoic acid (P_1F and P_2F).

In the following sections the principal methods and results of characterization of the nanoparticles will be described.

6.1.1 Dynamic Light Scattering

Dynamic light scattering, also referred to as quasi-elastic light scattering, enables the determination of particle size and size distribution in dispersion. The method is based on the fluctuations in the intensity of light scattered by a small volume of a solution in the microsecond time range which are directly related to the Brownian motion of the solute. Submicrometer size particles in suspension exhibit significant random motion because of collisions with the molecules of the surrounding liquid medium (Brownian motion). As a result, when light irradiates a colloidal dispersion, the phases of the scattered waves fluctuate randomly in time. The scattered light intensities from individual particles interfere

with each other, and hence the net intensity of the scattered light fluctuates randomly in time. The time dependence of the intensity fluctuations, calculated from the autocorrelation function of the scattered intensity, can be related to the diffusion coefficient of the particles. For a monodisperse system, the normalized autocorrelation function, $g^{(1)}$, is an exponential decay,

$$g^{(1)}(t') = \exp(-\Gamma t'), \tag{6.1}$$

where t' is the decay time of the autocorrelation function, Γ is the decay constant, which is related to the diffusion coefficient D by

$$D = \frac{\Gamma}{q^2}, \tag{6.2}$$

where q is the scattering wave vector, which depends on the wavelength of the light source, λ, the solvent refractive index, n, and the angle of detection, θ,

$$q = \frac{4n\pi}{\lambda} \sin\frac{\theta}{2}. \tag{6.3}$$

The hydrodynamic averaged intensity radius of the particles, R_H, can be calculated from the diffusion coefficient D, using the Stokes-Einstein relation

$$R_H = \frac{k_B T}{6\pi\eta D}, \tag{6.4}$$

where k_B is the Boltzmann constant, T the absolute temperature and η is the viscosity of the medium. This relation is the basis of the particle size determination by dynamic light scattering, but it is valid only for monodisperse particles.

For polydisperse particles, the normalized autocorrelation function is an integral of exponentials,

$$g^{(1)}(t') = \int_0^\infty F(\Gamma)\exp(-\Gamma t')d\Gamma. \tag{6.5}$$

Dynamic light scattering measurements of the nanoparticles were performed using a fixed angle (173°) ALV-NIBS high performance particle sizer. The size of the hydrogenated and fluorinated nanoparticles were of the same order of magnitude. The measurements revealed sizes of 3.1 ± 0.3 nm (P_1F) and 3.2 ± 0.3 nm (P_2F) for the fluorinated complexes. The mean diameters of the hydrogenated particles spread over a broader range, 2–4 nm for P_1H and approximately 3 nm for P_2H.

In contrast to their complexes, the dynamic light scattering data of the neat polyampholytes indicated only scattering objects with hydrodynamic radii smaller than 1.5 nm.

6.1.2 Analytical Ultracentrifugation

Analytical ultracentrifugation is one of the most reliable experimental methods for the determination of particle size distribution. The technique consists in monitoring the sedimentation of particles in the centrifugal field. The application of a centrifugal force causes

the depletion of particles at the meniscus and the formation of a concentration boundary that moves toward the bottom of the centrifuge cell as a function of time. The definition of the sedimentation coefficient of a particle, s, and the molecular parameters that determine the s-value are given by the Svedberg equation

$$s = \frac{u}{\omega^2 r} = \frac{M(1-\overline{\nu}\rho)}{N_A f} = \frac{MD(1-\overline{\nu}\rho)}{RT}, \tag{6.6}$$

where u is the observed radial velocity of the particle, ω is the angular velocity of the rotor, r is the radial position, $\omega^2 r$ is the centrifugal field, M is the molar mass, $\overline{\nu}$ is the partial specific volume, ρ is the density of the solvent, N_A is Avogadro's number, f is the frictional coefficient, D is the diffusion coefficient, and R is the gas constant.

Analytical ultracentrifugation of the nanoparticles was carried out using a Beckman Optima XL-I ultracentrifuge (Beckman Counter, Palo Alto, CA) at (25 $\pm$ 0.2)°C and 50000 rpm (acceleration 180000 g). Detection of the particles was carried out by applying UV-Vis absorption detection at a wavelength of 210 nm (P_1) and 240 nm (P_2). They were simultaneously detected with the Raleigh interference optics. The measured radial concentration profiles were transformed into a sedimentation coefficient distribution by using the equation

$$s_i = \frac{\ln(r_i/r_m)}{\omega^2 t}, \tag{6.7}$$

where s_i is the sedimentation coefficient of i, r is the radial distance to the center of rotation with the indices i = particle, m = meniscus and t is the time. The particle-size distribution was determined by

$$d_i = \sqrt{\frac{18\eta s_i}{\rho_1 - \rho_2}}, \tag{6.8}$$

where d_i is the diameter of the particle i, η the solvent viscosity and ρ the density with the indices 1 for water and 2 for the particle. The sedimentation coefficient distribution (equation (6.7)) is calculated for a constant velocity of the particles where the centrifugal force acting on the particles is balanced by the frictional and buoyant forces. The validity of this assumption was checked by equal spacings between the individual scans. Equation (6.8) implies Stokes' law meaning that the particles must be spherical. If this is not the case, the diameter is that of an equivalent sphere.

Figure 6.2 shows the particle size distribution of the polyampholyte complexes as determined by analytical ultracentrifugation. The fluorinated nanoparticles are nearly of the same size and their size distributions are narrow. The mean diameters were quantified by Gaussian fits to be 5.1 $\pm$ 0.1 nm (P_1F) and 3.9 $\pm$ 0.1 nm (P_2F). For hydrogenated nanoparticles mean diameters of 2.7 $\pm$ 0.1 nm (P_1H) and 3.9 $\pm$ 0.1 nm (P_2H) were found. The strong increase in the relative concentrations at diameters smaller than 1 nm is probably due to non-complexed polyampholyte chains and has not be taken into account for

fitting. No sedimenting objects with sizes significantly larger than 1 nm were present for the neat polyampholytes. Thus aggregation of the neat polyampholytes can be ruled out.

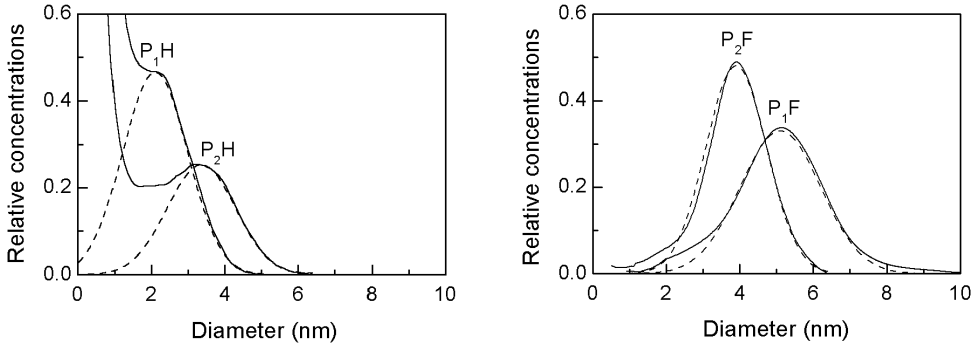

Figure 6.2. Particle size distributions of the polyampholyte complexes with dodecanoic (PH) and perfluorododecanoic acid (PF) as determined by analytical ultracentrifugation. Dashed lines correspond to the Gaussian fits. The concentrations were 1 g L^{-1}. Adapted from [130].

The critical aggregation concentrations of the complexes depend on the polyampholyte and are higher for the complexes with $R =$ hydrogen (P_1). The values were 1 g L^{-1} for P_1F and P_1H and 10^{-2} g L^{-1} for P_2F and P_2H. Above these values, the particles were proved to be stable in a large range of concentrations in the sense that they were not aggregated or dissolved at higher and lower concentrations, respectively. An example is shown for the P_2F complex in Figure 6.3.

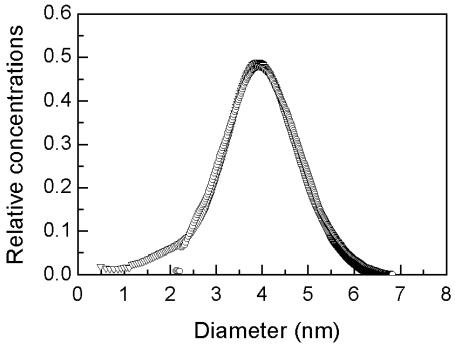

Figure 6.3. Particle size distributions of the fluorinated complex P_2F at concentrations of 0.02 (○) and 2 (▽) g L^{-1} as determined by analytical ultracentrifugation. Adapted from [130].

6.1.3 Zeta Potential

The zeta potential is related to the electric charge of a particle. The net charge density on a particle in contact with an aqueous solution gives rise to an electrical double layer,

comprised of a fixed layer which includes strongly adsorbed counterions at specific sites on the surface and a outer, diffuse layer composed of counterions whose distribution is determined by a balance of electrostatic forces and random thermal motion. In the presence of an applied electric field, each particle (and strongly adsorbed ions) moves with respect to the medium. Between the two phases is a plane of shear, i.e. the hypothetical boundary between the particle with its ion atmosphere and the surrounding medium. The electric potential at the plane of shear is called zeta potential.

The zeta potentials of dispersed colloidal particles can be measured by electrophoresis. The electric force causes the particle to move in relation to a stationary liquid at a constant velocity. The ratio of the velocity to the electric field E is the electrophoretic mobility, μ_E. Electrophoretic mobilities of nanoparticles were measured using a Malvern Zetamaster. The mobility was converted into zeta potential, ζ, using the Smoluchowski equation

$$\zeta = \frac{\eta \mu_E}{\varepsilon}, \tag{6.9}$$

where η is the viscosity of the solution and ε is the permittivity of the solution.

Zeta potentials were highly negative for fluorinated complexes, with values of $-(47 \pm 5)$ mV for P_1F and $-(48 \pm 5)$ mV for P_2F (Figure 6.4). The differences in the zeta potentials of hydrogenated complexes were more pronounced. They displayed zeta potentials of $+(25 \pm 10)$ mV when R is the hydrogen and $-(20 \pm 4)$ mV when R is the phenyl group (Figure 6.4). The reason for the positive value of zeta potential of P_1H might be amine protonation.

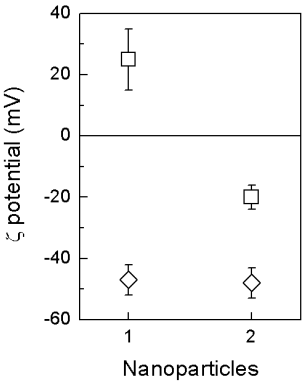

Figure 6.4. Zeta potentials of the polyampholytes complexes with dodecanoic acid (□) and perfluorododecanoic acid (◇). Adapted from [130].

6.1.4 Density

The density of the nanoparticles was determined with a density oscillator model DMA 60/602 (Anton Paar, Graz). The densities of the fluorinated complexes were drastically

higher, 1.654 (P_1F) and 1.754 (P_2F) g cm^{-1}, than those of the non-fluorinated, 1.256 (P_1H) and 1.273 (P_2H) g cm^{-1}.

6.1.5 Small Angle X-Ray Scattering

X-ray diffraction in the small-angle mode is used for the characterization of colloidal systems with characteristic length scales that range from 1 nm to several hundred nanometers. This technique measures the diffracted X-ray intensity in the range of 0 to 5°. When a beam of monochromatic X-ray radiation is directed at a colloidal system, diffraction of the X-rays at various angles with respect to the incident beam is observed. The scattering intensities are given as a function of the scattering vector which is defined here as $s = q/2\pi = (2/\lambda)\sin\theta$, where θ is the Bragg angle and λ is the wavelength of the X-ray radiation (1.54 Å).

Radii of the nanoparticles were determined by small-angle X-ray scattering (HASYLAB at DESY, Hamburg, Germany). Dispersions of nanoparticles in water were transferred into glass capillaries with a diameter of 1 mm. The intensity measured was corrected by the intensity from a capillary filled with Millipore water. The fluorinated nanoparticles produce a strong scattering intensity (Figure 6.5 (a)) while the intensity of the hydrogenated nanoparticles is low (not shown). This difference can be explained by the different densities of the nanoparticles. Taking into account that the small-angle scattering intensity is proportional to the square of the electron density difference between the particles and their surroundings (water) the scattering intensity of the fluorinated particles has to be expected one order of magnitude higher than its hydrogenated analogues. On the basis of the present data only the scattering of the fluorinated nanoparticles can therefore be evaluated. Figure 6.5 shows that the scattering intensity decreases proportional to s^{-4} at high values of s, i. e. a Porod asymptote. Sharp phase boundaries are identified by the presence of Porod's law [135] which is given by

$$\lim_{s\to\infty} 2\pi^3 s^4 I = \frac{k}{l_p}, \tag{6.10}$$

where I is the scattering intensity, l_p is the average chord length, and k is the invariant, which is given by the expression

$$k = 4\pi \int_0^\infty s^2 I(s) ds \tag{6.11}$$

The scattering intensity is experimentally available between a lower limiting value of the scattering vector s_{min} and an upper value s_{max}. In order to calculate the invariant as precisely as possible the experimental limits were taken into account by approximations of the region of high and low scattering vectors, which results in

$$k = \frac{4}{3}\pi s_{min}^3 I(s_{min}) + 4\pi \int_{s_{min}}^{s_{max}} s^2 I(s) ds + \frac{4\pi}{s_{max}} \lim_{s\to\infty}[s^4 I(s)]. \tag{6.12}$$

The area under the straight lines in Figure 6.5 (c) corresponds to the first and third term in equation (6.12) and sum up together to 30% of the invariant, which cannot be neglected. The main source of error in the range of validity covered by Porod's law is the scattering due to density fluctuations and the widths of the domain boundary [136]. The value of $s^4I(s)$, as shown in Figure 6.5 (b), was found to be constant for a scattering vector in the range of 0.15 to 0.28 nm^{-1}. This proves that the structures of the nanoparticles are consistent with Porod's law. A broader transition or a statistical structuring of the domain boundary, as typically observed in microphase-separated block-copolymers in the bulk material can be excluded [137].

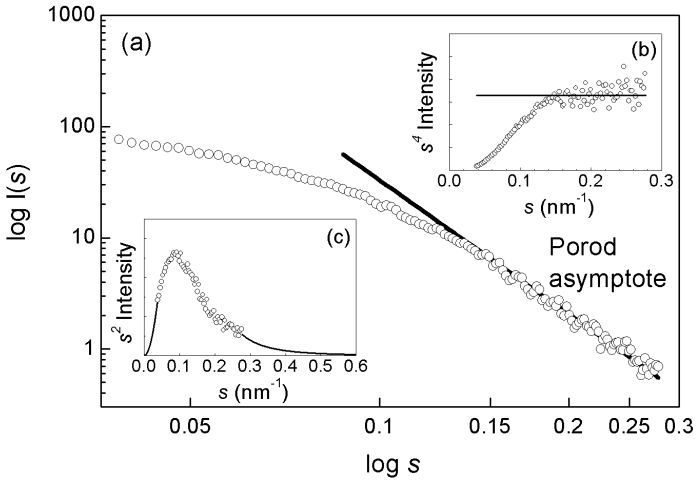

Figure 6.5. (a) Small-angle X-ray scattering intensity of the fluorinated nanoparticles (circles). The straight line indicates the Porod asymptote. The $s^4I(s) - s$ plot in insert (b) shows the asymptotic behavior of the data (circles). The solid line represents the best fit according to Porod's law performed in the range 0.15–0.28 nm^{-1}. The area under the curve in insert (c) represents the invariant k. Experimental values (circles) are only available between a lower limiting value of the scattering vector s_{min} and an upper value s_{max}. Extrapolations (straight lines) below s_{min} and above s_{max} were carried out to calculate the invariant as precisely as possible.

Small deviations from a sharp boundary would indicate a significant deviation from Porod's law [136]. Therefore the phase boundaries of the nanoparticles are of the order of 1 to 2 atomic distances. Using equation (6.10), the average chord length was calculated to be 2.7 nm. The radius of a spherical particle is then given as $r = (3/4)l_p$ [137] and was determined to be 2.0 nm for the nanoparticles. This value is in agreement with the values determined by analytical ultracentrifugation and dynamic light scattering measurements.

6.1.6 Structure of Nanoparticles

The nanoparticles are thought to consist of a hydrophobic core, which is formed by the surfactant chains, and a hydrophilic shell, like a typical surfactant micelle. The low molecular weight counterions of the micelle are replaced by the polyampholytes [130]. In the case of the nanoparticles large molecules with approximately 60–80 binding sites stick on the micelle surface instead of moving like the single charged ions. Zeta potentials indicate that the particles are stabilized ionically.

Due to their small size they have specific surface areas of approximately 1000 $m^2\ g^{-1}$. It can be expected that the high surface area would be useful in providing extensive interactions with the peptides.

6.2 The Conformation of B18 Peptide in the Presence of Nanoparticles

Circular dichroism measurements were performed to determine the secondary structure of the B18 peptide after titration with different amounts of nanoparticles. Final particle concentrations were 0, 2, 4 and 6 g L^{-1}. The measurements were performed at pH 4 and 7, at $(20 \pm 1)^{\circ}$C, with a final peptide concentration of 96 μM.

The circular dichroism spectra of B18 in the presence of complex P_1 and complex P_2 at pH 4 are shown in Figures 6.6 and 6.7, respectively. It can be seen from Figures 6.6 and 6.7, curve 1, that B18 displayed, in the absence of particles, the typical spectrum of a random coil protein (minimum at 198 nm). The quantitative determination of the secondary structure motifs, using CONTIN/LL, resulted in a content of 2% α-helix, 14% β-sheet 8% β-turn and 76% random coil at pH 4. The titration of B18 with increasing amounts of fluorinated nanoparticles at pH 4 induced a change from random coil to α-helix structure as shown in Figure 6.6 (a) and 6.7 (a) (curves 2 to 4).

Secondary structure estimation resulted in 23%, 46% and 52% of α-helix for 2, 4 and 6 g L^{-1} of fluorinated complex P_1F, respectively (Table 6.1). The fluorinated complex P_2F induced an α-helix content of 29% (2 g L^{-1}), 44% (4 g L^{-1}) and 51% (6 g L^{-1}). The β-sheet content decreased to 6–7% in the series, whereas the degree of random coil decreased to 28% for both complexes (Table 6.1). It can be seen that an isosbestic point is present at 203 nm (Figure 6.6 (a) and 6.7 (a)), which is a strong indication for an equilibrium between two states.

The hydrogenated particles, in contrast to the fluorinated ones, did not induce α-helix rich structures at pH 4 (Figure 6.6 (b) and 6.7 (b)). The titration of B18 with hydrogenated nanoparticles resulted in a decrease of the circular dichroism signal with increasing concentration of the nanoparticles (Figure 6.6 (b) and 6.7 (b), curves 2 to 4). This was accompanied by the occurrence of turbidity in the solution. The presence of an isosbestic point

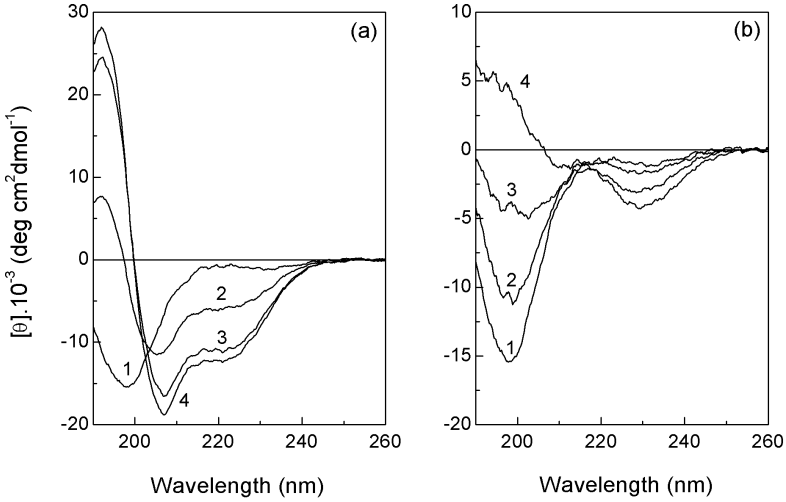

Figure 6.6. Circular dichroism spectra of B18 peptide at pH 4 in the presence of complex P_1 fluorinated (a) and hydrogenated (b): 0 g L^{-1} (curve 1), 2 g L^{-1} (curve 2), 4 g L^{-1} (curve 3) and 6 g L^{-1} (curve 4).

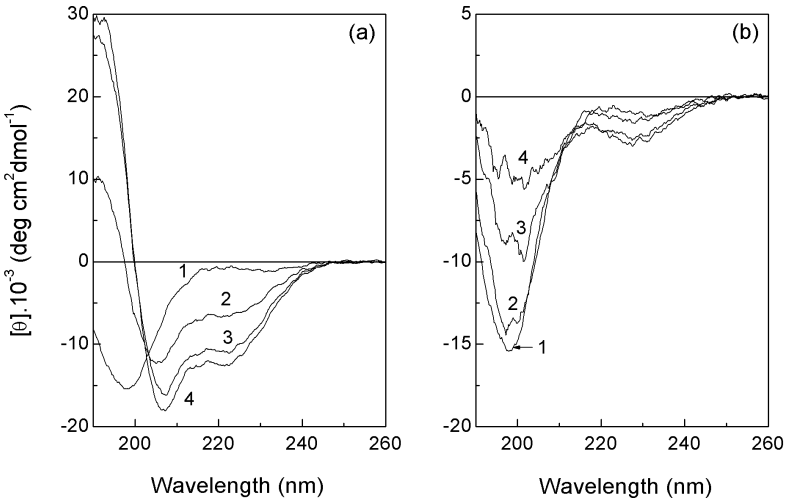

Figure 6.7. Circular dichroism spectra of B18 peptide at pH 4 in the presence of complex P_2 fluorinated (a) and hydrogenated (b): 0 g L^{-1} (curve 1), 2 g L^{-1} (curve 2), 4 g L^{-1} (curve 3) and 6 g L^{-1} (curve 4).

Complex	Conc. (g L^{-1})	Helix (%)	Strand (%)	Turn (%)	Unordered (%)
–	0	2	14	8	76
P_1F	2	23	18	18	41
	4	46	9	15	30
	6	52	6	14	28
P_2F	2	29	18	23	30
	4	44	10	15	31
	6	51	7	14	28

Table 6.1. Percentage of secondary structure motifs ($\pm$ 3%) of B18 in the presence of fluorinated nanoparticles at different particle concentrations and pH 4 calculated by CONTIN/LL program.

at 210 nm indicates a two-state transition from random coil to a β-sheet rich structure. This suggests that β-sheet structures are present in B18 for the higher particle concentration (4 and 6 g L^{-1}), but due to the strong light scattering of the B18 aggregates the distribution of structure motifs could not be calculated. A possible reason for the occurrence of aggregates in the case of the hydrogenated particles can be charge compensation between the negatively charged nanoparticles and the positively charged B18.

The changes in the secondary structure of B18 at pH 7 after titration with nanoparticles are shown in Figures 6.8 and 6.9. At pH 7, B18 peptide exhibited, in the absence of particles, the characteristic spectrum of a random coil protein, similar to that observed at pH 4 (Figures 6.8 and 6.9, curve 1). Quantitative determination of the secondary structure indicated a content of 3% α-helix, 19% β-sheet, 9% β-turn and 69% random coil at pH 7. Again a transition from random coil to α-helix structure after titration with the fluorinated nanoparticles was observed, but the behavior was more complex. It can be seen in Figure 6.8 that P_1F complex induced the maximum degree of α-helix at a concentration of 4 g L^{-1}. The α-helix content at this concentration was estimated to be 43%. The random coil fraction decreased from 69% to 31% and the β-sheet and β-turn contents were 11% and 15%, respectively. A further increase of the nanoparticle concentration did not result in a higher content of α-helix (Figure 6.8, curves 2 to 4).

In the presence of P_2F complex, the circular dichroism signal intensity of B18 was close to zero at small nanoparticle concentrations (2 g L^{-1}) and a high turbidity in the solution was observed (Figure 6.9 (a), curve 2). This was probably due to charge neutralization between B18 and the particles. At higher nanoparticle concentrations the solutions were transparent and the shapes of the circular dichroism curves were that of typical α-helix structure (curves 3 and 4 in Figure 6.9 (a)). These findings are in the line with results reported earlier by Glaser et al., who showed that at pH 7 the titration of B18 with increasing amounts of trifluoroethanol induced a change from random coil to α-helix, but an intermediate state appeared to exist at 10–20% of alcohol [46].

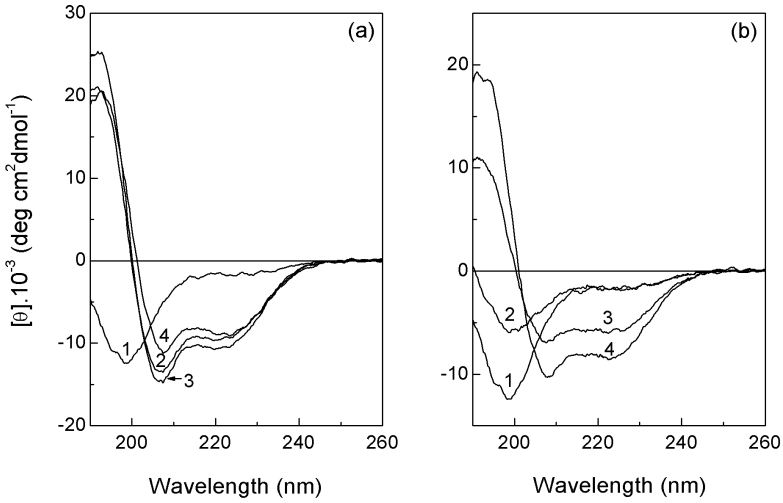

Figure 6.8. Circular dichroism spectra of B18 peptide at pH 7 in the presence of complex P_1 fluorinated (a) and hydrogenated (b): 0 g L^{-1} (curve 1), 2 g L^{-1} (curve 2), 4 g L^{-1} (curve 3) and 6 g L^{-1} (curve 4).

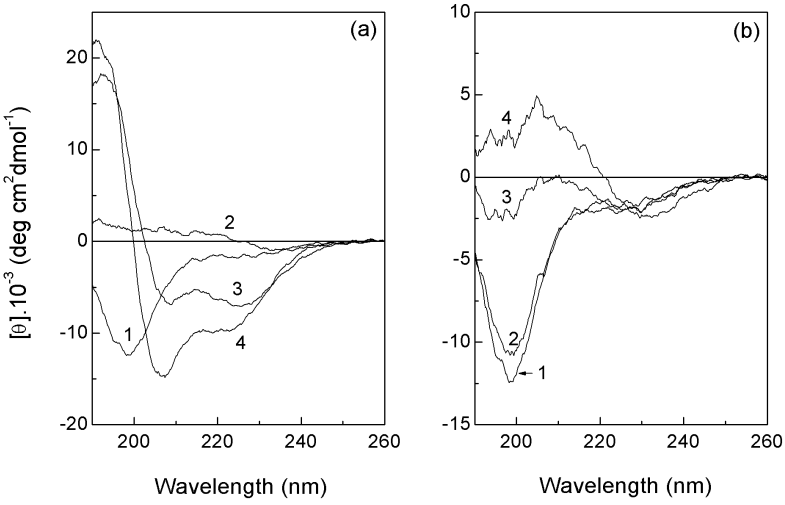

Figure 6.9. Circular dichroism spectra of B18 peptide at pH 7 in the presence of complex P_2 fluorinated (a) and hydrogenated (b): 0 g L^{-1} (curve 1), 2 g L^{-1} (curve 2), 4 g L^{-1} (curve 3) and 6 g L^{-1} (curve 4).

The content of α-helix was estimated to be 31% and 40% for P_2F complex concentrations of 4 and 6 g L^{-1}, respectively (Table 6.2).

Conc. (g L^{-1})	Helix (%)	Strand (%)	Turn (%)	Unordered (%)
0	3	19	9	69
2	[a]	[a]	[a]	[a]
4	31	18	17	34
6	40	11	17	32

[a] calculation was not possible due to precipitation

Table 6.2. Percentage of secondary structure motifs ($\pm$ 3%) of B18 in the presence of fluorinated nanoparticles P_2F at different particle concentrations and pH 7 calculated by CONTIN/LL program.

The effect of P_2F at a concentration of 6 g L^{-1} on B18 peptide is similar to that observed for P_1F complex at 4 g L^{-1} (Figure 6.10). The particle/peptide ratio was estimated to be 0.6 for P_1F at 4 g L^{-1} and 2 for P_2F at 6 g L^{-1}. The number of nanoparticles was estimated assuming a spherical shape and a homogeneous density of each particle. The total number of particles is given by the mass of the solution in 1 L divided by the mass of a single particle, which is equal to the volume ($(4/3)\pi r^3$, where r is the radius of the particle) multiplied by the density. The results suggest that at pH 7, P_1F complex is more effective in inducing α-helix structure in B18 than P_2F complex.

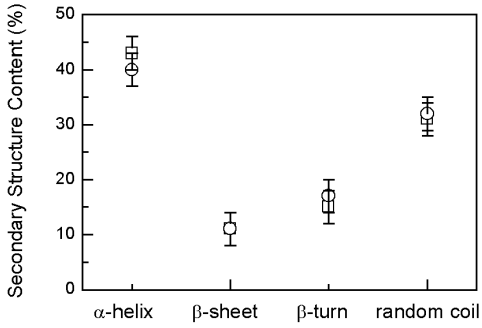

Figure 6.10. Percentage of the secondary structure elements of B18 in the presence of fluorinated particles at pH 7: 4 g L^{-1} of P_1F (□) and 6 g L^{-1} of P_2F (○).

Binder et al. reported that zinc ions induce α-helix structure in B18 by specific complexation with the histidine-rich sequence of B18 (HxxHH) [45]. In the absence of zinc, the peptide is rapidly inactivated at pH $\geq$ 7 or higher by aggregation into β-sheet amyloid fibrils. The fluorinated particles at a suitable concentration seem to have a similar effect on B18 as zinc or α-helix inducing solvents (trifluoroethanol).

The effect of hydrogenated nanoparticles on B18 peptide at pH 7 depends on the polyampholyte (Figure 6.8 (b) and 6.9 (b)). The hydrogenated complex P_1H induced

a decrease in the circular dichroism signal of B18 at a concentration of 2 g L^{-1}, indicating the presence of aggregates. At higher concentrations of P_1H complex (4 and 6 g L^{-1}), spectra characteristic of α-helix structure were observed. Quantitative analysis of the structure motifs resulted in an α-helix content of 3%, 23% and 33% for 2, 4 and 6 g L^{-1} P_1H nanoparticles, respectively. The degree of random coil decreased to 32%, whereas the β-sheet content was 17%, similar to the value obtained for B18 in the absence of nanoparticles. The increase in α-helix was more due to a reduction of the random coil content (from 69% to 32%) than to the reduction of the β-sheet content (from 19% to 17%). Further increasing the nanoparticle concentration did not change the secondary structure contents.

As opposed to P_1F, the hydrogenated complex P_1H is not able to decrease the β-sheet content of B18 (Figure 6.11). The maximum α-helix inducing effect of P_1H was observed at a concentration of 6 g L^{-1} (particle/peptide ratio of 8), whereas that of the fluorinated P_1F complex was found at 4 g L^{-1} (particle/peptide ratio of 0.6), as shown in Figure 6.11.

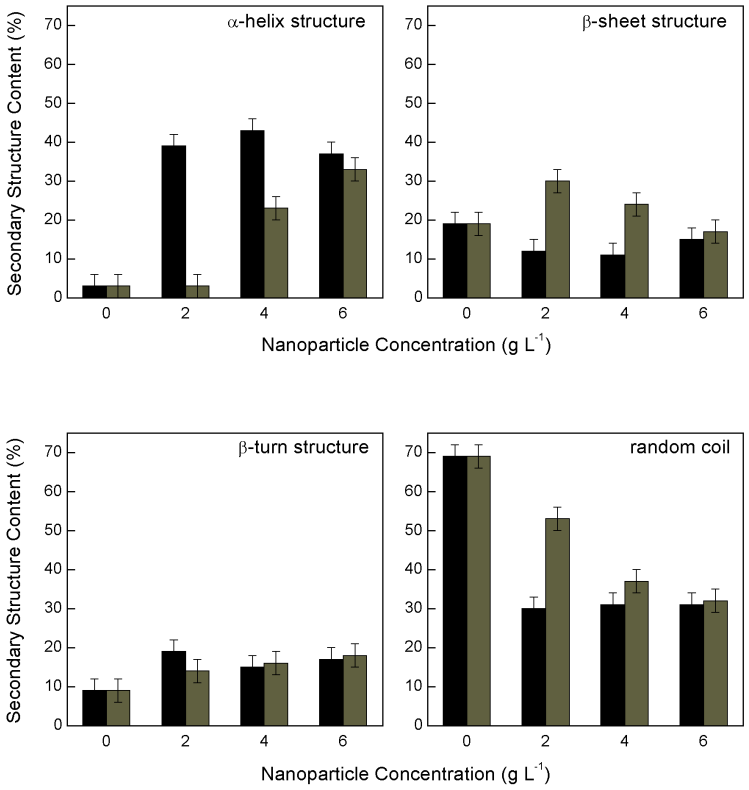

Figure 6.11. The relative percentage of the various secondary structural elements of B18 peptide in the presence of complex P_1 fluorinated (black bars) and hydrogenated (gray bars).

For the hydrogenated nanoparticles P_2H at pH 7 the change of the circular dichroism

signal was low at a particle concentration of 2 g L^{-1} but changed greatly at the higher concentrations (Figure 6.9 (b)). The titration of B18 solution with increasing amounts of complex P_2H was accompanied by occurrence of significant precipitation. A calculation of the secondary structure was therefore not possible. Nevertheless from the shape of the spectra (curves 3 and 4 in Figure 6.9 (b)) B18 seemed to contain mainly β-sheet and random coil motifs at particle concentrations of 4 and 6 g L^{-1}.

B18 peptide is fully charged at pH 4, at which it carries five positive charges. At this pH, protonation of the carboxylic group of the polyampholytes is expected to occur, which will destabilize the particles and may lead to aggregation. Most likely aggregation of B18 in the presence of hydrogenated nanoparticles at pH 4 results from the destabilization of the complexes. Since the perfluorododecanoic acid is a stronger acid than the dodecanoic one, the fluorinated particles are more stable, and aggregation is not observed.

At pH 7, partial deprotonation of the histidine residues is expected to occur and the peptide becomes less charged. At this pH all the complexes are stable [130]. The fluorinated nanoparticles induce α-helix structure in B18 peptide. The influence of the hydrogenated nanoparticles depends on the polyampholyte. An α-helix structure is induced by P_1H, whereas aggregation or β-sheet formation is observed for P_2H. The zeta potential of P_1H complex is $+25$ mV, whereas that of P_2H is about -20 mV, which indicates that the complexes have opposite electric charge. The aggregation of B18 in the presence of P_2H can be explained by charge compensation between the peptide and the complex. This suggests that the highly negative zeta potential of the fluorinated particles is an important parameter to observe the α-helix inducing effect. Thus electrostatic interactions play a certain role in the resulting secondary structure of B18. However, the fact that P_1H, which has a positive zeta potential, is able to induce α-helix indicates that B18 interacts with nanoparticles by hydrophobic interactions.

6.3 The Conformation of Amyloid beta-Peptide in the Presence of Nanoparticles

The secondary structure of the amyloid β-peptide (1–40) at pH 7 in the presence of different amounts of nanoparticles was characterized by circular dichroism spectroscopy at $(20 \pm 1)^{\circ}$C. Final particle concentrations were 0, 2, 4 and 8 g L^{-1}. The final peptide concentration was 53 μM.

The amyloid β-peptide (1–40) at pH 7, in the absence of particles, was mainly in random coil and β-sheet conformations. The secondary structure estimation resulted in a content of 3% α-helix, 27% β-sheet, 14% β-turn and 56% random coil.

The circular dichroism spectra of amyloid β-peptide (1–40) after titration with P_1 complex are shown in Figure 6.12. It can be seen from Figure 6.12 (a), curves 2 to 4, that fluorinated nanoparticles P_1F induced a change from random coil to α-helix structure. This

two state process is supported by the observation of an isosbestic point at 203 nm. The content of α-helix was 8%, 16% and 31% after the addition of 2, 4 and 8 g L^{-1} fluorinated nanoparticles P_1F, respectively (Figure 6.13 (a)). The random coil structure decreased to 27%, whereas the content of β-sheet and β-turn was approximately constant.

The hydrogenated particles P_1H, in contrast to the fluorinated nanoparticles, did not induce α-helix rich structure on amyloid β-peptide (Figure 6.12 (b)). The titration of amyloid β-peptide with hydrogenated nanoparticles P_1H resulted in circular dichroism spectra of typical β-sheet protein (minimum at 215 nm). The fraction of β-sheet increased from 27% to 37% and the random coil content decreased from 56% to 37% (Figure 6.13 (b)), suggesting a two state transition from random coil to β-sheet structure.

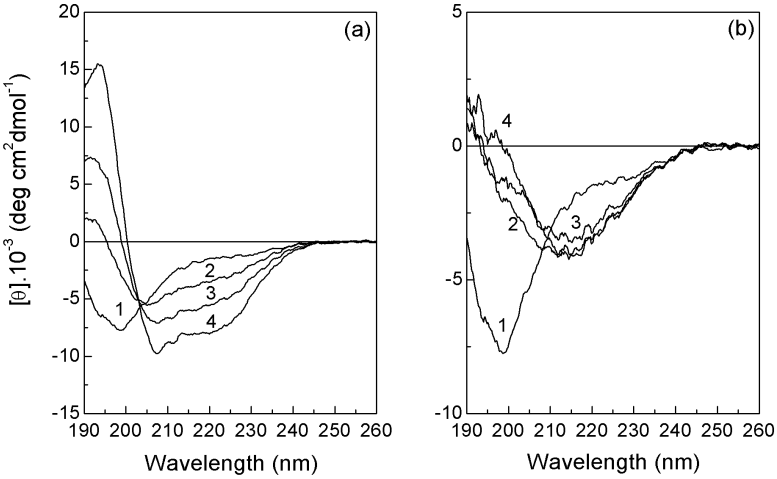

Figure 6.12. Circular dichroism spectra of amyloid β-peptide at pH 7 in the presence of complex P_1 fluorinated (a) and hydrogenated (b): 0 g L^{-1} (curve 1), 2 g L^{-1} (curve 2), 4 g L^{-1} (curve 3) and 8 g L^{-1} (curve 4).

Figure 6.14 shows the circular dichroism spectra of amyloid β-peptide (1–40) in the presence of complex P_2. After addition of fluorinated particles P_2F the spectra were reminiscent of α-helix structure, particular at high complex concentration (8 g L^{-1}), as observed in Figure 6.14 (a). In this case the increase in α-helix content was, however, smaller (from 3% to 21%) than the increase observed after addition of 8 g L^{-1} of complex P_1F (from 3% to 31%). The random coil fraction decreased to 36% (Table 6.3).

The titration of amyloid β-peptide (1–40) with hydrogenated nanoparticles P_2H resulted in a decrease of the circular dichroism signal with increasing concentration of the nanoparticles (Figure 6.14 (b)), suggesting the occurrence of aggregation. The presence of peptide aggregates is known to reduce the circular dichroism signal intensity due to light scattering and a shadowing effect [138].

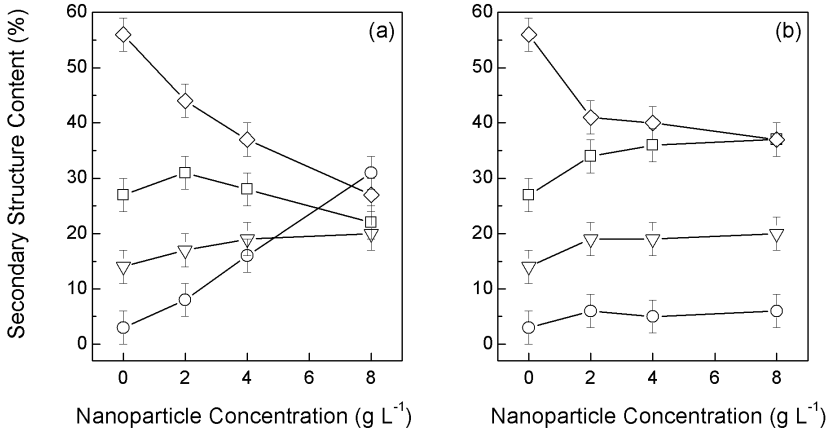

Figure 6.13. Percentage of secondary structure motifs of amyloid β-peptide at pH 7 in the presence of different concentrations of complex P_1 fluorinated (a) and hydrogenated (b): α-helix (○), β-sheet (□), β-turn (▽) and random coil (◇).

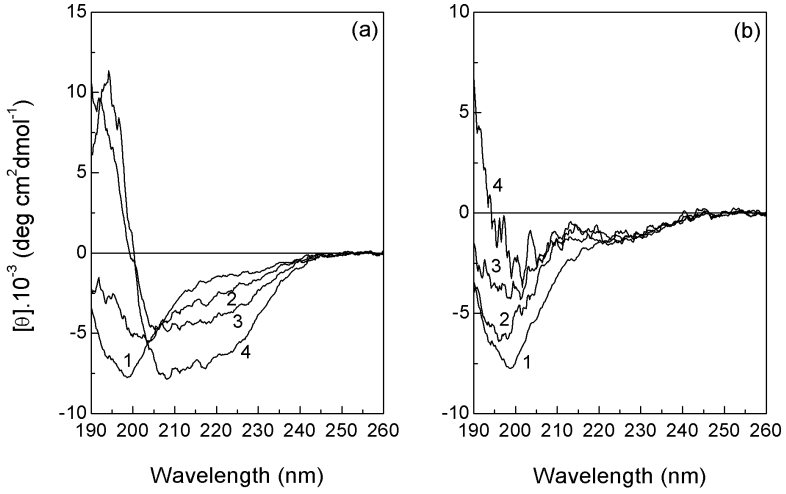

Figure 6.14. Circular dichroism spectra of amyloid β-peptide at pH 7 in the presence of complex P_2 fluorinated (a) and hydrogenated (b): 0 g L^{-1} (curve 1), 2 g L^{-1} (curve 2), 4 g L^{-1} (curve 3) and 8 g L^{-1} (curve 4).

Conc. (g L^{-1})	Helix (%)	Strand (%)	Turn (%)	Unordered (%)
0	3	27	14	56
2	4	29	15	52
4	8	33	21	38
8	21	24	19	36

Table 6.3. Percentage of secondary structure motifs ($\pm$ 3%) of amyloid β-peptide in the presence of fluorinated nanoparticles P_2F at different particle concentrations and pH 7 calculated by CONTIN/LL program.

Fluorinated nanoparticles induce α-helix rich structures in amyloid β-peptide (1–40) at pH 7, whereas the hydrogenated ones lead to β-sheet formation and aggregation. Previous studies have shown that hydrophobic teflon particles, with a zeta potential of approximately -47 mV and size of 200 nm, are able to induce α-helix structure in amyloid β-peptide [95]. These studies are in agreement with the results presented here.

At pH 4.5–6.6, at which the peptide has six positively and six negatively charged residues, the aggregated β-sheet structure is stabilized by intermolecular ion-pairing interactions and hydrophobic interactions [67–70, 104]. At pH 7 the side chains of glutamic acid and aspartic acid (pK_a 4.5) are deprotonated (COO^-, residues 1, 3, 7, 11, 22, 23), the side chains of lysine and arginine are protonated ($-NH_3^+$, $=NH^+$, residues 5, 16, 28) and a partial deprotonation of histidine side chain (pK_a 6.5) may occur ($3NH^+ \rightarrow 3N$, residues 6, 13, 14). It was previously demonstrated that the pK_a values of glutamic acid, aspartic acid and histidine were higher by about 1.5 units in the presence of negatively charged micelles, which induce α-helix structure in amyloid β-peptide [104]. The highly negatively charged environment around the micelle hindered the deprotonation of these residues' side chain. This implies that electrostatic attraction between the peptide and negatively charged micelles occurs and favors the helical state of the peptide.

Fluorinated nanoparticles show high negative surface charges with zeta potential of approximately -50 mV. This suggests that fluorinated nanoparticles may have a similar effect on the pK_a values of the peptide residues as highly negatively charged micelles, resulting in favorable electrostatic attraction between the peptide and the particles. It is possible that the α-helix structure results from electrostatic attraction provided by negatively charged nanoparticles, which drive the peptide to the surface of the particle, and hydrophobic interactions with the fluorinated chains that stabilize the peptide-particle interaction, similar to the mechanism proposed for the interaction of the peptide with micelles, described in section 5.3. The less pronounced α-helix inducing effect of fluorinated complex P_2F on amyloid β-peptide compared with complex P_1F is likely explained by the presence of the phenyl group on the polyampholyte of complex P_2F. It can be that this group constitutes a barrier that prevents fluorine groups to reach the particle surface or blocks a possible penetration of the peptide into the particle.

The hydrogenated nanoparticles in contrast have zeta potentials of $+25$ and -20 mV,

depending on the polyampholyte structure. This suggests that the surface charge of the hydrogenated particles is relatively lower than that of the fluorinated ones. The hydrogenated particles are not able to preventing the ion-pairing interaction between peptide molecules, which will lead to β-sheet formation and aggregation. In addition charge compensation may be occurring between the peptide and the particles resulting in aggregation.

6.4 Structure Stabilization by Fluorinated Nanoparticles

The strong effect of fluorinated nanoparticles on the secondary structure of the peptide indicates that the particles have a dynamic structure where a part of the fluorinated chains is in contact with the hydrophilic phase. Due to the stiffness of fluorinated chains, a surfactant-block model similar to that proposed by Fromherz may be suitable to explain the packing of perfluorododecanoic acid molecules [139]. In this model the orientation of the surfactant molecules is parallel correlated, the width of a correlated surfactant block equals the length of the hydrocarbon chain, which is in an extended conformation perturbed by few gauche-trans-gauche kinks, and the surfactant blocks are assembled with the head groups separated as far as possible [139]. In the case of the nanoparticles, a surfactant-block model of the perfluorododecanoic acid molecules surrounded by the polyampholyte is proposed. Due to thermal fluctuations and the small size of the particles, some CF_3 groups are expected to be in contact with the hydrophilic phase. In this sense the system differs qualitatively from one with the flexible CH_3 groups where the hydrocarbons can be completely enveloped by the hydrophilic heads. A schematic representation of the fluorinated nanoparticle interacting with amyloid β-peptide is shown in Figure 6.15. The peptide associates at the particle/water interface by electrostatic attractions and subsequent hydrophobic interactions with fluorinated groups result in α-helix structure.

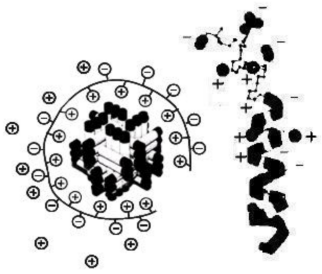

Figure 6.15. Proposed mechanism for the interaction of fluorinated nanoparticles with amyloid β-peptide. The structures are not scaled according to their relative sizes. The nanoparticle is illustrated as a block assembly of surfactant chains as proposed by Fromherz [139], surrounded by the polyampholyte chain. The black tips correspond to the head groups COO^-.

It has been demonstrated that fluorinated nanoparticles made of a polyampholyte-fluorosurfactant complex induce α-helix rich structures in B18 and amyloid β-peptide (1–40), whereas their hydrogenated analogues are less efficient leading in most cases to aggregation or β-sheet formation. The interaction of fluorinated particles with B18 and amyloid β-peptide suggests that for optimum response proper micelle engineering is required with enough fluorine outside to affect the peptide structure and a suitable particle/peptide ratio to avoid precipitation.

Fluorinated nanoparticles are proposed to be potential candidates for the inhibition of conformational changes of proteins that lead to amyloid fibril formation.

7 Conclusions

Several human diseases are caused by protein misfolding and aggregation beyond the influence of cellular quality-control systems. In these diseases, proteins seem to fold efficiently but they misfold in their destination environments, and aggregate as insoluble amyloid fibrils. Accumulation of fibrils ultimately disrupts tissue structure and function. This pathological process is observed in diseases such as Alzheimer's and systemic amyloidosis.

The reasons for natively soluble proteins of distinct primary structure to undergo partial unfolding and aberrant refolding to produce highly stable structures are not completely clear. Supraphysiological protein concentrations, coupled with prolonged time and certain biochemical conditions, may initialize the oligomerization process. The local protein concentration may well increase as a result of mutations or surface interactions.

The mechanism by which misfolded proteins induce cellular injury is even more complex to understand. In the case of Alzheimer's disease, studies with transgenic mices overexpressing mutant human amyloid precursor protein seem to point for a decrease in presynaptic nerve terminal and neuronal cell bodies when concentrations of soluble amyloid β-peptide are increasing. Hence the inhibition of abnormal conformational alterations and fibril formation seems to be a reasonable therapeutic strategy for protein misfolding associated diseases.

In this thesis the behavior of the fibril-forming peptides B18 and amyloid β-peptide (1–40) at surfaces and interfaces was characterized, as well as their conformation in the presence of amphiphiles, in order to gain insights into the role of surfaces and membrane mimicking systems in the peptide structure and aggregation. In addition nanoparticles made of polyampholytes complexed with hydrogenated or perfluorinated surfactants were prepared, aiming at the development of α-helix inducing agents, hence aggregation inhibitors. Their influence on the peptide structure was determined.

The adsorption of peptides on modified surfaces was studied by X-ray and neutron reflectometry and by atomic force microscopy. Exposure of an aqueous protein solution to a solid surface typically results in excess accumulation of protein molecules at the solid/liquid interface. This tendency for proteins to adsorb spontaneously may have implications on fibril formation in amyloid associated diseases. The degree of adsorption of B18 and amyloid β-peptide was determined at pH 7 on different surfaces: negatively

and positively charged hydrophilic films, as well as hydrophobic polymers. B18 peptide did not adsorb on hydrophilic positively charged surfaces, which was attributed to electrostatic repulsion between the positively charged peptide and the surface. In contrast, the peptide was found to adsorb on negatively charged surfaces and hydrophobic surfaces. The peptide showed higher affinity for hydrophobic surfaces than for hydrophilic negatively charged surfaces, which was determined by adsorption kinetic studies. B18 peptide adsorbed irreversibly on hydrophobic surfaces after 20 minutes adsorption time, whereas it required more than one hour to adsorb on negatively charged surfaces. The affinity for hydrophobic surfaces must be caused by its seven leucine residues, which are highly hydrophobic. Atomic force microscopy provided the indication that lateral diffusion on the surface affects the adsorption process of B18 on hydrophobic surfaces. The adsorption of B18 on negatively charged surfaces was characterized by the formation of globular clusters.

Amyloid β-peptide was found to adsorb on positively charged surfaces and hydrophobic surfaces but not on non-charged and negatively charged surfaces. This behavior was attributed to the charge distribution and hydrophobic residues of the molecule. Amyloid β-peptide has a net negative charge at pH 7, which favors the electrostatic attraction between the peptide and positively charged surfaces. The peptide adsorbed on the positively charged film as compact patches with very low water content and a thickness of 20 Å. This observation associated with the fact that the positively charged polymer induced a β-sheet structure in amyloid β-peptide suggests that the peptide adsorbed as β-strands. On the other hand there is no electrostatic attraction between the peptide and the non-charged surface. Moreover electrostatic repulsion might occur between the molecule and negatively charged surfaces. The absence of adsorption on non-charged and negatively charged films suggests that electrostatic interactions are the driving forces for the adsorption of amyloid β-peptide on hydrophilic surfaces. The adsorption on hydrophobic surfaces must result from hydrophobic interactions since the peptide has two hydrophobic domains, residues 17–21 and 29–40. Again a very compact peptide layer was observed. The thickness of the adsorbed peptide layer at two different hydrophobic surfaces was 12 and 20 Å, which agrees well with the presence of one pleated sheet and two pleated sheets, respectively. It was additionally observed that amyloid β-peptide undergoes a transition from random coil to β-sheet structure when in contact with air, but no conformational alterations are detected when the peptide is stored in negatively charged cuvettes hermetically sealed. These results suggest that adsorption of amyloid β-peptide results in conformational rearrangement that might lead to β-sheet formation and aggregation. Understanding and controlling the adsorption process may be important for *in vivo* inhibition of amyloid fibril formation.

The conformation of B18 and amyloid β-peptide in the presence of amphiphiles (anionic sodium dodecyl sulphate, anionic pentadecafluorooctanoic acid, cationic cetyltrime-

thylammonium chloride, and nonionic 1-*O*-*n*-octyl-β-D-glucopyranoside) at physiological pH of 7 was characterized by circular dichroism spectroscopy.

B18 peptide was observed to adopt an α-helix structure in the presence of charged amphiphiles independently from the fact whether the amphiphiles formed micelles or not. At pH 7, B18 carries only positive charges, indicating that hydrophobic interactions are the major forces in determining the helical state of the peptide in charged amphiphile solutions. The nonionic amphiphile has a large polar group and a short chain length, thus the monomers had no significant influence on the peptide structure. In contrast, the nonionic micelles induced a partial α-helix structure. In this case the conformational transition seems to result from surface interaction and might be due to the micelle curvature that forces the peptide to bend and to adopt a more favorable conformation.

Amyloid β-peptide showed a complex behavior when interacting with the monomers, which is most probably related to the hydrophobic/hydrophilic part of the amphiphile. Nevertheless it was observed that a β-sheet structure is formed in the presence of charged monomers at certain concentrations. This is an indication that membrane damage *in vivo* might expose the lipid chains and lead to peptide aggregation. The peptide structural changes in the presence of micelles were more consistent and some conclusions can be drawn. Both cationic and anionic micelles induced an α-helix structure on amyloid β-peptide, whereas the nonionic micelles induced a β-sheet structure. In the case of amyloid β-peptide the electrostatic contribution seems to be important for the helical stability, whereas the β-sheet structure seems to result from hydrogen bonds between the peptide and the micelle. The interaction effect of amphiphiles on amyloid peptides highlights the complexity of conformational peptide changes in biological environments and requires more detailed studies in order to better understand the precise reasons of misfolding. Nevertheless the studies of amphiphiles interacting with peptides provided the important conclusion that perfluorinated micelles are effective α-helix inducing agents. A natural consequence of this observation is to expect that combining highly charged polymers with fluorinated compounds will enhance the α-helix inducing effect.

It was previously demonstrated that polyelectrolyte-fluorosurfactant complexes dissolve amyloid plaques in sections of animal tissue and convert β-sheet into α-helix structures. These complexes were tested on solid supports. In order to increase the contact area between peptide molecules and complexes, nanoparticles of these complexes were synthesized. Polyampholytes with alternating cationic and anionic charged monomers were synthesized with a degree of polymerization in the range of 60 to 80. Complexes of the polyampholytes and dodecanoic and perfluorododecanoic acid, respectively, were prepared. This resulted, in both cases, in nanoparticles with hydrodynamic diameters ranging from 3 to 5 nm. The radii of gyration of the nanoparticles were 2 nm, confirming that the particles are small. Accordingly they have high specific surface areas of approximately 1000 $m^2\ g^{-1}$. It can be expected that the high surface area would be useful in providing

extensive interactions with the peptide. The nanoparticles displayed surface charges with zeta potentials of -50 mV when fluorinated and in the range of -20 to $+25$ mV when hydrogenated. They dissolved at concentrations lower than 0.02 g L^{-1} (that is, they are not covalently cross-linked). The nanoparticles are thought to consist of a hydrophobic core (formed by the surfactant chains) and a hydrophilic charged shell. Though, to induce a change of a water soluble peptide, the fluorinated nanoparticles must have a dynamic structure where a part of the fluorinated chains is in contact with the hydrophilic phase.

The fluorinated nanoparticles induced α-helix rich structures in B18 and amyloid β-peptide, whereas their hydrogenated analogues were less efficient leading in most cases to aggregation or β-sheet formation, as determined by circular dichroism spectroscopy. The stabilization of the α-helix structure of B18 by fluorinated particles is thought to result from hydrophobic interactions. In the case of amyloid β-peptide, electrostatic interactions seem dominant in driving the peptide to the particle surface and subsequent hydrophobic interactions with the fluorinated groups stabilize the peptide structure. Thus it is evident that fluorinated groups conferred appropriate properties to the nanoparticles to induce monomeric α-helix structure.

The studies presented in this thesis provided information concerning peptide-surface interactions that might be responsible for peptide aggregation and a possible strategy to prevent amyloid fibril formation through the stabilization of α-helix structure by fluorinated micelles and nanoparticles.

A Symbols and Abbreviations

A	Absorbance
AFM	Atomic force microscopy
b	Scattering length of atomic species
β	Absorption term
C	Concentration
cmc	Critical micellar concentration
$CTAC$	Cetyltrimethylammonium chloride
D	Diffusion coefficient
d	Thickness
δ	Dispersion term
E	Electric vector
ε	Molar extinction coefficient
ϕ	Volume fraction
G	Gibbs free energy
Γ	Decay constant
H	Enthalpy
I	Intensity of the reflected or transmitted radiation
I_0	Intensity of the incident radiation
η	Viscosity
k_B	Boltzmann's constant
K	Wave vector
l_p	Average chord length
λ	Wavelength
μ_E	Electrophoretic mobility
n	Refractive index
OG	1-O-n-octyl-β-D-glucopyranoside
N_A	Avogadro's constant
OTS	n-Octadecyltrichlorosilane
PAH	Poly(allylamine hydrochloride)

PEI	Poly(ethyleneimine)
$PFOA$	Pentadecafluorooctanoic acid
PF	Polyampholyte complexes with perfluorododecanoic acid
PH	Polyampholyte complexes with dodecanoic acid
PSS	Poly(sodium 4-styrenesulfonate)
q	Scattering vector
r	Reflection coefficient
R	Reflectivity
R_F	Fresnel Reflectivity
$[\theta]$	Molar ellipticity
ρ	Density
s	Sedimentation coefficient
S	Entropy
SDS	Sodium dodecyl sulphate
σ	Root mean square roughness
V_m	Molecular volume
T	Temperature
$\omega^2 t$	Centrifugal field
ζ	Zeta potential

Bibliography

[1] Selkoe D. J. Folding proteins in fatal ways. *Nature* 2003, 426, 900–904.

[2] Stefani M., Dobson C. M. Protein aggregation and aggregate toxicity: new insights into protein folding, misfolding diseases and biological evolution. *J. Mol. Med.* 2003, 81, 678–699.

[3] Soto C. Unfolding the role of protein misfolding in neurodegenerative diseases. *Nature Reviews Neurosci.* 2003, 4, 49–60.

[4] Selkoe D. J. Alzheimer's disease: genes, proteins and therapy. *Physiol. Rev.* 2001, 81, 741–766.

[5] Uverskya V. N., Finka A. L. Conformational constraints for amyloid fibrillation: the importance of being unfolded. *Biochim. Biophys. Acta* 2004, 1698, 131–153.

[6] Sunde M., Blake C. The structure of amyloid fibrils by electron microscopy and X-ray diffraction. *Adv. Protein Chem.* 1997, 50, 123–159.

[7] Ulrich A. S., Otter M., Glabe C. G., Hoekstra D. Membrane fusion is induced by a distinct peptide sequence of the sea urchin fertilization protein bindin. *J. Biol. Chem.* 1998, 273, 16748–16755.

[8] Ulrich A. S., Tichelaar W., Förster G., Zschörnig O., Weinkauf S., Meyer H. W. Ultrastructural characterization of peptide-induced membrane fusion and peptide self-assembly in lipid bilayer. *Biophys. J.* 1999, 77, 829–841.

[9] Chiti F., Webster P., Taddei N., Clark A., Stefani M., Ramponi G., Dobson C. M. Designing conditions for *in vitro* formation of amyloid protofilaments and fibrils. *Proc. Natl. Acad. Sci.* 1999, 96, 3590–3594.

[10] Pillot T., Goethals M., Vanloo B., Talussot C., Brasseur R., Vandekerckhove J., Rosseneu M., Lins L. Fusogenic properties of the C-terminal domain of the Alzheimer β-amyloid peptide. *J. Biol. Chem.* 1996, 271, 28757–28765.

[11] Lansbury P. T. Evolution of amyloid: what normal protein folding may tell us about fibrillogenesis and disease. *Proc. Natl. Acad. Sci.* 1999, 96, 3342–3344.

[12] Kelly J. W. The alternative conformations of amyloidogenic proteins and their multi-step assembly pathways. *Curr. Opin. Struct. Biol.* 1998, 8, 101–106.

[13] Miraglia S. J., Glabe C. G. Characterization of the membrane-associating domain of the sperm adhesive protein bindin. *Biochem. Biophys. Acta* 1993, 1145, 191–198.

[14] McLaurin J., Yang D. S., Yip C. M., Fraser P. E. Review: Modulating factors in amyloid-β fibril formation. *J. Struct. Biol.* 2000, 130, 259–270.

[15] Selkoe D. J. Toward a comprehensive theory for Alzheimer's disease. Hypothesis: Alzheimer's disease is caused by the cerebral accumulation and cytotoxicity of amyloid β-protein. *Ann. NY Acad. Sci.* 2000, 924, 17–25.

[16] Anfinsen C. B. Principles that govern the folding of protein chain. *Science* 1973, 181, 223–230.

[17] Stryer L. *Biochemistry*, 4th ed., W. H. Freeman and Company, New York, 1995.

[18] Hartl F. U., Mayer-Hartl M. Molecular chaperones in the cytosol: from nascent chain to folded protein. *Science* 2002, 295, 1852–1858.

[19] Goldberg A. L. Protein degradation and protection against misfolded or damaged proteins. *Nature* 2003, 426, 895–899.

[20] Dobson C. M., Sali A., Karplus M. Protein Folding: A perspective from theory and experiment. *Angew. Chem. Int. Ed.* 1998, 37, 868–893.

[21] Dill K. A. Dominant Forces in Protein Folding. *Biochemistry* 1990, 29, 7133–7155.

[22] Privalov P. L. Stability of proteins. *Adv. Protein Chem.* 1979, 33, 167–241.

[23] Miller S., Janin J., Lesk A. M., Chothia C. Interior and surface of monomeric proteins. *J. Mol. Biol.* 1987, 196, 641–656.

[24] Dill K. A., Chan H. S. From Levinthal to pathways to funnels. *Nat. Struct. Biol.* 1997, 4, 10–19.

[25] Creighton T. E. *Proteins: structure and molecular properties*. W. H. Freeman and Company, New York, 1992, 2nd ed.

[26] Hirschfield G. M., Hawkins P. N. Amyloidosis: new strategies for treatment. *Int. J. Biochem. Cell B.* 2003, 35, 1608–1613.

[27] Martin J. B. Molecular basis of the neurodegenerative disorders. *N. Eng. J. Med.* 1999, 340, 1970–1980.

[28] Förstl H., Kurz A. Clinical features of Alzheimer's disease. *Eur. Arch. Psychiatry Clin. Neurosci.* 1999, 249, 288–290.

[29] Selkoe D. J. The molecular pathology of Alzheimer's disease. *Neuron* 1991, 6, 487–498.

[30] Serpell L. C. Alzheimer's amyloid fibrils: structure and assembly. *Biochim. Biophys. Acta* 2000, *1502*, 16–30.

[31] Guijarro J. I., Sunde M., Jones J. A., Campbell I. D., Dobson C. M. Amyloid fibril formation by an SH3 domain. *Proc. Natl. Acad. Sci.* 1998, 95, 4224–4228.

[32] Fändrich M., Fletcher M. A., Dobson C. M. Amyloid fibrils from muscle myoglobin. *Nature* 2001, 410, 165–166.

[33] Pertinhez T. A., Bouchard M., Tomlinson E. J., Wain R., Ferguson S. T., Dobson C. M., Smith L. J. Amyloid fibril formation by a helical cytochrome. *FEBS Lett.* 2001, 495, 184–186.

[34] Mrak R. E., Griffin S. T., Graham D. I. Aging-associated changes in human brain. *J. Neuropathol. Exp. Neurol.* 1997, 56, 1269–1275.

[35] Jarrett J. T., Lansbury Jr. P. T. Seeding one-dimensional crystallization of amyloid: a pathogenic mechanism in Alzheimer's disease and scrapie. *Cell* 1993, 73, 1055–1058.

[36] Lomakin A., Chung D. S., Benedek G. B., Kirschner D. A., Teplow D. B. On the nucleation and growth of amyloid β-protein fibrils: detection of nuclei and quantitation of rate constants. *Proc. Natl. Acad. Sci.* 1996, 93, 1125–1129.

[37] Come J. H., Fraser P. E., Lansbury Jr. P. T. A kinetic model for amyloid formation in the prion diseases: Importance of seeding. *Proc. Natl. Acad. Sci.* 1993, 90, 5959–5963.

[38] Walsh D. M., Lomakin A., Benedek G. B., Condron M. M., Teplow D. V. Amyloid β-protein fibrillogenesis: detection of a protofibrillar intermediate. *J. Biol. Chem.* 1997, 272, 25945–25952.

[39] Conway K. A. Harper J. D., Lansbury P. T. Accelerated in vitro fibril formation by a mutant α-synuclein linked to early-onset Parkinson disease. *Nature Med.* 1998, 4, 1318–1320.

[40] Walsh D. M., Hartley D. M., Kusumoto Y., Fezoui Y., Condron M. M., Lomakin A., Benedek G. B., Selkoe D. J., Teplow D. B. Amyloid β-protein fibrillogenesis:

structure and biological activity of protofibrillar intermediates. *J. Biol. Chem.* 1999, 274, 22364–22372.

[41] Bucciantini M., Giannoni E., Chiti F., Baroni F., Formigli L., Zurdo J., Taddei N., Ramponi G., Dobson C. M., Stefani M. Inherent toxicity of aggregates implies a common mechanism for protein misfolding diseases. *Nature* 2002, 416, 507–511.

[42] Söllner T., Whiteleart S. W., Brunner M., Erdjument-Bromage H., Geromanos S., Tempst P., Rothman E. R. SNAP receptors implicated in vesicle targeting and fusion. *Nature* 1993, 362, 318–324.

[43] Angel V. D., Dupuis F., Mornon J. P., Callebaut I. Viral fusion peptides and identification of membrane-interacting segments. *Biochem. Biophys. Res. Commun.* 2002, 293, 1153–1160.

[44] Tamm L. K., Han X. Viral fusion peptides: a tool set to disrupt and connect biological membranes. *Bioscience Rep.* 2000, 20, 501–518.

[45] Binder H., Arnold K., Ulrich A. S., Zschörnig O. The effect of Zn^{2+} on the secondary structure of a histidine-rich fusogenic peptide and its interaction with lipid membranes. *Biochim. Biophys. Acta* 2000, 1468, 345–358.

[46] Glaser R. W., Grüne M., Wandelt C., Ulrich A. S. Structure analysis of a fusogenic peptide sequence from the sea urchin fertilization protein bindin. *Biochemistry* 1999, 38, 2560–2569.

[47] Barré P., Zschörnig O., Arnold K., Huster D. Structural and dynamical changes of the bindin B18 peptide upon binding to lipid membranes. A solid-state NMR study. *Biochemistry* 2003, 42, 8377–8386.

[48] Pillot T., Lins L., Goethals M., Vanloo B., Baert J., Vandekerckhove J., Rosseneu M., Brasseur R. The 118–135 peptide of the human prion protein forms amyloid fibrils and induces liposome fusion. *J. Mol. Biol.* 1997, 274, 381–393.

[49] Halverson K., Fraser P. E., Kirschner D. A., Lansbury Jr, P. T. Molecular determinants of amyloid depositions in Alzheimer's disease: conformational studies of synthetic β-protein fragments. *Biochemistry* 1990, 29, 2639–2644.

[50] Lundberg K. M., Stenland C. J., Cohen F. E., Prusiner S. B., Millhauser G. L. Kinetics and mechanism of amyloid formation by the prion protein Hl peptide as determined by time-dependent ESR. *Biol. Chem.* 1997, 345–355.

[51] Selkoe D. J., Abraham C. R., Podlisny M. B., Duffy L. K. Isolation of low-molecular-weight proteins from amyloid plaque fibers in Alzheimer's disease. *J. Neurochem.* 1986, 46, 1820–1834.

[52] Joachim C. L., Duffy L. K., Morris J. H., Selkoe D. J. Protein chemical and immunocytochemical studies of meningovascular β-amyloid protein in Alzheimer's disease and normal aging. *Brain Res.* 1988, 474, 100–111.

[53] Tagliavini F., Giaccone G., Frangione B., Bugiani O. Preamyloid deposits in the cerebral cortex of patients with Alzheimer's disease and nondemented individuals. *Neurosci. Lett.* 1988, 93, 191–196.

[54] Kang J., Lemaire H. G., Unterbeck A., Salbaum J. M., Masters C. L., Grzeschik K. H., Multhaup G., Beyreuther K., Müller-Hill B. The precursor of Alzheimer's disease amyloid A4 protein resembles a cell-surface receptor. *Nature* 1987, 325, 733–736.

[55] Selkoe D. J. Normal and abnormal biology of the β-amyloid precursor protein. *Annu. Rev. Neurosci.* 1994, 17, 489–517.

[56] Haass C., Schlossmacher M. G., Hung A. Y., Vigo-Pelfrey C., Mellon A., Ostaszewski B. L., Lieberburg I., Koo E. H., Schenk D., Teplow D. B., Selkoe D. J. Amyloid β-peptide is produced by cultured cells during normal metabolism. *Nature* 1992, 359, 322–325.

[57] Seubert P., Vigo-Pelfrey C., Esch F., Lee M., Dovey H., Davis D., Sinha S., Schlossmacher M., Whaley J., Swindlehurst C., McCormack R., Wolfert R., Selkoe D., Lieberburg I., Schenk D. Isolation and quantification of soluble Alzheimer's β-peptide from biological fluids. *Nature* 1992, 359, 325–327.

[58] Adessi C., Soto C. Beta-sheet breaker strategy for the treatment of Alzheimer's disease. *Drug Develop. Res.* 2002, 56, 184–193.

[59] Van Leuven F. Single and multiple transgenic mice as models for Alzheimer's disease. *Prog. Neurobiol.* 2000, 61, 305–312.

[60] Walsh D. M., Klyubin I., Fadeeva J. V., Cullen W. K., Anwyl R., Wolfe M. S., Rowan M. J., Selkoe D. J. Naturally secreted oligomers of amyloid β protein potently inhibit hippocampal long-term potentiation *in vivo*. *Nature* 2002, 416, 535–539.

[61] Pike C. J., Walencewicz A. J., Glabe C. G., Cotman C. W. In vitro aging of β-amyloid protein causes peptide aggregation and neurotoxicity. *Brain Res.* 1991, 563, 311–314.

[62] Kirschner D. A., Abraham C., Selkoe D. J. X-ray diffraction from intraneuronal paired helical filaments and extraneuronal amyloid fibers in Alzheimer disease indicates cross-beta conformation. *Proc. Natl. Acad. Sci.* 1986, 83, 503–507.

[63] Spillantini M. G., Goedert M., Jakes R., Klug A. Different configurational states of β-amyloid and their distributions relative to plaques and tangles in Alzheimer's disease. *Proc. Natl. Acad. Sci.* 1990, 87, 3947–3951.

[64] Hilbich C., Kisters-Woike B., Reed J., Masters C. L., Beyreuther K. Aggregation and secondary structure of synthetic amyloid βA4 peptides of Alzheimer's disease. *J. Mol. Biol.* 1991, 218, 149–163.

[65] Barrow C. J., Yasuda A., Kenny P. T. M., Zagorski M. G. Solution conformations and aggregational properties of synthetic amyloid β-peptide of Alzheimer's disease. *J. Mol. Biol.* 1992, 225, 1075–1093.

[66] Kirschner D. A., Inouye H., Duffy L. K., Sinclair A., Lind M., Selkoe D. J. Synthetic peptide homologous to β protein from Alzheimer disease forms amyloid-like fibrils in vitro. *Proc. Natl. Acad. Sci.* 1987, 84, 6953–6957.

[67] Hilbich C., Kisters-Woike B., Reed J., Masters C. L., Beyreuther K. Substitutions of hydrophobic amino acids reduce the amyloidogenicity of Alzheimer's disease βA4 peptides. *J. Mol. Biol.* 1992, 228, 460–473.

[68] Jarret J. T., Berger E. P., Lansbury Jr. P. T. The carboxy terminus of the β amyloid protein is critical for the seeding of amyloid formation: implications for the pathogenesis of Alzheimer's disease. *Biochemistry* 1993, 32, 4693–4697.

[69] Fraser P. E., McLachlan D. R., Surewicz W. K., Mizzen C. A., Snow A. D., Nguyen J. T., Kirschner D. A. Conformation and fibrillogenesis of Alzheimer Aβ peptides with selected substitution of charged residues. *J. Mol. Biol.* 1994, 244, 64–73.

[70] Soto C., Castaño E. M., Frangione B., Inestrosa N. C. The α-helical to β-strand transition in the amino-terminal fragment of the amyloid β-peptide modulates amyloid formation. *J. Biol. Chem.* 1995, 270, 3063–3067.

[71] Yong W., Lomakin A., Kirkitadze M. D., Teplow D. B., Chen S. H., Benedek G. B. Structure determination of micelle-like intermediates in amyloid β-protein fibril assembly by using small angle neutron scattering. *Proc. Natl. Acad. Sci.* 2002, 99, 150–254.

[72] Selkoe D. J., Schenk D. Alzheimer's disease: molecular understanding predicts amyloid-based therapeutics. *Annu. Rev. Pharmacol. Toxicol* 2003, 43, 545–584.

[73] Soto C., Castaño E. M., Kumar R. A., Beavis R. C, Frangione B. Fibrillogenesis of synthetic amyloid-β peptides is dependent on their initial secondary structure. *Neurosci. Lett.* 1995, 200, 105–108.

[74] Fasman G. D. *Circular dichroism and the conformational analysis of biomolecules*, Plenum Press, New York, 1996.

[75] Rohl C. A., Chakrabartty A., Baldwin R. L. Helix propagation and N-cap propensities of the amino acids measured in alanine-based peptides in 40 volume percent trifluoroethanol. *Protein Sci.* 1996, 5, 2623–2637.

[76] Greenfield N. J. Methods to estimate conformation of proteins and polypeptides from circular dichroism data. *Anal. Biochem.* 1996, 235, 1–10.

[77] Greenfield N., Fasman G. D. Computed circular dichroism spectra for the evaluation of protein conformation. *Biochemistry* 1969, 8, 4108–4116.

[78] Brahms S., Brahms J. Determination of protein secondary structure in solution by vacuum ultraviolet circular dichroism. *J. Mol. Biol.* 1980, 138, 149–178.

[79] Provencher S. W., Glöckner J. Estimation of globular protein secondary structure from circular dichroism. *Biochemistry* 1981, 20, 33–37.

[80] Sreerama N., Woody R. W. Estimation of protein secondary structure from circular dichroism spectra: comparison of CONTIN, SELCON, and CDSSTR methods with an expanded reference set. *Anal. Biochem.* 2000, 287, 252–260.

[81] Sreerama N., Venyaminov S. Y., Woody R. W. Estimation of protein secondary structure from circular dichroism spectra: inclusion of denatured proteins with native proteins in the analysis. *Anal. Biochem.* 2000, 287, 243–251.

[82] Daillant J., Gibaud A. *X-ray and neutron reflectivity: principles and applications*, Berlin Springer, 1999.

[83] Braun C. Parratt 32 Fitting routine for reflectivity data, HMI, Berlin, 1997–1999.

[84] Stahl N., Borchelt D. R., Hsiao K., Prusiner S. B. Scrapie prion protein contains a phosphatidylinositol glycolipid. *Cell* 1987, 51, 229–240.

[85] Caughey B., Raymond G. J. The scrapie-associated form of PrP is made from a cell surface precursor that is both protease- and phospholipase-sensitive. *J. Biol. Chem.* 1991, 266, 18217–18223.

[86] Borchelt D. R., Taraboulos A., Prusiner S. B. Evidence for synthesis of scrapie prion proteins in the endocytic pathway. *J. Biol. Chem.* 1992, 267, 16188–16199.

[87] Biere A. L., Ostaszewski B., Stimson E. R., Hyman B. T., Maggio J. E., Selkoe D. J. Amyloid β-peptide is transported on lipoproteins and albumin in human plasma. *J. Biol. Chem.* 1996, 271, 32916–32922.

[88] Koudinov A. R., Koudinova N. V., Kumar A., Beavis R. C., Ghiso J. Biochemical characterization of Alzheimer's soluble amyloid beta protein in human cerebrospinal fluid: association with high density lipoproteins. *Biochem. Byophys. Res. Commun.* 1996, 223, 592–597.

[89] Namba Y., Tomonaga M., Kawasaki H., Otomo E., Ikeda K. Apolipoprotein E immunoreactivity in cerebral amyloid deposits and neurofibrillary tangles in Alzheimer's disease and kuru plaque amyloid in Creutzfeldt-Jakob disease. *Brain Res* 1991, 541, 163–166.

[90] Matsuzaki K., Horikiri C. Interactions of amyloid β-peptide (1–40) with ganglioside-containing membranes. *Biochemistry* 1999, 38, 4137–4142.

[91] Yanagisawa K., Odaka A., Suzuki N., Ihara Y. GM1 ganglioside-bound amyloid β-protein (Aβ): A possible form of preamyloid in Alzheimer's disease. *Nat. Med.* 1995, 1, 1062–1066.

[92] Kowalewski T., Holtzman D. M. In situ atomic force microscopy study of Alzheimer's β-amyloid peptide on different substrates: new insights into mechanism of β-sheet formation. *Proc. Natl. Acad. Sci.* 1999, 96, 3688–3693.

[93] Schladitz C., Vieira E. P., Hermel H., Möhwald H. Amyloid-β-sheet formation at the air-water interface. *Biophys. J.* 1999, 77, 3305–3310.

[94] Maltseva E., Brezesinski G. Adsorption of amyloid beta (1–40) peptide to phosphatidylethanolamine monolayers. *Chem. Phys. Chem.* 2004, 5, 1185–1190.

[95] Giacomelli C. E., Norde W. Influence of hydrophobic teflon particles on the structure of amyloid β-peptide. *Biomacromolecules* 2003, 4, 1719–1726.

[96] Iler R. K. *The chemistry of silica*, Wiley, New York, 1979.

[97] Decher G. Fuzzy nanoassemblies: toward layered polymeric multicomposites. *Science* 1997, 277, 1232–1237.

[98] Arys X., Jonas A. M., Laschewsky A., Legras R. *Supramolecular polymers*. Marcel Dekker New York, 2000, 505–563.

[99] Ladam G., Schaad P., Voegel J. C., Schaaf P., Decher G., Cuisinier F. *In situ* determination of the structural properties of initially deposited polyelectrolyte multilayers. *Langmuir* 2000, *16*, 1249–1255.

[100] Haynes C. A., Norde W. Globular proteins at solid liquid interfaces. *Colloids surf. B* 1994, 2, 517–566.

[101] Zhu M., Souillac P. O., Ionescu-Zanetti C., Carter S. A., Fink A. L. Surface-catalyzed amyloid fibril formation. *J. Biol. Chem.* 2002, 277, 50914–50922.

[102] McLaurin J., Chakrabartty A. Membrane disruption by Alzheimer β-amyloid peptides mediated through specific binding to either phospholipids or gangliosides. *J. Biol. Chem.* 1996, 271, 26482–26489.

[103] Glasoe P. K., Long F. A. Use of glass electrodes to measure acidities in deuterium oxide. *J. Phys. Chem.* 1960, 64, 188–190.

[104] Ma K., Clancy E. L., Zhang Y., Ray D. G., Wollenberg K., Zagorski M. G. Residue-specific pK_a measurements of the β-peptide and mechanism of pH-induced amyloid formation. *J. Am. Chem. Soc.* 1999, 121, 8698–8706.

[105] Zhang S., Iwata K., Lachenmann M. J., Peng J. W., Li S., Stimson E. R., Lu Y. A., Felix A. M., Maggio J. E., Lee J. P. The Alzheimer's peptide Aβ adopts a collapsed coil structure in water. *J. Struct. Biol.* 2000, 130, 130–141.

[106] Sears V. F. Neutron scattering lengths and cross sections. *Neutron News* 1992, 3, 26–37.

[107] Kheterpal I., Zhou S., Cook K. D., Wetzel R. R. Aβ amyloid fibrils possess a core structure highly resistant to hydrogen exchange. *Proc. Natl. Acad. Sci.* 2000, 97, 13597–13601.

[108] Kracun I., Kalanj S., Talan-Hranilovic J., Cosovic C. Cortical distribution of gangliosides in Alzheimer's disease. *Neurochem. Int.* 1992, 20, 433–438.

[109] Pettegrew J. W., Panchalingam K., Hamilton R. L., McClure R. J. Brain membrane phospholipid alterations in Alzheimer's disease. *Neurochem. Res.* 2001, 26, 771–782.

[110] Zagorski M. G., Barrow C. J. NMR studies of amyloid β-peptides: proton assignments, secondary structure, and mechanism of an α-helix $\rightarrow$ β-sheet conversion for a homologus, 28-residue, N-terminal fragment. *Biochemistry* 1992, 31, 5621–5631.

[111] Otvos Jr. L., Szendrei G. I., Lee V. M. Y., Mantsch H. H. Human and rodent Alzheimer β-amyloid peptides acquire distinct conformations in membrane-mimicking solvents. *Eur. J. Biochem.* 1993, 211, 249–257.

[112] Kohno T., Kobayashi K., Maeda T., Sato K., Takashima A. Three-dimensional structures of the amyloid β peptide (25–35) in membrane-mimicking environment. *Biochemistry* 1996, 35, 16094–16104.

[113] Marcinowski K. J., Shao H., Clancy E. L., Zagorski M. G. Solution structure model of residues 1–28 of the amyloid β-peptide when bound to micelles. *J. Am. Chem. Soc.* 1998, 120, 11082–11091.

[114] Coles M., Bicknell W., Watson A. A., Fairlie D. P., Craik D. J. Solution structure of amyloid β-peptide(1–40) in a water-micelle environment. Is the membrane-spanning domain where we think it is? *Biochemistry* 1998, 37, 11064–11077.

[115] Shao H., Jao S. C., Ma K., Zagorski M. G. Solution structures of micelle-bound amyloid β-(1–40) and β-(1–42) peptides of Alzheimer's disease. *J. Mol. Biol.* 1999, 285, 755–773.

[116] Degiorgio V., Corti M. *Physics of Amphiphiles: micelles, vesicles and microemulsions*. Eds., North Holland, Amsterdam, 1983.

[117] Markovic-Housley Z., Garavito R. M. Effect of temperature and low pH on structure and stability of matrix porin in micellar detergent solutions. *Biochim. Biophys. Acta* 1986, 869, 158–170.

[118] Hantgan R. R., Braaten J. V., Rocco M. Dynamic light scattering studies of $\alpha_{IIb}\beta_3$ solution conformation. *Biochemistry* 1993, 32, 3935–3941.

[119] Van Os N. M., Haak J. R., Rupert L. A. M. *Physico-chemical properties of selected anionic, cationic and nonionic surfactants*, Elsevier, 1993.

[120] Kissa E. *Fluorinated surfactants*. Surfactant Science Series, Marcel Dekker New York, 1993, vol. 50.

[121] He L. Z., Garamus V., Niemeyer B., Helmholz H., Willumeit R. Determination of micelle structure of octyl-β-glucoside in aqueous solution by small angle neutron scattering and geometric analysis. *J. Mol. Liq.* 2000, 89, 239–249.

[122] Afonin S., Dürr U. H. N., Glaser R. W., Ulrich A. S. Boomerang-like insertion of a fusogenic peptide in a lipid membrane revealed by solid-state ^{19}F NMR. *Magn. Reson. Chem.* 2004, 42, 195–203.

[123] Curtain C. C., Ali F. E., Smith D. G., Bush A. I., Masters C. L., Barnham K. J. Metal ions, pH, and cholesterol regulate the interactions of Alzheimer's disease Amyloid-β peptide with membrane lipid. *J. Biol. Chem.* 2003, 278, 2977–2982.

[124] Bokvist M., Lindström F., Watts A., Gröbner G. Two types of Alzheimer's β-amyloid (1–40) peptide membrane interactions: aggregation preventing transmembrane anchoring versus accelerated surface fibril formation. *J. Mol. Biol.* 2004, 335, 1039–1049.

[125] Rozek A., Buchko G. W., Cushley R. J. Conformation of two peptides corresponding to human apolipoprotein C-I residues 7–24 and 35–53 in the presence of sodium dodecyl sulfate by CD and NMR spectroscopy. *Biochemistry*1995, 34, 7401–7408.

[126] Buchko G. W., Treleaven W. D., Dunne S. J., Tracey A. S., Cushley.R. J. Structural studies of a peptide activator of human lecithin-cholesterol acyltransferase. *J. Biol. Chem.* 1996, 271, 3039–3045.

[127] Breukink E., Demel R. A., Korte-Kool G., Kruijff B. SecA insertion into phospholipids is stimulated by negatively charged lipids and inhibited by ATP: a monolayer study. *Biochemistry* 1992, 31, 1119–1124.

[128] Kim J., Blackshear P. J., Johnson J. D., McLaughlin S. Phosphorylation reverses the membrane association of peptides that correspond to the basic domains of MARCKS and neuromodulin. *Biophys. J.* 1994, 67, 227–237.

[129] Vieira E. P., Hermel H., Möhwald H. Change and stabilization of the amyloid-β(1–40) secondary structure by fluorocompounds. *Biochim. Biophys. Acta* 2003, 1645, 6–14.

[130] Thünemann A. F., Sander K., Jaeger W., Dimova R. Polyampholyte-dressed micelles of fluorinated and hydrogenated dodecanoic acid. *Langmuir* 2002, 18, 5099–5105.

[131] Thünemann A. F., Vieira E. P., Hermel H., Motschmann H., Möhwald H., Schmahl W., Matiasek K., Sperling C., Werner C. (Max Planck Society), European Patent application EP1341564.

[132] Sargent J., Seffl R. Properties of perfluorinated liquids. *Fed. Proc.* 1970, 29, 1699–1703.

[133] Sohlenius A. K., Lundgren B., DePierre, J. W. Perfluorooctanoic acid has a persistent effect on peroxisome proliferation and related parameters in mouse liver. *J. Biochem Toxicol.* 1992, 7, 205–212.

[134] Upham B. L., Deocampo N. D., Wurl B., Trosko J. E. Inhibition of GAP junctional intercellular communication by perfluorinated fatty acids is dependent on the chain length of the fluorinated tail. *Int. J. Cancer* 1998, 78, 491–495.

[135] Micha M. A., Burger C., Antonietti M. Generalized Phase Diagram for microphase-separated systems and its determination by small-angle scattering. *Macromolecules* 1998, 31, 5930–5933.

[136] Siemann U., Ruland W. Determination of the width of the domain boundaries in polymer two-phase systems by X-ray small-angle scattering. *Colloid Polym. Sci.* 1982, 260, 999–1010.

[137] Wolff T., Burger C., Ruland W. Small-angle X-ray scattering study of lamellar microdomains in diblock copolymers in the weak segregation regime. *Macromolecules* 1994, 27, 3301–3309.

[138] Duysens L. N. M. The flattening of the absorption spectrum of suspensions, as compared to that of solutions. *Biochim. Biophys. Acta* 1956, 19, 1–12.

[139] Fromherz P. Micelle structure: a surfactant-block model. *Chem. Phys. Lett.* 1981, 77, 460–466.